GRAIN COALESCENCE AND MODELING OF NANOSIZED ZIRCONIA IN SOLID-STATE SINTERING

YU POH CHING

NATIONAL UNIVERSITY OF SINGAPORE

2009

GRAIN COALESCENCE AND MODELING OF NANOSIZED ZIRCONIA IN SOLID-STATE SINTERING

YU POH CHING

(B.S., University Technology Malaysia)

A THESIS SUBMITTED

FOR THE DEGREE OF DOCTOR IN PHILOSOPHY

DEPARTMENT OF MECHANICAL ENGINEERING

NATIONAL UNIVERSITY OF SINGAPORE

2009

ACKNOWLEGEMENTS

Firstly, I would like to express my appreciation to my supervisors, Prof. Jerry Fuh Ying Hsi, Dr. Li Qingfa and Prof. Lu Li for giving me this opportunity to further my study and their upmost support and guidance along the way.

Secondly, I would like to thank SIMTech for providing the laboratory facilities and my fellow colleagues in SIMTech for their understanding and help during the course of my study.

I would also like to express my gratitude to Assistant Prof. Srikanth Vedantam, for sharing his knowledge in phase field algorithm; Prof. Soh Ai Kah, for the fruitful discussion in phase field simulation; Prof. Zbigniew Henyk Stachurski, for his kind advice in the probability analysis; Dr. Ooi Ean Tat, for his guidance in FORTRAN language; Mr. Paul Kung and Mr. Zhang Xinhuai, for their help in using Materials Studio software to generate the random packed powder system.

Last but not least, I would like to thank my dearest family members, for their moral support over the past few years, especially to my husband, who tolerate my negligence in family and proof read my thesis.

CONTENT

SUMMARY

Micro powder injection molding (μPIM) using nanosized powder provides an alternative to mass produce micro component at competitive cost and promising novel properties. However due to agglomeration of nanosized particles and abnormal growth during sintering, use of nano powder particles in the μPIM is limited. In this study, 50 nm 3 mol % yttria stabilized zirconia powder (3Y-TZP) was used for μPIM. Agglomeration problem of nanosized powder was resolved using a preheat treatment prior mixing with a proprietary binder system, and the debound part demonstrated an agglomeration free structure. The increased difficulty during injection molding, demolding and debinding process due to high surface area of nanosized powder and micro size mold cavity was overcome. The produced micro gear was visually defect-free with well defined gear teeth and the high hardness of 3Y-TZP was preserved in micro feature. Sintering behaviour of this nanosized powder was characterized via different sintering routes and compared with conventional coarse counterpart. Density and grain size that normally used to characterise the grain growth when sintering involved nanosized powder were found inadequate. Assessment on microstructure and material property was important in ensuring that the measured density was not due to connected pore channels and the material is strong enough for applications. Nanosized powder demonstrated extensive grain growth during initial sintering stage despite the reduction in sintering temperature and holding duration. The presence of irregular shaped grains suggested that the extensive grain growth was not via classic curvature migration which yielded smooth grain boundary.

To better understand microstructure evolution of nanosized powder, phase field approach was used. Simulation result showed suppressed grain growth due to the monosize distribution followed by exaggerated growth of several grains that gained diffusional advantages at low packing regions. These observations were different from the rapid growth at initial stage and the obtained relative growth was exceptionally large to justify the empirical finding. Grain coalescence, another means of grain growth that allows instantaneous growth when the neighboring grains are in crystallography match, may be an important growth mechanism where fine grain rotation is facilitated. Grain coalescence dominated solid-state sintering model was proposed to be responsible for the extensive initial growth of nanosized powder. A quantitative analysis, based on crystallite geometry, was carried out to study the probability of grain coalescence in a random condition and found high frequency of low angle grain that can potentially rotate and coalesce during initial sintering stage. Coalescence of these low angle grains was incorporated in phase field simulation for qualitative analysis. With grain coalescence, the simulated microstructure evolution and the relative growth have shown strong agreement with empirical finding. The irregular shaped grains, as observed experimentally, were formed after grain coalescence, contributing to the extensive initial grain growth. These results suggested that sintering of nanosized powder was in substantial agreement with the proposed grain coalescence dominated solid-state sintering model. In short, understanding the grain growth mechanism of nanosized powder and resolving the difficulties of μPIM enhances the capability in tailoring the material properties for industrial applications.

Keywords: PIM, Nanosized Powder, Sintering, Modeling, Grain Coalescence

LIST OF FIGURES

LIST OF TABLES

LIST OF APPENDICES

NOMENCLATURE

Nanosized powder Powder with its size smaller than 100 nm in diameter

Feedstock A homogenous blend of powder with a polymeric binder system for powder injection molding process

Compact Solid body formed by fine powders through different processing routes (isostatic press, uniaxial press, etc.)

Green Material state before firing

Brown Material state after debinding, typically for powder injection molding, sometimes denoted as debound state

Debinding A process to remove binder composition

Sintering A thermal cycle for bonding particles into dense and strong material

Microstructure Shape, size, and distribution of different phases that conform a material at the microscopic level

Grain boundary Dislocated surface located between two contiguous grains of different orientations

Grain growth Increase in average grain size as a result of reduced total number of grains in the event of conserved mass

Grain coalescence Instantaneous grain growth with the elimination of common grain boundary

ABBREVIATIONS

PIM Powder injection molding

µPIM Micro powder injection molding

3Y-TZP 3 mol % yttria stabilized zirconia

NANO 50 nm 3 mol % yttria stabilized zirconia powder

BASF A type of commercially available 3Y-TZP feedstock from BASF Catamold ® with code TZP-F 106A

TCE Trichloroethylene, a kind of solvent

CM A furnace from the company CM Furnace Inc.

ISO Isothermal sintering

2SS Two-stage sintering

OPU A type of oxide polishing medium from Struers, made from colloidal silica suspension for final polishing of all material

MD-Chem Polishing cloth from Struers, for final polishing of all materials, make from porous Neoprene material. For magnetic fixation on MD-Disc

CSL Coincidence site lattice

SEM Scanning electron microscope

AFM Atomic force microscope

TEM Transmission electron microscope

HR High resolution, such as HRSEM and HRTEM

CHAPTER 1 INTRODUCTION

Nanosized powder has been gaining extensive attention from researchers aiming to achieve bulk nanostructure material with enhanced material properties. The nanosized powder needs to be shaped and sintered into bulk material prior applications. The shaping process consolidates the fine powder into desired shape from simple ones to complex geometries via process like powder injection molding. Densification of the weak powder compact into strong bulk material is via heat treatment or sintering process. The nanosized powder tends to grow extensively during sintering and fails to retain its nanostructure. To control the grain growth and retain the nanostructure, understanding the sintering mechanism of nanosized powder is vital.

In this chapter, the sintering of nanosized 3 mol % yttria stabilized zirconia and the mass production feasible shaping process, powder injection molding that used in this work is reviewed and discussed. The extensive grain growth behavior of the nanosized powder is analyzed based on the classic curvature migration theory developed from coarse counterpart. Grain coalescence that recently been proposed attributing to the extensive grain growth of nanosized powder is reviewed. Review on the specified topics will finally lead to the research objectives of this thesis.

1.1 Nanosized 3 mol % Yttria Stabilized Zirconia (3Y-TZP)

1.1.1 Background of 3Y-TZP

3 mol % yttria stabilized zirconia (3Y-TZP) is widely used as tooling and structural material. It has been known that zirconia has three stable phases at different temperatures. Addition of 3 mol % yttria stabilized zirconia as tetragonal polycrystal structure at room temperature. 3Y-TZP is famous for its high toughness induced from tetragonal to monoclinic phase transformation at crack tip. Besides the high toughness, its chemical inertness, wear resistant, low thermal conductivity and stability at high temperature makes it an important structural material that is widely used as cutting tools, dies and valve guides. The reported superplastic deformation behavior at high temperature[1] that had never been observed in brittle ceramics before, and improved hardness of 3Y-TZP with refined microstructure[2] makes it an ever interesting material and has gathered enormous research attention to retain its nanostructure.

1.1.2 Sintering of Nanosized 3Y-TZP

Although 3Y-TZP is widely employed, normally only micron size and submicron size 3Y-TZP powder are used due to difficulty in the processing and property control of nanosized 3Y-TZP. Since nanostructured or nanograined materials may provide very different mechanical behaviors, current researches on nanosized 3Y-TZP mainly focus on the influence of various powder synthesis methods and

sintering methods on the sintering behavior[3-18]. Agglomerates, a common problem for fine powder, are small mass of particles that bounded by relatively weak secondary bonds of electrostatic, magnetic, van de Waals or when moisture is present, capillary type of bonds formed[19]. Pores are often present between the particles within agglomerates and inter-agglomerates during compaction (Figure 1-1[20]) and will subsequently become sites for flaw development[21, 22]. Small pores in the compacts could be due to the pores inside agglomerates while the larger pores are related to pores between agglomerates. Porosity will lower the strength of a material as the voids are the weakest link in the bonding of the microstructure. The presence of large voids formed by agglomerates and inefficient packing of individual particles cause low initial or green density, eventually affects the sinterability and the properties of final part. Thus, nanosized powder has to be carefully prepared to overcome the agglomeration problem, leading to defect free sintered part.

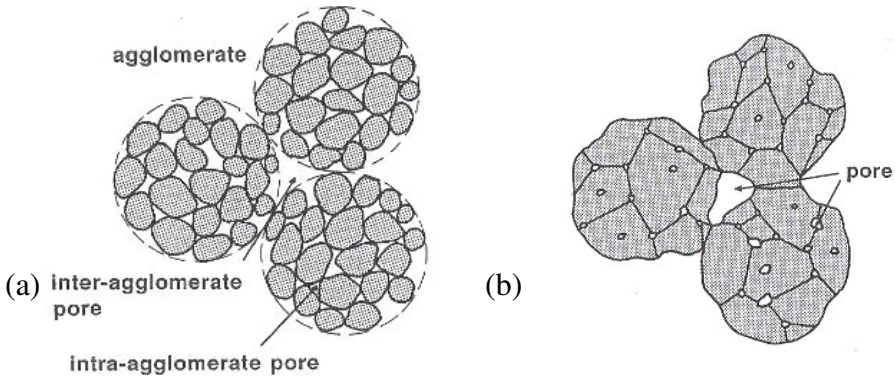

Figure 1-1 Inter and intra-agglomerates pore (a) before and (b) after sintering.

Li and Gao[7] synthesized 8 nm 3Y-TZP powder through heating alcohol-aqueous salt solution method. The powder which compacted at 450 MPa and sintered at 1150ºC for 2 hours achieved 98.5% relative density with an average grain size of

about 60 nm. Hague and Mayo[16] sinter-forged the 15 nm 3Y-TZP at 1100ºC and has achieved 98% theoretical density with average grain size of 120 nm. Recently Kim et al.[17] applied high-frequency induction heated sintering on 58-76 nm 3Y-TZP powder and obtained a relative density of 99.5% and 170 nm average grain size, under a 5 min and 100 MPa pressurized sintering at 950ºC.

Apparently the sinterability of nanosized powder is greatly enhanced, and hence a high density can be achieved at relatively low sintering temperatures. The firing temperature for nanosized powder can be lower due to its reduced activation energy[8]. Durán et al. sintered the nanosized 3Y-TZP powder at 1070ºC, compared to 1500ºC for conventional coarse powder[23]. However, sintering of nanosized powder is often accompanied by extensive grain growth even under high pressure, reduced sintering temperature and holding duration. For instance, the grain growth of the 8 nm and 15 nm 3Y-TZP is 7.5 and 8 times respectively, relative to its initial nanosize[7, 17]. Compared to its coarse counterpart, the relative growth is only less than two times[8]. Powder with soft agglomerates is desired to produce powder compact with high green density and narrow pore size distribution[24]. This criterion is reported to reduce the grain growth of nanosized powder[23]. In view of the loose packing structure inherent from debinding process, the grain growth may be more severe. This may hinders the use of nanosized powder in powder injection molding. However, sintering behavior of nanosized 3Y-TZP powder processed by powder injection molding is not reported so far.

1.2 Powder Injection Molding and Micro Powder Injection Molding

1.2.1 Powder Injection Molding (PIM)

Powder Injection Molding (PIM) was developed for small and complex parts that require high accuracy and mass production. The PIM industry has grown rapidly since the onset of its commercialization in the 1980's[25]. As of 1998, worldwide PIM related industries involved 300 manufacturers and 5,000 subcontractors[26]. The potential market for 2010 is estimated to be greater than $2.1 billion[27]. PIM combines the cost effective attributes of plastic injection molding with the superior properties of engineering materials. It is suitable for a wide range of powder materials including metals and ceramics.

Figure 1-2 shows the basic process of powder injection molding[28]. It differs from plastic injection molding as the powder itself does not melt and flow like the plastic at low temperature, usually around 100-500˚C. Thus, the first step of a PIM is mixing of the metallic or ceramics powder with binder, usually a composition of several polymeric materials in order to be able to inject into the die cavity. The mixture is termed feedstock. Rheological properties of feedstock are very important for PIM, the fluidity need to be carefully controlled together with the solid loading[29]. The molded part will then be required to go through debinding (process to extract the binder) and sintering process. Green refers to material state before firing, for parts associate with PIM, green bodies often denote fresh molded parts. Brown state is a typical term in PIM, refers to material state after debinding but prior sintering. The binder can be removed through thermal decomposition or with a combination of

solvent extraction. The aim is to gradually remove most of the binder content without generating unwanted cracks and voids, while providing some strength for subsequent handling during sintering process. Sintering process consolidates the powder into a dense and strong part. The sintering temperature, duration, pressure and environment have great influence on the final strength.

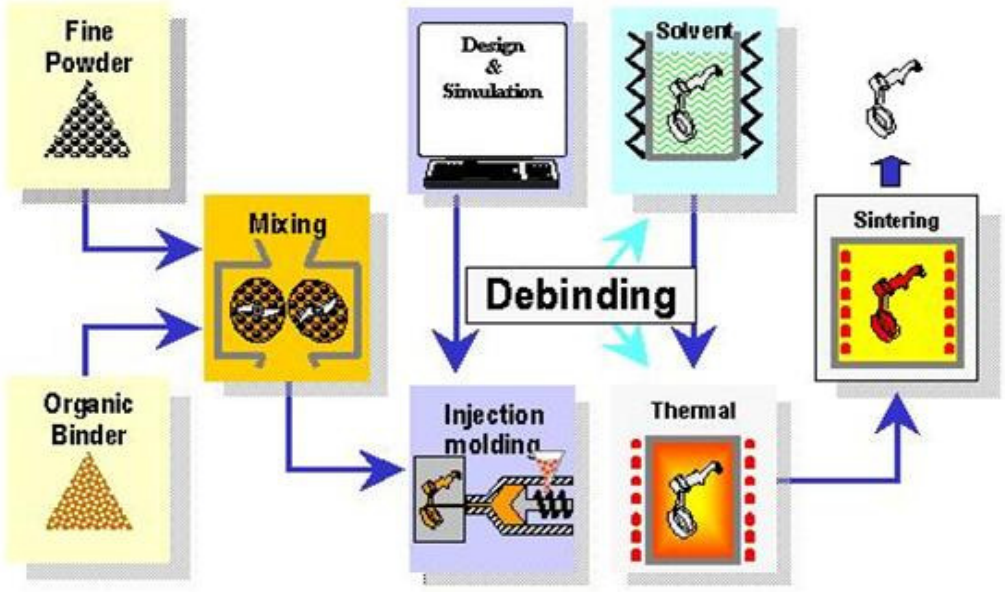

Figure 1-2 Schematic diagram of powder injection molding process[28], from mixing of fine powder with binder to injection molding, debinding and sintering in order to obtain the final part.

1.2.2 Micro Powder Injection Molding (µPIM)

Micro powder injection molding, µPIM, is a term to differentiate PIM process that involved micro size features. PIM, driven by miniaturization, is in demands with µPIM bucking the trend. With µPIM's capability of producing micro components, small tools like end mills and drills of fine diameters can be mass produced at reduced cost, which is an $8 billion U.S market[30]. Due to the fine feature size, µPIM thus

required high precision associates with more stringent requirements on powder characteristics, binder system and processing steps than PIM[31]. Fine powder is very useful in μPIM by providing smaller structure details with better shape retention and surface finishing[32]. Besides the agglomeration problem, reduced powder size also associates with higher percentage of binders and thus leading to a higher percentage of shrinkage after sintering. This may cause shrink mark in sintered parts where the powders are insufficient to hold the desired shape. Reduction in binder percentage increase the viscosity and the binder and powder may separate due to high shear stress during molding process[33]. Reported works mainly focus on rheological studies of nanosized 3Y-TZP feedstock[34-37], effect of powder characteristics[38] and powder treatment for de-agglomeration on injection molded parts[39], without the aim to produce micro features. Reports on μPIM on the other hand, aim to achieve ever smaller features by using micron size powder, typically 1-5 μm[31, 37, 40-46]. Studies on feedstock[41, 47], demolding[48, 49] and sintering kinetics[50] for micron size metal powder are also documented. Due to the high surface area per unit volume of nanosized powder and micro cavity, μPIM of nanosized powder may be extremely difficult. No documentation on μPIM using nanosized powder is found. Investigation on de-agglomeration methods of the nanosized powder, solid loading calculation and modification, injection molding process parameters optimization and debinding methods of producing defect free brown parts, as well as the sintering mechanism to produce high strength component with micro features using the nanosized powders, are of interest.

1.3 Solid-State Sintering

1.3.1 Understanding in Solid-State Sintering

Green parts require sintering before they can be used. “Sintering is a thermal treatment for bonding particles into a coherent, predominantly solid structure via mass transport events that often occur on the atomic scale. The bonding leads to improved strength and lower system energy.” [20] Solid-state sintering is a process where only solid phase is present during the sintering process. As for the 3Y-TZP, it is stable in solid state up to 2370ºC hence the sintering of 3Y-TZP at 1500ºC is in solid-state. During sintering where heat is supplied to the particles, solid bonding formed between the particles. The major driving force for sintering is the free energy reduction by replacement of free surfaces by grain boundaries (solid-solid interfaces) and grain growth (reduction in grain boundary area per unit volume). Typical solid-state sintering starts from point contact, neck formation, pore coalescence to grain growth and pore closure as illustrated in Figure 1-3[20, 51].

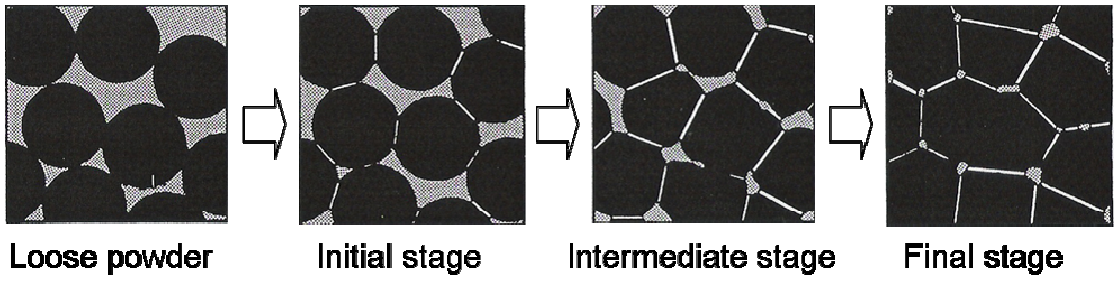

Figure 1-3 Typical sintering stages from initial powder compact to neck formation at initial stage, densification at intermediate stage to pore closure and grain growth at final stage.

Sintering can also be classified through pore structure evolution[20] (Figure 1-4). Sintering first occur at contact points and form necks during initial sintering stage. The pores between the particles will gradually decrease in size during sintering and ideally should disappear when fully sintered. However, sintering stage without any residue pores is tough to achieve in reality. For real application, sintering normally stops at final sintering stage where an acceptable quantity of isolated pores remains in the microstructure. Understanding of these morphological changes will be very useful when study the solid-state sintering process.

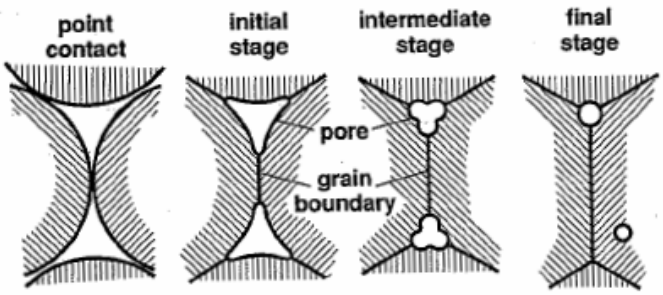

Figure 1-4 Classification of sintering process: (a) before sintering, (b) initial stage which starts from concave pore at point contact, (c) intermediate stage where the pores are gradually spheroidized as sintering proceed, and (d) final stage where the pores become isolated rounded pore at triple junction, or replaced by grain boundary.

These morphological changes are due to material transport from the individual particle to form a dense structure via surface transport and bulk transport[20]. Surface transport includes evaporation-condensation (E-C), surface diffusion (SD) and volume diffusion (VD) which only affect the neck area. On the other hand, the bulk material transport involves grain boundary diffusion (GB) and volume diffusion (VD) which will cause shrinkage.

1.3.2 Grain Growth via Curvature Migration

Grain growth always takes place during high temperature process such as sintering. Due to mass conservation, one grain grows at the expense of its neighbours. The direction of the material transport depends on the grain boundary curvature. Diffusion of atoms is from the concave side to the convex side of the grain boundary, resulting in the grain boundary migration towards the centre of the curvature into a smooth straight boundary[52]. According to Burk and Turnbull[53], this curvature migration or grain boundary motion, υ, depends on the grain boundary mobility (M_{gb}), grain boundary energy (γ_{gb}) and its curvature (κ), as expressed in equation (1-1).

$$\upsilon = M_{gb}\gamma_{gb}\kappa \qquad (1\text{-}1)$$

From equation (1-1), curvature migration is expected to be very rapid for small grain/particle as the grain boundary mobility, energy and curvature are high. Sintering of nanosized powder caused extensive grain growth compare to coarse powders thus often generally believed to be attributed to the high surface energy[4, 6, 20, 23, 54-57]. Curvature migration is relative to other neighboring grains thus results in the shrinkage of fine grains being consumed by coarse grains.

The existing understanding of the sintering and grain growth have been developed with the use of conventional coarse powder as precursor materials, therefore, it may not be appropriate when nanosized powder is considered. Densification of nano powder is reported different from conventional powder[6, 55, 58].

Other sintering mechanisms like dislocation motion, grain rotation, grain boundary slip and viscous flow have been suggested to govern the sintering of nanosized powder, at least in the initial sintering stage[59]. Therefore, fundamental understanding of the grain growth mechanism during sintering of nanosized powder thus required further validation.

1.4 Grain Coalescence

1.4.1 Grain Coalescence in Colloidal System

In 1962, Li suggested the subgrain rotation and coalescence as a natural growth process during recrystallization through thermodynamic and kinetic analysis[60]. In fact, particles rearrangement and rotation are common phenomenon during sintering[20]. Recently, grain rotation/coalescence was experimentally observed in colloidal system. The growth mechanism involves oriented attachment and elimination of common boundaries that share the same crystallographic orientation. Grain coalescence becomes significant when particles are free to move in colloidal system.

Penn and Banfield reported the imperfect orientated attachment under hydrothermal condition as important growth mechanism for nanocrystalline titatia particles[61]. Banfield et al. also documented the grain coalescence in nature by Brownian motion-driven particle collisions[62]. Leite et al. observed the presence of cluster and grain chains on low-magnification HRTEM image of SnO_2 particles

deposited at room temperature. In high magnification HRTEM image, the grain chain was found to become a single large crystalline. They suggested that grain growth via grain coalescence required only very low activation energy or even a zero-kinetic barrier[63]. Chen et al. also reported that the rotation process between coherent grains had zero-kinetic barrier and caused the grain growth during calcinations of 2 mol% Yttria Stabilized Zirconia at 600-1000ºC[10]. These findings are important as they provide empirical evidence in grain coalescence and suggest that grain growth via grain coalescence is facilitated by the ease of rotation and can be achieved even at low temperature.

On the other hand, Courtney and Lee[64] directed their attention to estimate the probability of particle coalescence in liquid phase sintered system. Geometrical and physically plausible model of the nature of low angle grain boundaries were made and the derived analytical expression was found to be in good agreement with most liquid phase sintered alloys. The importance of probability study is highlighted as an indicator of the significance of grain coalescence in microstructure evolution. However, no work has been documented to quantify the probability of grain coalescence in solid-state sintering.

1.4.2 Grain Coalescence in Fine Grain Structure

Direct observation of grain coalescence in fine grain structure, without the present of liquid phase is scarce. Harris et al. reported the in-situ observation of grain rotation and coalescence in thin film gold through HRTEM image[65], while Koga and

Takeo observed the coalescence growth of small gold cluster by X-ray diffraction technique[66]. These works are significant as fine grain rotation and coalescence is proven to take place even without the assistance of liquid phase.

Grain coalescence is also indirectly observed in other nanocrystalline materials. Chaim studied the densification mechanism in spark plasma sintering of 34 nm YAG particles and deduced that the early stages of densification of the nanocrystalline powder compact proceed by nano grain rotation, aided by particle surface softening[67]. The presence of nano grain clusters within the larger grain in HRSEM image at 1250°C and its absence at 1400°C implies that the grain growth was via grain coalescence. Wang et al. on the other hand, studied the grain growth during early stage of sintering of nanosized WC-Co powder. They attributed the rapid growth between 1000-1100°C to grain coalescence, where the liquid phase sintering was not yet activated[68]. The SEM micrograph reveals multilayers of triangular prism shaped grains which hypothesized the grain growth was by oriented coalescence instead of grain boundary migration that yields smooth and continuous surface. Contribution from Chaim and Wang et al. are worth noting as they show an alternative way to investigate the process of grain coalescence, by investigating the irregular shaped grain.

1.4.3 Numerical Study on Grain Coalescence

The development of computer simulation imparts an alternative means to study grain coalescence process when experimental proof is difficult to obtain.

Moldovan and co-workers[69-72] have highly contributed to the study of grain rotation and coalescence mechanism using molecular-dynamics simulation. They considered the driving force for grain rotation is a cumulative torque with respect to the mass center of grain, as proposed by Harris et al.[65]

$$\tau_{\mathrm{i}} = \sum_j L_j \frac{d\gamma_j}{d\theta_j} \tag{1-2}$$

where L_j is the length of grain boundary j with energies γ_j, and θ_j refers to the misorientation angle. The summation of every individual length and difference in energy relative to misorientation becomes the cumulative torque, τ acting on grain i. The simulation work extended to diffusion-accommodated grain rotation in columnar polycrystalline structure, inspired by grain boundary sliding theory of Raj and Ashby[73]. Coupling the competition between grain boundary migration and grain rotation/coalescence[70], they concluded that if the average grain size is smaller than a critical size, as in the case of nanocrystalline materials, grain coalescence dominates the grain growth over grain boundary migration. Further study on the scaling behavior of grain rotation/coalescence reveals that this mechanism followed power-law growth with a universal scaling exponent[71]. Moldovan and co-workers also elucidated the grain growth of 15nm FCC metal and concluded that grain rotation/coalescence is important, at least during the early stages of grain growth of nanocrystalline materials[72].

Other models such as phase field and Monte-Carlo are also used to study the microstructure evolution. Chen and Yang[74] described the grain orientation with a large number of non conserved order parameter (p) in phase field approach,

simulating a domain dynamics of a quenched system. When p=4, less grain orientation is generated results in high potential of grain coalescence. Irregular shaped grains are observed due to grain coalescence. Contrary to p=36, irregular shaped grain is absent as grain growth is through curvature migration. Together with Messing, they also investigated the anisotropic grain growth by Monte Carlo simulation[75]. The model allowed the coalescence of two contacting grains with same grain orientation to form a single grain without grain boundary in between. The obtained microstructure for isotropic surface energy was identical with the case of p=36, while the anisotropic case was in substantial agreement with microstructure of alumina. Upmanyu et al.[76] simulated simultaneous grain boundary migration and grain rotation and the results in atomistic scale molecular-dynamic were consistent with those mesoscale phase field model. They found that grain rotation occurs as a rigid body motion and the rotation rate increased with decreasing grain size.

The above mentioned works are highly recognized as providing important information for the driving force and highlighting the significance of grain rotation/coalescence in grain growth of nanocystalline materials during initial sintering stage. The sintering models and numerical simulations however, did not start with initial sintering stage, where grain coalescence is likely to govern the sintering mechanism over curvature migration. Thus it is more realistic to investigate the grain coalescence from the initial sintering stage of a powder compact.

1.5 Research Objectives

The previous sections have discussed the importance of the studied material and shaping method. The sintering behavior of nanosized powder, classic sintering models, grain growth via curvature migration and recently suggested grain coalescence are also reviewed. In summary, there are several inadequacies:

i. μPIM using nanosized 3Y-TZP powder is not yet explored,

ii. sintering behavior of nanosized 3Y-TZP powder processed by PIM has not been studied,

iii. whether the classic grain growth model governed by curvature migration is applicable to nanosized powder is not examined,

iv. grain coalescence model that is believed to play an important role during initial sintering stage is not studied quantitatively and qualitatively at powder compact stage or initial sintering stage.

Both μPIM and nanosized powder have great industrial potential. On the other hand, understanding the sintering mechanism of nanosized powder will contribute to grain refinement technology subsequently the material properties betterment. This thesis seeks to:

i. explore the potential of μPIM using nanosized 3Y-TZP for industry application,

ii. study the sintering behavior of nanosized 3Y-TZP processed by PIM via

isochronal, isothermal and two-stage sintering profiles to characterize the grain growth of nanosized powder,

iii. verify if the classic grain growth model governed by curvature migration is applicable to nanosized powder through phase field simulation,

iv. propose grain coalescence dominated solid-state sintering for nanosized powder,

v. verify quantitatively the proposed grain coalescence dominated solid-state sintering for nanosized powder through probability prediction using a geometrical model, and

vi. verify qualitatively the proposed grain coalescence dominated solid-state sintering through phase field simulation incorporated with grain coalescence.

Grain coalescence is facilitated by grain rotation. Many works have numerically proven the grain rotation mechanism, thus grain rotation will not be verified in this thesis. The rotation of individual powder will be simplified by assuming a misorientation threshold where neighbors with misorientation within the threshold are capable of rotating and then coalescing into a coarse grain, in both quantitative and qualitative study for grain coalescence. The proposed grain coalescence dominated solid-state sintering model may be of importance in explaining the extensive grain growth of nanosized powder during initial stage of sintering. This research may provide an alternative mass production method to the manufacturing of micro component, especially for better surface finishing of micro features or for hard-

to-machine materials like steel. Although powder synthesis method is important to determine the level of agglomeration and grain growth, this thesis has no intention to investigate the powder synthesis method. As the aim is to explore the potential of μPIM using nanosized powder for mass production, large amount of commercially available powder is needed rather than small scale lab based synthesized powder. The challenges emerging from μPIM using commercially available powder during mixing, injection molding and debinding processes will be stressed. Resolving these challenges will help to push the limit of micro component manufacturing industry in term of the feature size, property and production cost.

CHAPTER 2 EXPERIMENTAL

2.1 Methodology

2.1.1 Powder Injection Molding Process

The powder injection molding process using nanosized 3Y-TZP powder was shown in Figure 2-1. The equipments were as described in the following sections.

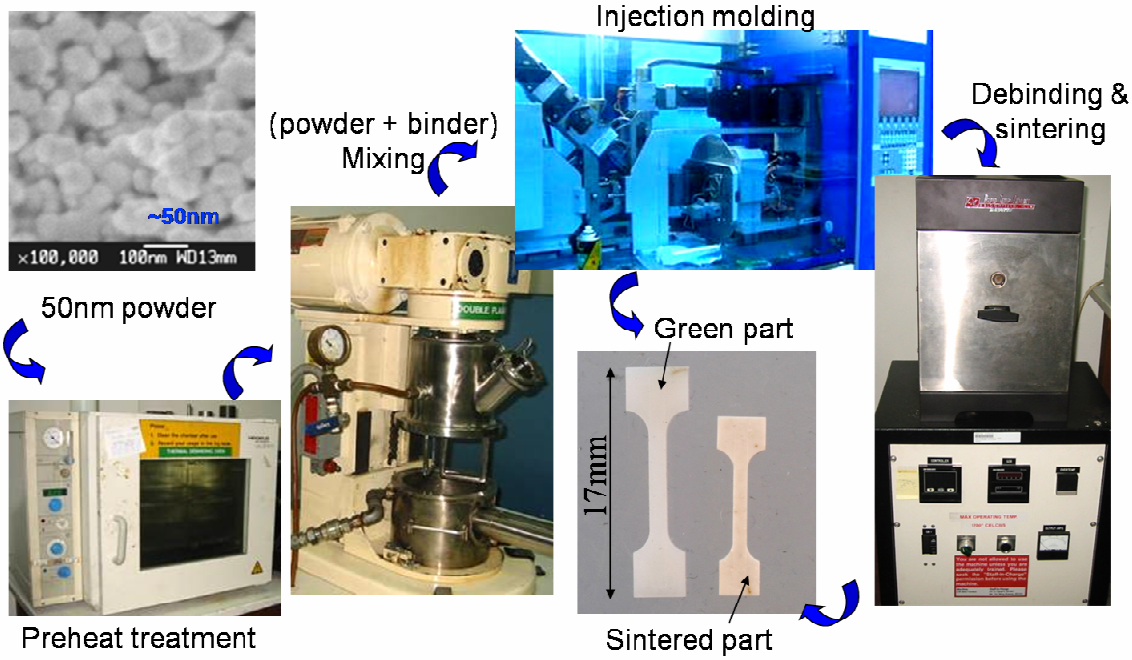

Figure 2-1 Powder injection molding process for nanosized 3Y-TZP powder with picture of actual lab equipments used in this project

2.1.2 Raw Materials

3Y-TZP powder from Microcoating Technologies with average size of 50 nm (based on supplier information) termed as NANO was used in this study. NANO will be compared with its coarse counterpart, the commercially available BASF Catamold ® TZP-F 106A, which is denoted as BASF. Figure 2-2 shows the size distribution obtained from pre-sintered fracture surfaces, in grain area, and the powder diameter is calculated based on assumption of circular powder shape for both powders. NANO shows very narrow size distribution with the average size of 67.7 nm, while BASF has wider size distribution ranging from 65.5 nm to 316.1 nm, with average size of 162.7 nm.

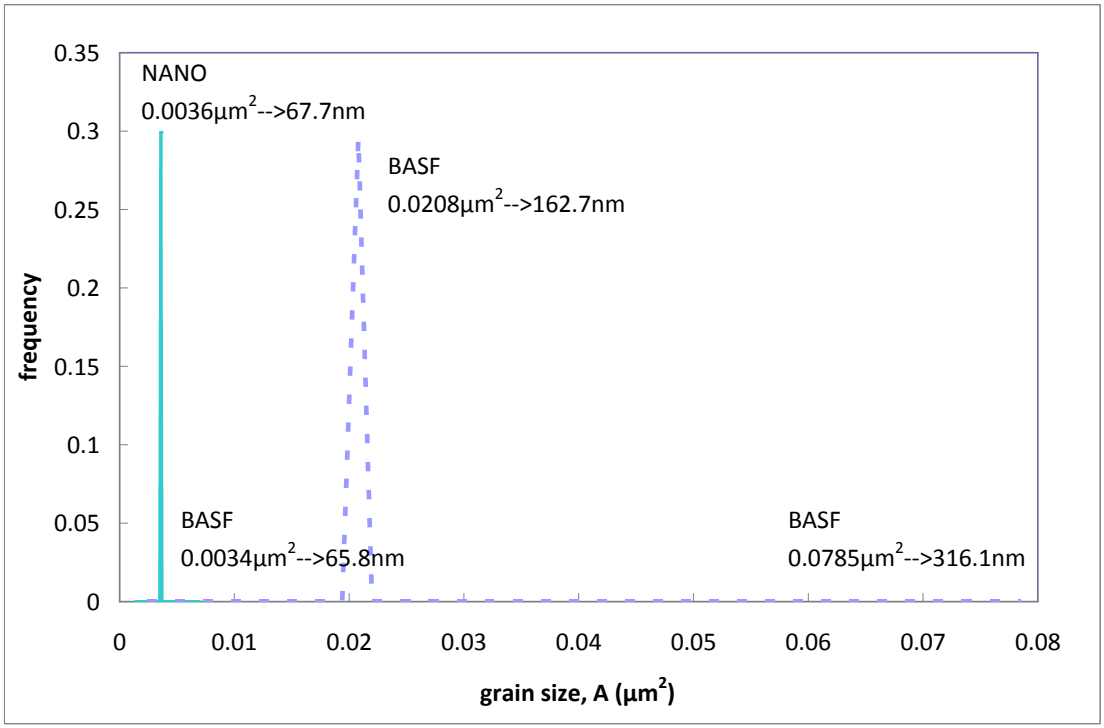

Figure 2-2 Powder size distribution of nanosized (NANO) and coarse (BASF) 3Y-TZP obtained from SEM micrographs of samples pre-sintered to 900ºC, on fracture surface without etching.

2.1.3 Feedstock preparation

Feedstock of the nanosized 3Y-TZP was prepared by a double planetary mixer. A proprietary wax based binder system was formulated to impart flowability and moldability. The binder was first melted at 150ºC followed by addition of powders in small consecutive loading. Solid loading is the volumetric ratio between powder and polymeric binders. Three different feedstocks were prepared at solid loading of 26, 41 and 45 vol. %. After reaching the desired solid loading, the feedstock was mixed at 30 rpm under vacuum for one hour to increase the homogeneity. The blend was then allowed to cool down and mechanically crashed into fine granules. Mixing was not required for ready mixed BASF feedstock.

2.1.4 Injection Molding

PIM of mini tensile bars with green dimensions of 17 mm in length and thickness of 1.2 mm were first fabricated. Scaling down to μPIM, a micro gear with 3 mm outer diameter and 20 teeth was selected. The mould insert was manufactured by high precision micro milling of harden steel with 56 HRC. Injection molding of mini tensile bar and micro gear were carried out using 5 tons Batttenfeld Micro Molding Machine.

2.1.5 Debinding

Four different debinding methods were used prior determined the suitable

debinding method for nanosized powder. Thermal debinding heated the samples in air to 360ºC for 8 hours; with 1ºC/minute ramp up rate and 5ºC/minute ramp down rate. Solvent debinding immersed the samples in 50ºC Trichloroethylene (TCE) solvent for 10 minutes, followed by the same thermal cycle, but only 2 hours holding at 360ºC. Wicking methods embedded the samples in wood powder followed by the same thermal cycle post solvent debinding. Slow thermal debinding profile is the same as thermal debinding, but with a slow ramp up rate, 0.1ºC/minutes. Slow thermal debinding with a pre-sintering to 900ºC is shown in Figure 2-3. This thermal cycle provides additional strength for subsequent handling prior to sintering. All thermal cycles were carried out in CM box furnace.

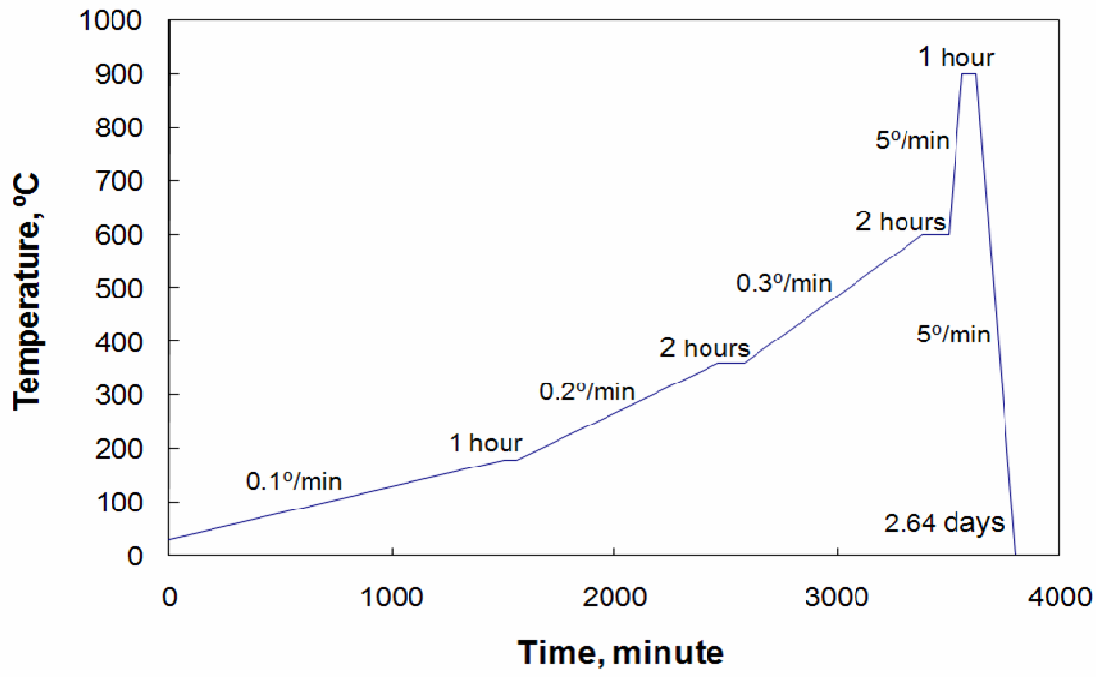

Figure 2-3 Slow thermal debinding profile with a pre-sintering at 900ºC is able to increase the strength of brown parts for subsequent handling

2.1.6 Sintering

A CM box furnace was also used for sintering. Two different sintering processes were employed. The first type of sintering only adopted a simple route where the specimens were preliminary sintered at 1500ºC for one hour. The results obtained through simple sintering will be discussed in Chapter 3. In the second type of sintering which will be discussed in Chapter 4, isochronal, isothermal and two-stage sintering were used. Figure 2-4 shows the two-stage sintering profile (2SS) used in this project. Isochronal sintering at varies sintering temperatures for 6 minutes or one hour followed. Isothermal sintering referred sintering at temperature of 1300˚C for 6 to 2400 minutes (40 hours). The ramp rate is 5˚C/minute to sintering temperature and to room temperature. The holding time at T_2 is 1 hour unless

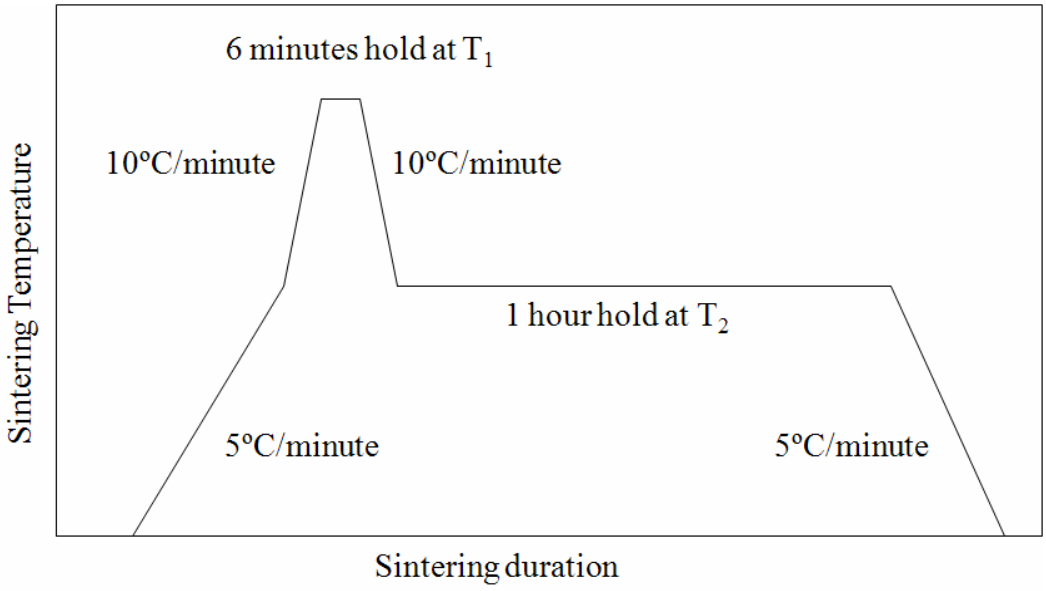

Figure 2-4 Two-stage sintering profile that used in this study consists a first stage high temperature sintering for a short duration follows by a longer dwelling at a lower temperature, to limit the grain growth occur during sintering process

specified. Isothermal sintering (ISO) is 5ºC/minute heating to T_2 and hold for 1 hour (or 6 minutes in section 4.3.2), followed by 5ºC/minute cooling down to room temperature. For isothermal sintering, $T_1=T_2$. 2SS-1500/1100 represented two-stage sintering with 6 minutes sintering at temperature of 1500ºC followed by 1 hour holding at 1100ºC, while ISO-1500 is 1 hour isothermal sintering at 1500ºC.

2.2 Physical properties Characterization

Structures of the as-sintered parts were measured using a Shimadzu X-ray diffractometer (XRD-6000) with Cu Kα radiation (λ=0.15406 nm). Sintered tensile bars were evaluated through linear shrinkage, density and Vickers hardness. The shrinkage percentage was measured through the dimensional change of green and sintered body, according to $\Delta L/L_o$ for both the length and thickness. The density was measured using Archimedes method in distilled water. Relative density was calculated based on theoretical density (6.06 g/cm^3) for tetragonal Zirconia. Vickers Hardness test was conducted using a Mitutoyo Machine at 1 kgf load on polished surface.

2.3 Morphological properties Characterization

Sintered micro gear was visually inspected for defects and shaped retention. Pore structure was examined using Atomic Force Microscope (AFM). A Cambridge S361 SEM or a field-emission scanning electron microscope (JSM 6340F, JEOL, FE-

SEM) were used for microstructure observation. The pre-sintered samples were directly observed at the cross section of fracture surface.

2.3.1 Thermal Etching

The sintered samples were first ground to 3 μm diamond finishing followed by mechanical chemical polishing with OPU on MD Chem polishing cloth from Struers for 2 minutes. Generally, to reveal the microstructure of a polished surface for Zirconia or Zirconia based ceramics, thermal etching vary from 1250ºC to 1400ºC has been widely applied [77-80]. However, it is not recommended for fine grain specimen which the high temperature supplied during etching process could simultaneously induced grain growth[81]. For rough surface like unpolished surface, fracture surface or surface inside a pore, grain morphology can be observed directly, as in Figure 2-5 (a). However, the uneven surface height and angle may affect the judgment on grain size, thus polishing is required for standard grain size measurement. Polished surface prior thermal etching (insert picture in Figure 2-5 (a)) shows limited details like pores and cracks, without information on grain morphology. Comparison between samples etched at 1400˚C and fracture surface without etching shown negligible difference in term of average grain size (Figure 2-5). This suggests that etching for 6 minutes at 1400ºC for sample sintered at 1400ºC can effectively delineate the grain boundary without causing significant grain growth. Thus, 6 minutes thermal etching at the sintering temperature will be applied to polished samples. For samples sinter at temperature higher than 1400˚C, 6 minutes thermal etching at 1400˚C will be used.

For sample at pre-sintering stage, no etching is required as microstructure appeared in raw powder stage.

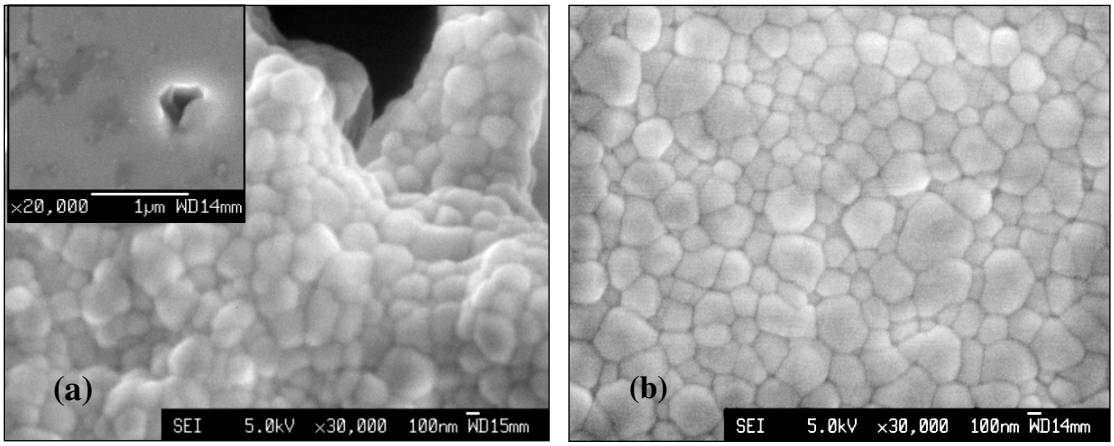

Figure 2-5 (a) Without thermal etching, micrograph taken on unpolished fracture surface reveals the microstructure, however only porosity and micro cracks can be observed on the polished surface before thermal etching, as the insert picture in (a). (b) after 6 minutes 1400°C etching, the grains appeared on flat polished surface. Both grain size and grain size distribution before and after etching are found to be similar, without significant grain growth during thermal etching process

2.3.2 Grain Size Measurement

The average grain size was determined from the obtained micrographs. Image processing was used to enhance the contrast, find edges and clean images prior to measurement with Photoshop software. Grain area was measured using image analysis software, Scion Image. Approximate of 200 grains were measured for each category. Grain diameter was measured according linear intercept method with at least 15 line segments for each category. The measured grain diameter on polished surface was multiplied by a correction factor of 1.56 to determine the true grain size[16, 82].

CHAPTER 3 MICRO POWDER INJECTION MOLDING (μPIM) – RESULTS AND DISCUSSION

Although μPIM is an adaptation of PIM that comprises of the same processes of feedstock preparation, injection molding, debinding and sintering, the requirements for μPIM are far more stringent and need additional precautions. De-agglomeration, optimization of solid loading versus flowability, injection molding profile, demolding and debinding will be discussed. The green parts were obtained by micro powder injection molding μPIM where were sintered isothermally at 1500ºC for one hour. Near densed (>98% of theoretical density) tensile bars and 3 mm diameter micro gears were produced using 50 nm 3 mol % Yttria Stabilized Zirconia (3Y-TZP).

3.1 Characterizations

3.1.1 Microstructure of Debound Nanosized 3Y-TZP

Figure 3-1 shows morphology of the brown part after debinding and pres-sintering to 900^{o}C. At low magnification, the powder distribution is uniform and near monosized. While at high magnification, the powder appeared in spherical shape without agglomeration.

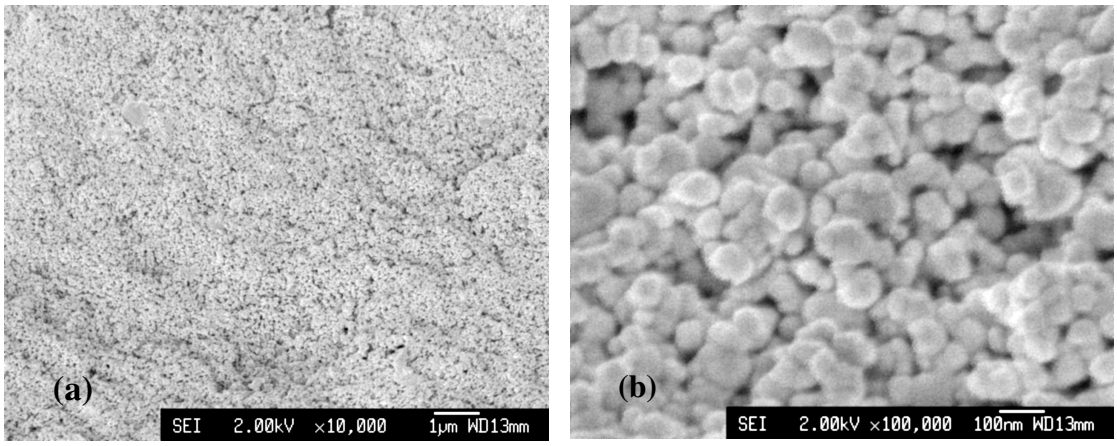

Figure 3-1 Microstructure of debound nanosized 3Y-TZP. (a) low magnification micrograph shows near monosized powder in uniform distribution and (b) high magnification micrograph reveals agglomeration free spherical particles.

3.1.2 XRD of Sintered Parts

Figure 3-2 shows XRD spectra of both sintered BASF and NANO which the peaks correspond to tetragonal phase zirconia. The identical profiles indicate that both are 3Y-TZP materials, with comparable composition and crystal structure and sintering at 1400˚C does not change their structures.

3.2 Critical Issues in μPIM

3.2.1 Agglomeration

Fig. 3-3 show the microstructure of NANO compact with and without preheat treatment at 150˚C for one hour since in the sintering of nanopowders, agglomeration is the critical issue of nanosized powder[36, 54, 83]. Highly agglomerating powders lead to severe defects as shown in Figure 3-3 (a) where voids and cracks are clearly observed.

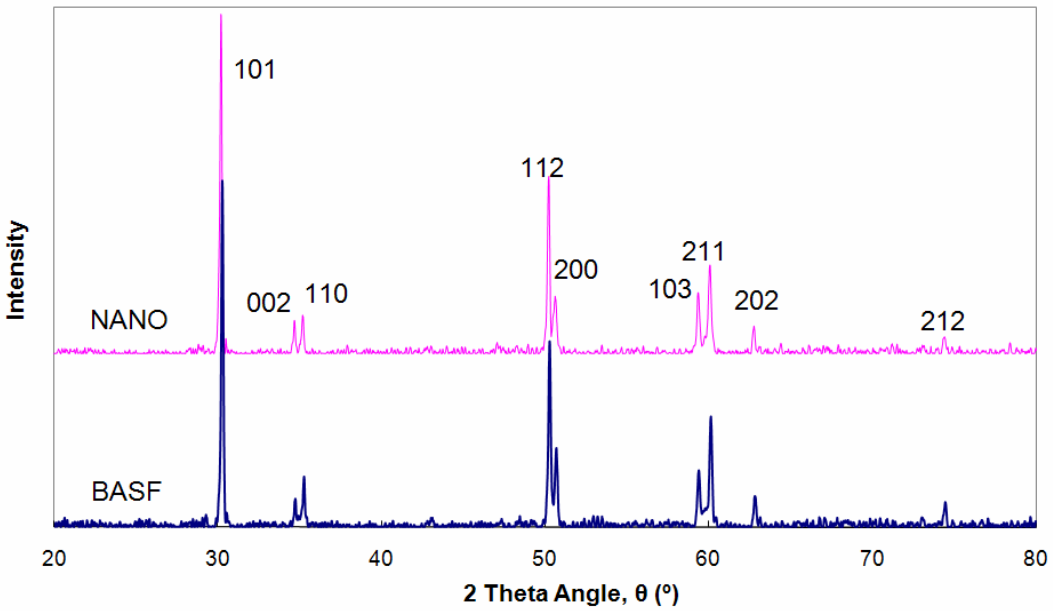

Figure 3-2 XRD profiles for both BASF (BASF-TZP-F) and NANO (50nm 3Y-TZP) are identical, indicating that both are tetragonal structure zirconia, with comparable composition and crystal structure.

Several attempts such as high compaction pressure, high sintering temperature and longer holding duration, and addition of binder and additives were made to eliminate the voids and cracks, but all were unsuccessful. Agglomerates formed inter-agglomerates bonds that are strong enough to resist compaction pressure and remained as flaws after sintering. Several methods have been reported to be able to overcome agglomeration problem. Zhu and Fan[84] preheated the powder to 500ºC prior to pressing to remove the surface hydroxyl group, while Wu and Wei [37] preheated the ball milled powder to 300ºC. In this experiment, preheat treatment to 150ºC was used. Figure 3-3 (b) shows tremendous improvement after preheat treatment at 150ºC for one hour. This implies that the agglomerates in fine powder are mainly induced by the presence of hydroxyl group when exposed to atmospheric moisture. The hydroxyl

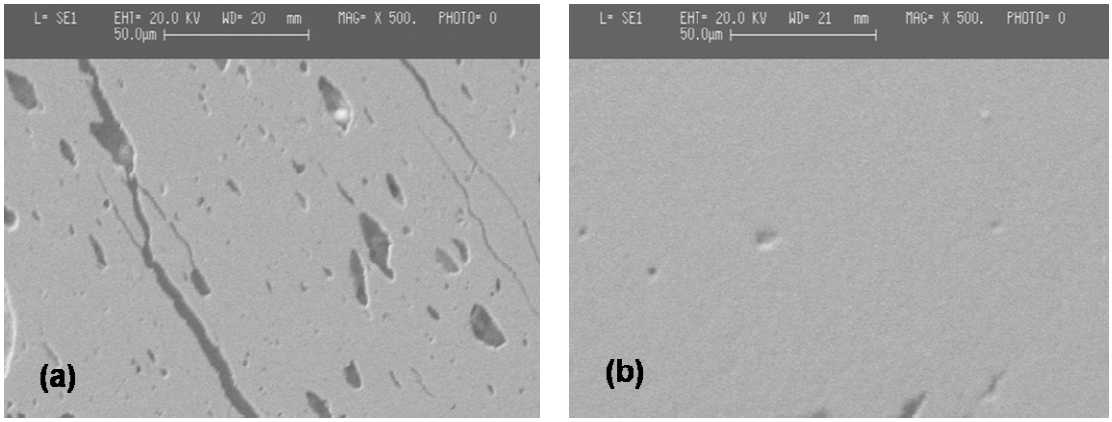

Figure 3-3 Microstructure of NANO compact (a) without and (b) with preheat treatment at 150˚C for one hour.

group creates attractive forces strong enough to flocculate the fine powder. In addition, the moisture entrapped on the powder particle surface expands during sintering. If the gas is unable to escape from the being sintered part, pores will be formed. Preheat treatment of the powder above 100ºC evaporates the moisture that causes agglomerations. Slightly higher temperatures were used for preheat treatment to compensate the efficiency of oven and also the possibility of impurities that increased the evaporation temperature of water.

3.2.2 Solid Loading Optimization

Optimizing the solid loading and viscosity is also critical. Figure 3-4 compares the properties of shrinkage, mass loss, density and hardness for feedstock at different solid loading, to identify the optimum solid loading. Mass loss is a solid loading dependent property which achieved a constant value after debinding process. Shrinkage although depends on solid volume loading, generally increased with

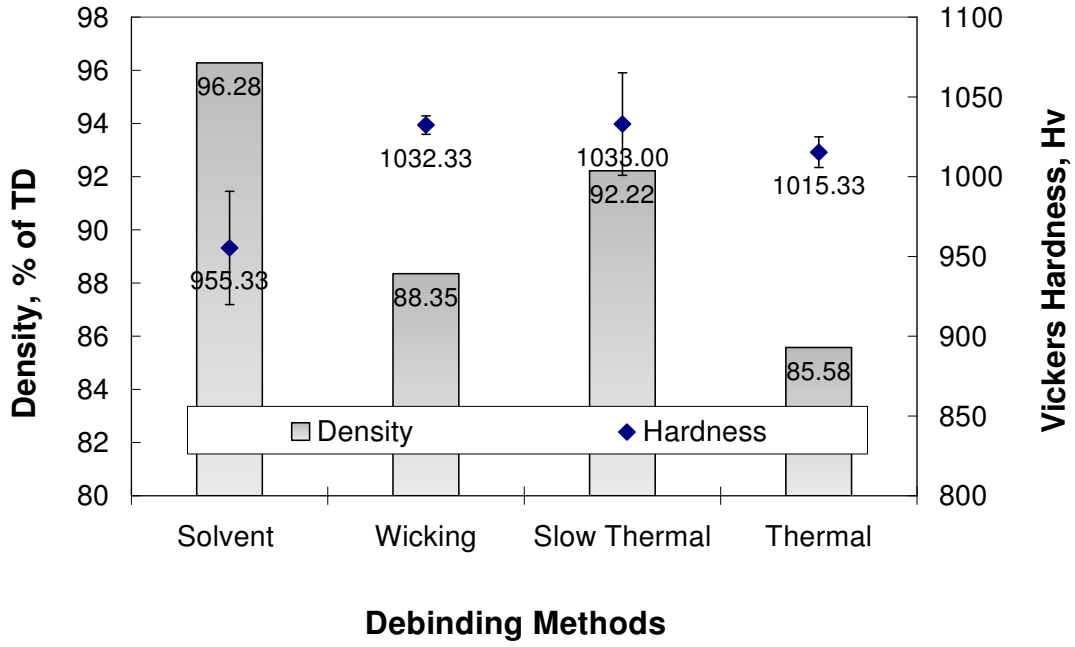

Figure 3-4 Effect of the volumetric solid loading on properties of shrinkage, mass loss, density and hardness, 41 vol. % is found optimum with higher hardness, smooth injection and well shape retention after sintering

sintering temperature and holding duration, and affected the density and hardness subsequently. At 26 vol. % solid volume loading, the high binder concentration assisted the injection process. However, the low powder content was insufficient to retain its net shape with visible sink marks observed after sintering. Typical solid loading for PIM falls around 60 vol. % [25]. Such low solid loading (26 vol. %) caused high shrinkage and shape distortion after sintering. High powder contents are necessary in PIM samples to retain the shape. Both 41 and 45 vol. % solid loading have successfully retained the shape after sintering, without shrink mark. Even though so, the injection process for feedstock with 45 vol. % was relatively difficult, when compared to 41 vol. %. Scaling down powder size corresponds with the increase of

total surface area per unit volume of the powders. The increased solid loading increased the viscosity and impeded the injection process. This may contribute to the reduced hardness of 45 vol. % feedstock, compared to 41 vol. %, which yielded the highest hardness. 41 vol. % solid loading was hence defined as the optimum solid loading for this 50 nm 3Y-TZP.

3.2.3 Short Shot during Injection Molding

With the increase viscosity, injection molding becomes difficult. Short shot or insufficient filling was occurred, especially at micro features. As viscosity is temperature sensitive, the molding temperature has to be carefully controlled. Several degrees difference in the respective heating zones was observed to significantly affect the moldability. Referring to Table 3-1, it is observed that temperature profiles vary with binder system, powder size and the complexity of the feature. For the tensile bar, temperature profile for rear barrel/front barrel/nozzle/mold was 190/190/180/50 for conventional BASF feedstock and 140/135/130/50 for nanosized powder feedstock prepared in-house. With micro gear feature, the temperature profile for latter was increased to 170/170/165/60. PIM of micro gear using BASF feedstock was not successful thus no suitable temperature profile was documented. The failure in molding micro gear by BASF may be attributed to the relatively coarse powder size in irregular shape and wider size distribution, as observed in Figure 3-5.

Table 3-1 PIM temperature profile at different heating zones that vary with binder system, powder size and complexity of feature

Temperature (°C)	BASF tensile bar	NANO tensile bar	NANO micro gear
Rear barrel	190	140	170
Front barrel	190	135	170
Nozzle	180	130	165
Mold	50	50	60

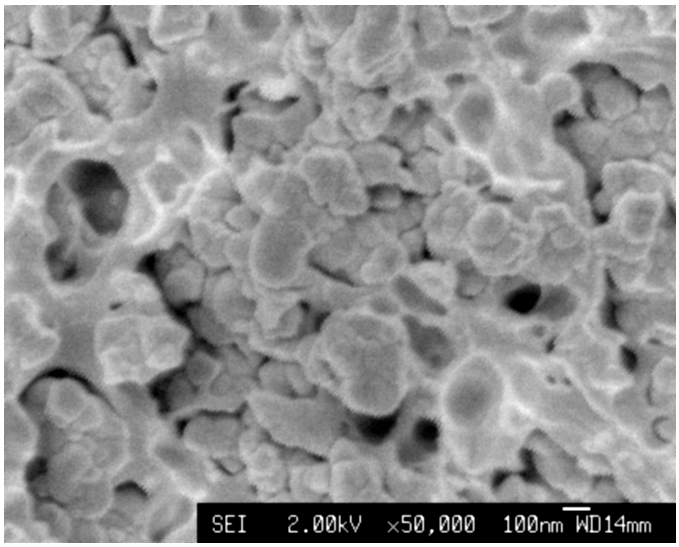

Figure 3-5 Debound BASF shows irregular shaped powder with wide size distribution, which is unfavorable to injection molding of micro feature

3.2.4 Incomplete Demolding

Demolding is a step when shaped molten feedstock solidified and ejected from the die cavity. Figure 3-6 (a) shows the green and sintered tensile bars with the dimensions relative to a paper clip. Demolding of the tensile bar was easy due to the simple shape and larger size. For μPIM, however, even with complete filling, defects

often generated during demolding. The Adhesive force between the feedstock and micro-cavities was exceeded the material green strength resulting in incomplete demolding. The use of the variotherm mould is recommended to ensure complete filling of the micro features and high green strength for demolding[31]. Fleischer et al. [85] on the other hand suggested the development of a special ejecting system with ejector pins of inner diameter 525 μm, surrounding the inner core of the feature to ensure shape retention during demolding. In this study, the die set that is initially designed for plastic injection molding was modified by inserting a thin layer of plastic gear base into the mould cavity. With this support base, the ejector pin transfers the force to the whole micro gear, including the gear teeth, promoting the ejection of the micro gear and teeth. Figure 3-1 (b) shows the molded green parts with an attached layer of plastic gear that will be decomposed during heat treatment.

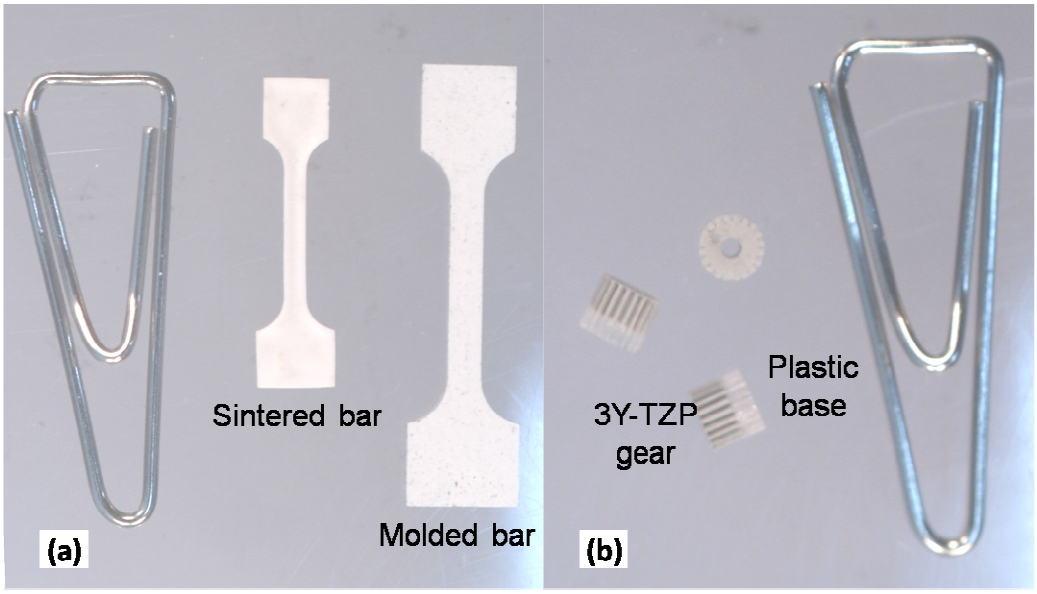

Figure 3-6 Photographs showing (a) green and sintered tensile bar and (b) green micro gear with attached plastic gear base for ease of ejection. Specimens size are visually compared with a paper clip

3.2.5 Optimization of Debinding Process

Polymeric binders are the temporary vehicles for flowability. A proper debinding process is necessary to avoid defect formation[86]. Several debinding methods were tested on the 26 vol. % feedstock, as shown in Figure 3-7, for the most desirable density and hardness. The solvent debinding process utilizes both heat and polymer dissolution to remove the binders. Oliveira et al.[87] in particular studied solvent debinding kinetics for PIM specimens. Although solvent debinding can effectively shorten the debinding cycle, it was found to be less effective for small specimens as the turbulence produced by the solvent can be relatively strong to generate flaws. Surfaces were found to be severely cracked, and the resulting hardness was low. The wicking method adopts both thermal and absorbent effects. Samples subjected to wicking are submerged under an absorbent powder and subsequently heated in a furnace. The hardness of samples debound by this method was increased significantly. The porous powder substrate provides sponging action to facilitate the extraction of the molten binder out of the powder compact. Not all binder can be extracted via wicking method, and the remaining binder formed pendular bond at powder contact[33]. The brown part was strengthen, thus reduced flaws generation prior sintering, and thus increased the final hardness. The slow thermal debinding process demonstrated the best combinations of density and hardness. As the sample was heated up with a very slow heating rate, the binder decomposition was started at surface and escaped slowly without generating unwanted flaws. Recently Thomas-Vielma et al.[88] reported an optimized 18 hour thermal cycle for 0.8 μm alumina with high density polyethylene binder system. Thermal debinding cycle with faster heating

rate was attempted to speed up the debinding process. The sample hardness was reduced as the increased heating rate resulted aggressive binder decomposition and caused micro cracking. Hence, the slow thermal debinding is identified as the optimum debinding method.

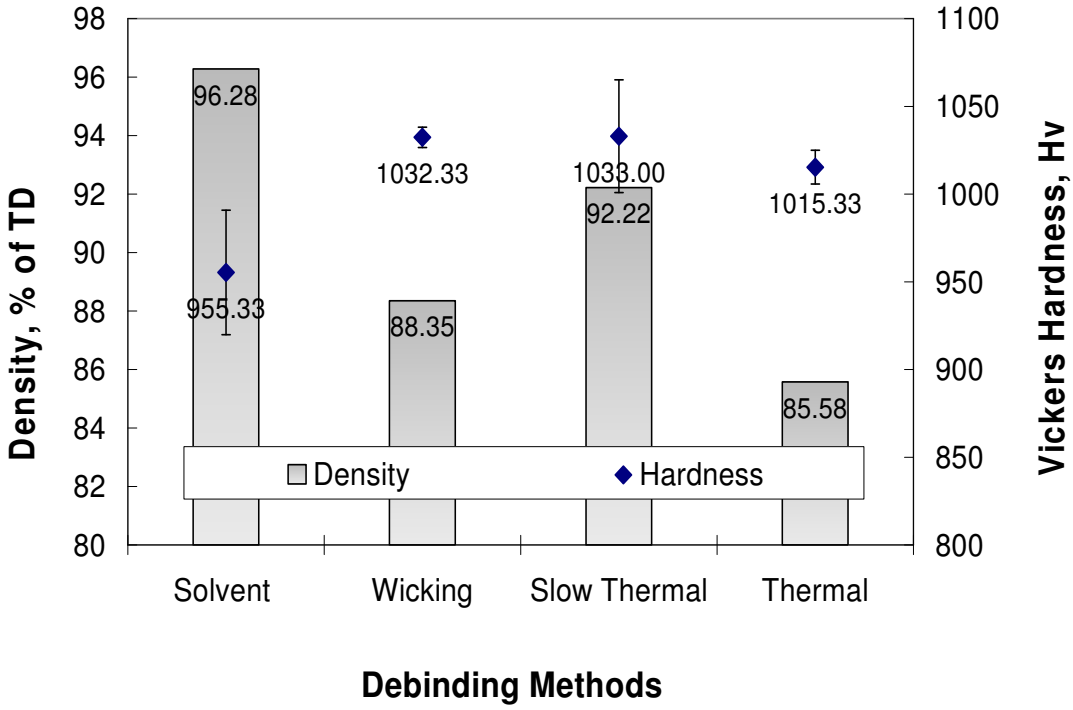

Figure 3-7 Density and hardness as a function of debinding methods, which slow thermal debinding yields best combination of hardness and density

3.3 Characterizations of Micro Gear

It is found that sintered samples of 41 vol. % feedstock experienced isotropic shrinkage around 23% with 16% mass loss. Near dense (>98% theoretical density) tensile bar achieved hardness of 1121 Hv. Figure 3-8 shows the sintered 3 mm micro gear with 20 teeth. The gear teeth shrunk to about 73 μm after sintering. Visual inspection observed overall isotropic shrinkage and good shape retention with the

gear teeth well defined. Material property was preserved in fine and complex features. Vickers hardness of the micro gear yielded the same hardness as the tensile bar. The arrow in Figure 3-8 (c) pointed to the typical indentation of a Vickers hardness test. The well defined diamond shape indentation mark without crack lines at the tips was corresponding to the high toughness of the micro gear. As powder of at least one magnitude smaller than the micro features is necessary for good shape retention25, 89, the moldability and sinterability of 50 nm powder demonstrated in this report suggested that μPIM of features as small as 0.5 μm was feasible.

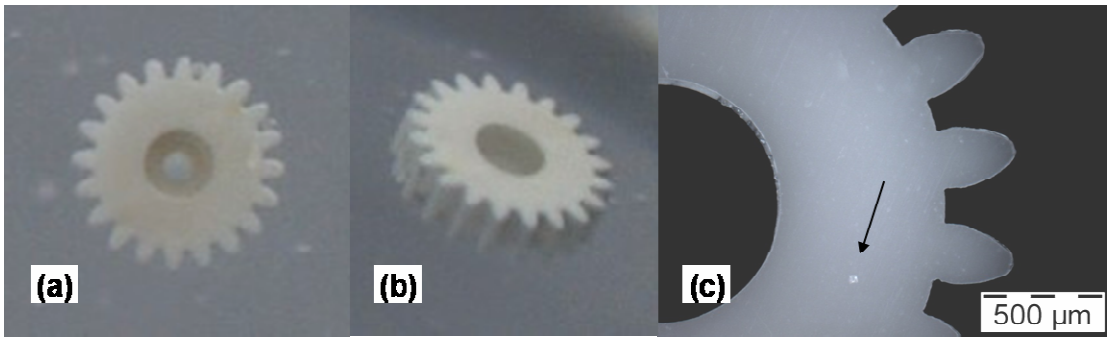

Figure 3-8 Optical microscopic photographs showing (a) the top and (b) isometric views of a sintered micro gear revealing excellent shape retention, (c) well defined gear teeth and the arrow pointed an indentation mark of Vickers hardness test

3.4 Summary

Micro powder injection molding (μPIM) of nanosized powder was found to differ from conventional PIM of coarse powders. In this study, the problems arising from μPIM using nanosized powder have been addressed. The problem of agglomeration was resolved by preheat treatment. Proprietary binder system with 41 vol. % of 50 nm 3Y-TZP powder was found to provide good dimensional control and

flowability. Injection molding is temperature sensitive and complex shape demands higher temperature profile. It is found that fine powders and features increased the difficulties of binder removal and the handling of the brown part. The debinding method that is used for coarse powder and macro parts is not suitable for nanosized powder and micro feature. Solvent debinding of small parts was detrimental and thermal debinding at slow ramp rates was preferred. The production of micro gear with 50 nm 3Y-TZP powder suggests that micro features as small as 0.5 μm with interesting properties, such as the reported superplasticity in ceramics may be possible in near future.

CHAPTER 4 SINTERING OF NANOSIZED 3Y-TZP– RESULTS AND DISCUSSION

The capability of powder injection molding micro features was outlined in previous chapter. The properties of sintered parts may be improved with different sintering profiles, typically for grain refinement to enhance the grain size dependant properties. Grain growth however is remaining as a major problem when sintering nanosized powder. Initial researches proposed that high green density and minimum sintering temperature are beneficial in controlling the grain growth of nanosized powder. In view of the inherent loose packing from debinding process, grain growth control of nanosized powder processed by PIM may be more challenging. In this chapter, the 3Y-TZP was isochronally sintered at a temperature of 1100 to 1500ºC and obtained results will be discussed.

4.1 Appropiate Sintering Measurement Techniques

There are many parameters that can be used to assess the sintering process, such as microstructure measurement, material properties and dimensional changes [20]. Despite a wide range of measurements, mass loss, shrinkage, density, hardness and microstructure in particular are recorded. Sintering is often categorized into four stages, according to the microstructure changes from contacting particles to neck

growth, pore coalescence and finally pore shrinkage and grain growth. Each stage is progressively changed in term of neck size, pore size and grain size. To differentiate the minor changes within each stage, or thereby termed as sintering degree, selection of one common parameter is of necessity.

4.1.1 Mass Loss, Shrinkage and Relative Density

The mass loss was found to be constant for all fully debound samples, independent of the sintering degree. For NANO with solid loading of 41 vol. %, the typical mass loss was 23.2% as reported in Figure 3-4 and 20% for BASF, corresponding to the amount of binder. The shrinkage and density were varied with different sintering degrees, as shown in Figure 4-1. Generally, the samples shrank as sintering proceeds and saturated at about 23% corresponding to the green packing density. Despite the higher shrinkage with the increasing sintering temperature, density of the samples fluctuated between 93 to 98% relative to its theoretical density, for both NANO and BASF.

4.1.2 Morphology Study

Figure 4-2 reveals a porous structure of the sample sintered at 1100ºC. Due to insufficient interdiffusion between different particles, such porous structure led to the low shrinkage (11.7%). On the other hand, such porous structure cannot explain the obtained high density (97.8%), as shown in Figure 4-1. During the sintering process,

neck growth and pore shrinkage reduce the distance between particles increasing both the density and leading to shrinkage. Referring to the porous structure, it seems that the connected open porosity system has misled the density measurement. As the density was measured by Archimedes method, water filled up the open pores volume and the measured sample volume reduced without considering the open porosity. Hence, only 2.2% closed pores was detected. Measuring the density of such porous system was similar to the true density measurement of loose powder. This resulted in the high density of the porous sample sintered at 1100ºC. To correct the measurement, the porous sample was first immersed in oil to avoid the water filling up the open pores. The corrected density was 76.2%, corresponding to 21.6% open porosity.

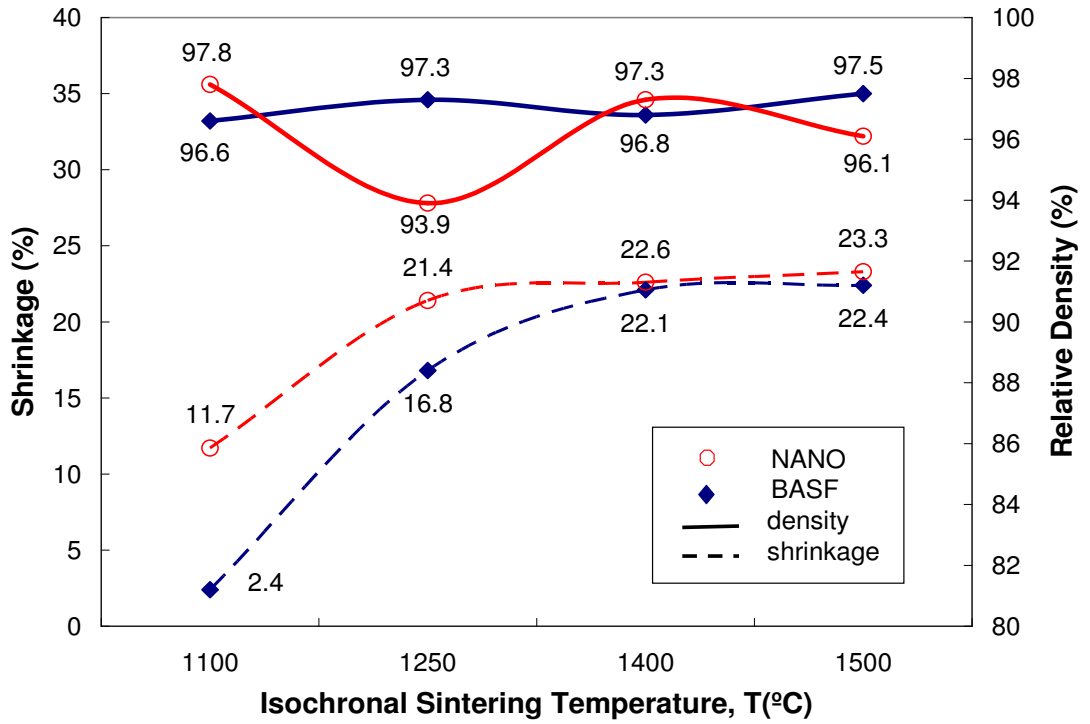

Figure 4-1 Sintering degree is measured through shrinkage and relative density at varies sintering temperatures. The shrinkage increase with the sintering temperature, however high shrinkage does not guarantee high measured density

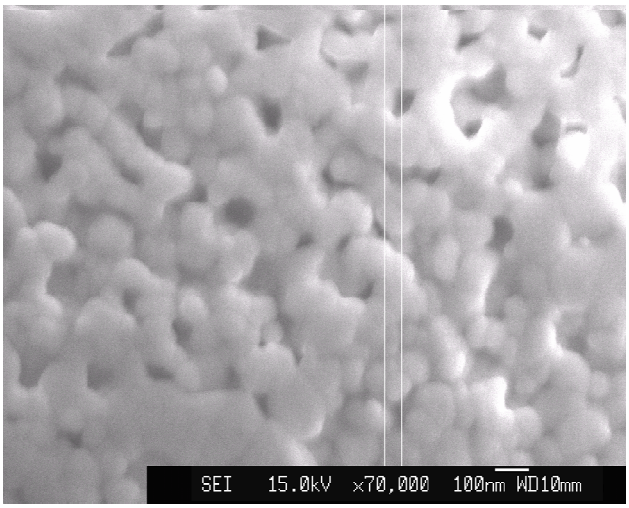

Figure 4-2 A porous microstructure after one hour sintering at 1100ºC shows that the sintering has proceeded to neck growth stage; the line measurement read the connected particle size at 66 nm

In some instances, as demonstrated by NANO at 1500ºC in Figure 4-1, the density of the samples could also decrease with the prolonging sintering due to pore coarsening. As sintering proceeds, pore structure evolves from connected pores to isolated pores. Some pores coalesce into a coarser pore while some pores shrink and disappear. Evolution from open pores to isolated pore causes reduction in density measurement, while pore shrinkage and elimination increases the measured density. Pore shrinkage or coarsen depends on the pore coordination number[5, 20, 52, 90, 91]. With additional depth information, AFM images in Figure 4-3 clearly indicate different pore structures between NANO and BASF. The pore structure found in NANO is categorized as high grain coordination pore, which is generally similar in size or even bigger than the grain, usually surrounded by five or more grains. This type of pore is very stable and will resists further densification. In contrast, the low coordination pore found in BASF will shrink as the sintering continues and increase the relative density.

Referring to the pore configurations as insert illustration in Figure 4-3, high grain coordination pore is thermodynamically stable with convex grain surface, while low grain coordination pore has unstable concave grain surface[52]. Coarse grain size is beneficial for sintering with reduced pore coordination number. Coarse grain structure like BASF, rarely have high grain coordination pore. Therefore its density was proportional to sintering degree. Contrast to BASF, due to the high grain coordination pores, the finer grain size of NANO may cause a decrease in density as sintering proceeds.

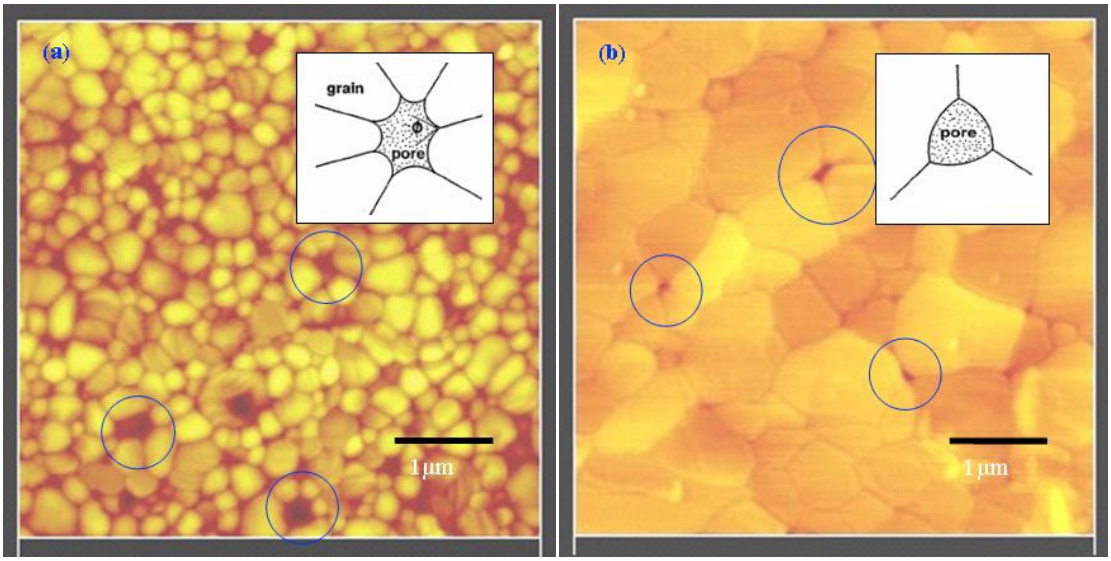

Figure 4-3 AFM micrograph shows grain size of (a) NANO compact being much smaller than (b) BASF. However the fine grain structure tends to create high coordination pores, as the insert illustration in (a), resist pore shrinkage and may coarsen during prolong sintering and reduce the final density

4.1.3 Vickers Hardness

Figure 4-4 shows that the hardness of both the NANO and BASF increases with sintering temperature up to 1400ºC, and then slightly reduces at 1500ºC. It was

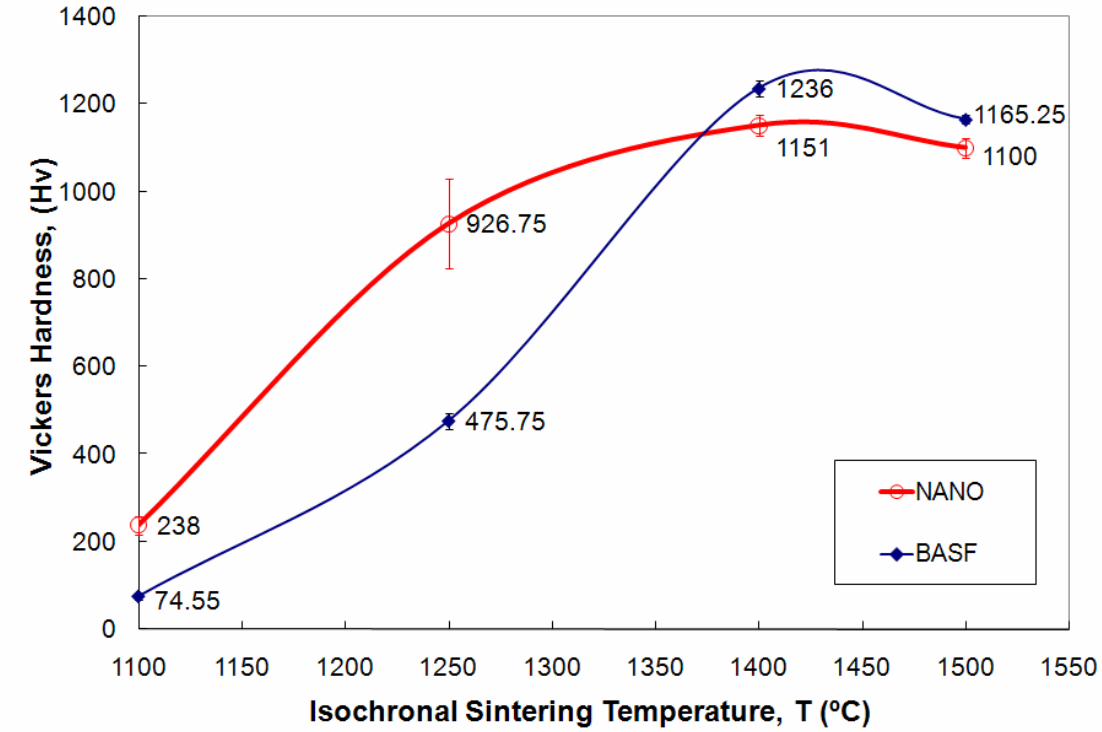

Figure 4-4 Hardness for one hour isochronal sintering, appeared as appropriate indicator for sintering degree, compared to shrinkage, mass lost and relative density

observed that the hardness values vary from 70 to 1250 Hv, more appropriate to reflect the sintering degree, when compared to shrinkage (~2-23%) and density (~93-99%). The standard deviation of hardness value also provided useful information about the sintering degree. For example, standard deviation for initial and final sintering stage was marginal, as the whole test body was homogenous, either as a weak connected particles, or strong sintered grains. The hardness noticeably deviated (>200 Hv) for NANO test piece at intermediate sintering stage, as the porosity level was high. If the surface underneath the indentation consists porosity that weakens the test surface, the indentation mark became bigger and caused low hardness reading. Hardness also directly manifest whether the material is useable with acceptable strength. Vickers hardness value relates to other material properties, such as the

material strength and toughness. Toughness in particular can be calculated from Vickers hardness test, with the measurement of crack lengths[92].

As both mass loss and shrinkage saturated depending on the binder content, and density could deviated due to pore structure changes such as open porosity at initial sintering stage and high grain coordination pore at final sintering stage, the three mentioned parameters were poor indicators of sintering degree. Thus in the following discussions, Vickers hardness will be used as the sintering indicator, with the support of FE-SEM micrographs to assess the morphology properties.

4.2 Sintering Behavior of Nanosized Y-TZP Processed by PIM

4.2.1 Isochronal Sintering with A Duration of 6 Minutes

Figure 4-5 shows the morphology evolution of NANO and BASF. After thermal debinding and pre-sintering at 900°C, the microstructure observed at the fracture surface of the NANO sample shows nanosized spherical particles with narrow size distribution. The BASF sample appears coarser, and less spherical in shape. Microstructures for the samples sintered at temperature of 1250ºC showed tubular and rounded pore structure at intermediate sintering stage. About 40% grains in the NANO samples have grown extensively to the size about 600 nm. BASF on the other hand, showed negligible grain growth with noticeable rearrangement and pore coalescence. As the sintering temperature increased to 1400°C, both the NANO and BASF appeared to be in final stage sintering with some remaining isolated pores. Significant densification was observed for both samples compared to those at 1250˚C.

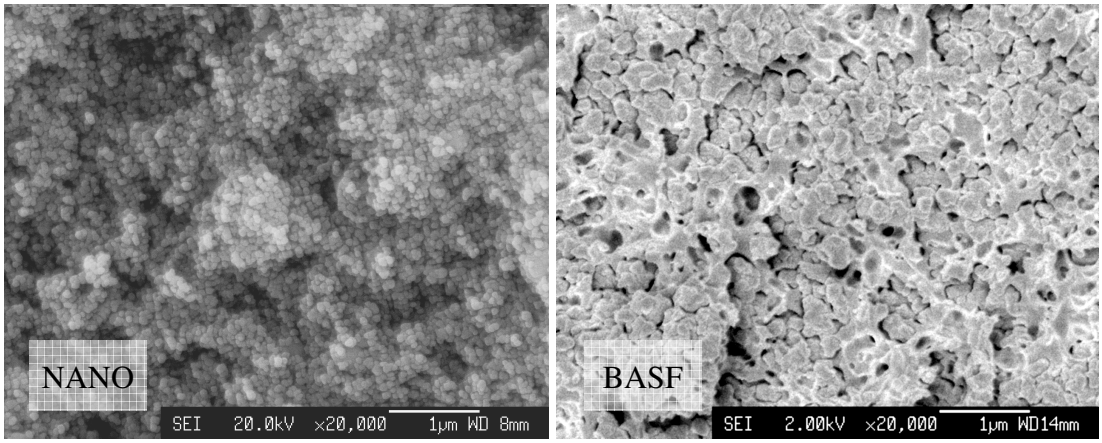

(a) Pre-sintering at 900ºC

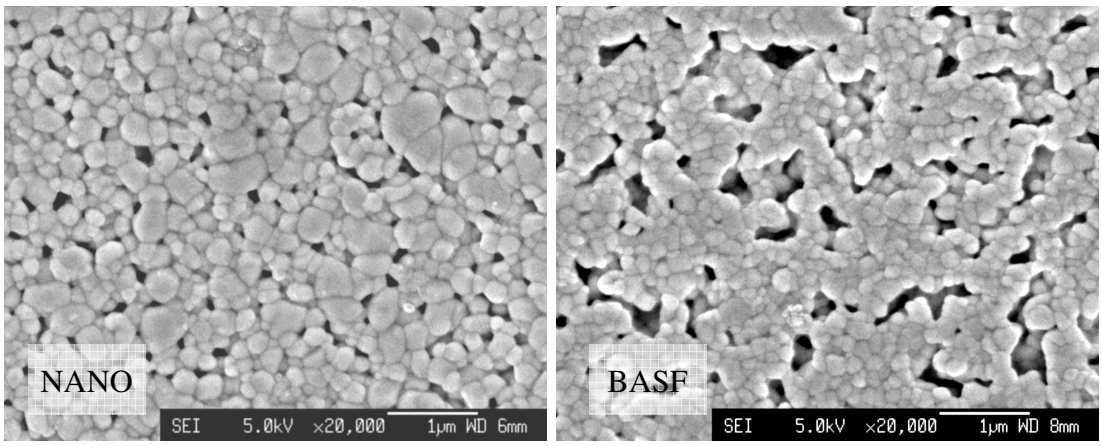

(b) 6 min sintering at 1250ºC

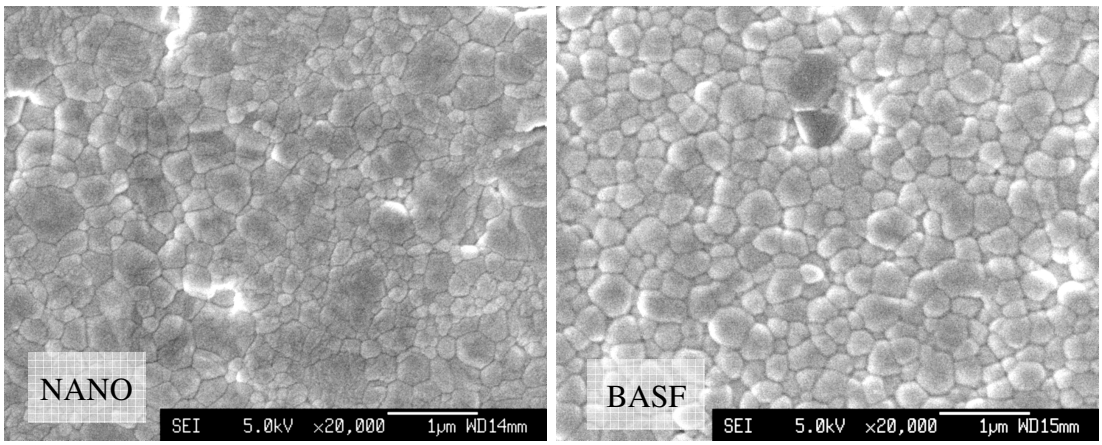

(c) 6 min sintering at 1400ºC

Figure 4-5 Micrographs of NANO and BASF samples at different sintering temperatures show evolution from powder compact (900˚C) to intermediate stage (1250˚C) and final stage (1400˚C)

The NANO sample did not grow much from 1250˚C, while the BASF sample showed noticeable grain growth comparing microstructure at 1250ºC and 1400ºC.

To quantify the grain growth behavior at different sintering temperatures, average grain size was measured in term of grain diameter, D or grain area, $\bar{A}$. Figure 4-6 compares both D and $\bar{A}$ as a function of sintering temperatures. Both D and $\bar{A}$ curves for BASF were almost parallel, where $\bar{A}$ is almost equal to $\pi/2(D/2)^2$, due to the nature of their measurement techniques. Some deviations were expected in the relationship of D and $\bar{A}$ due to the differences in grain shape. Both D and $\bar{A}$ are interchangeable and will be used for comparison in subsequent discussions, subject to suitability. The relationship between D and $\bar{A}$ also causes the relative grain growth differs by a power of two, which $\bar{A}/\bar{A}_0 = (D/D_0)^2$.

As shown in Figure 4-5 and 4-6, grain growth is rapid for the NANO, especially from 900 to 1250˚C. It grew more than 5 times, from 60.5 to 313 nm, and failed to retain its nanostructure at such a low temperature, which still at intermediate sintering stage. Further sintering from 1250ºC showed relatively small grain growth. From 1250 to 1400˚C, grain growth was only 23%, and about 50% to 1500ºC. Conversely, BASF grew slowly, about 25% from 900 to 1250˚C, followed by 34% to 1400ºC and 20% to 1500ºC. The overall growth is only two times of initial size, much lesser than the growth of NANO from 900 to 1250ºC.

Figure 4-7 compares the relative grain growth of the NANO and BASF sintered at isochronal condition with other published results[4, 9, 23, 54, 93]. All nanosized powders show exponential grain growth, regardless of initial powder size and holding

duration. Isochronal sintering started from low temperature thus covered sintering from initial to final stage. For example, Theunissen et al. reported slow grain growth for 8 nm 3Y-TZP from 500-1050˚C [93], where grain boundary slip and grain boundary diffusion were presumed as the main densification mechanism. The grain growth increases from 1100˚C onwards and the grain volume diffusion was assumed to be the dominated grain growth mechanism, in view to the high density (95%) measured at this stage. The 8 nm powder grew about 13 times to 102 nm at 1200˚C. Grain growth is usually slow initially due to pore pinning effect, followed by exponential growth that corresponds to final sintering stage where porosity is minimal, thus less pore pinning effect. However, referring to Figure 4-5 (b), the amount of porosity is high, and the connected pore structure indicates intermediate sintering stage. The extensive growth observed at this stage hence cannot be explained by pore pinning effect. The corresponding measured density was 98%, due to the connected pore channel that reduced the mass volume measured using Archimedes method. No microstructure for sample sintered at 1200˚C was available in Theunissen report for comparison. Whether the high density measured by Archimedes method in mercury was 5% closed pore without open pore channel was not known. If comparing only the measured density and final grain size, both 8 nm and 50 nm powder appeared to follow the same growth behavior. Therefore, grain growth of nanosized powder is generally high during initial sintering stage, inexplicable by pore pinning effect, which implies a different growth mechanism from its coarse counterpart.

Exceptionally, the growth curves for 27 nm powder[9] was below 50 nm NANO. This may be attributed to the different packing conditions, or the holding

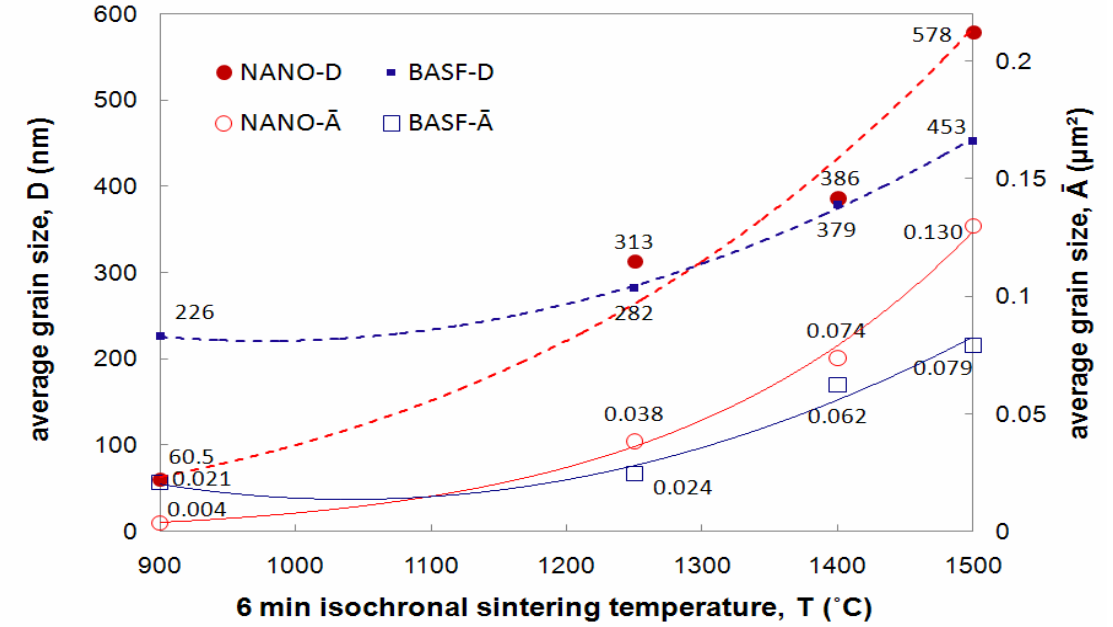

Figure 4-6 Average grain size as a function of isochronal sintering temperature, where NANO demonstrate extensive grain growth during initial sintering stage, as compared to BASF

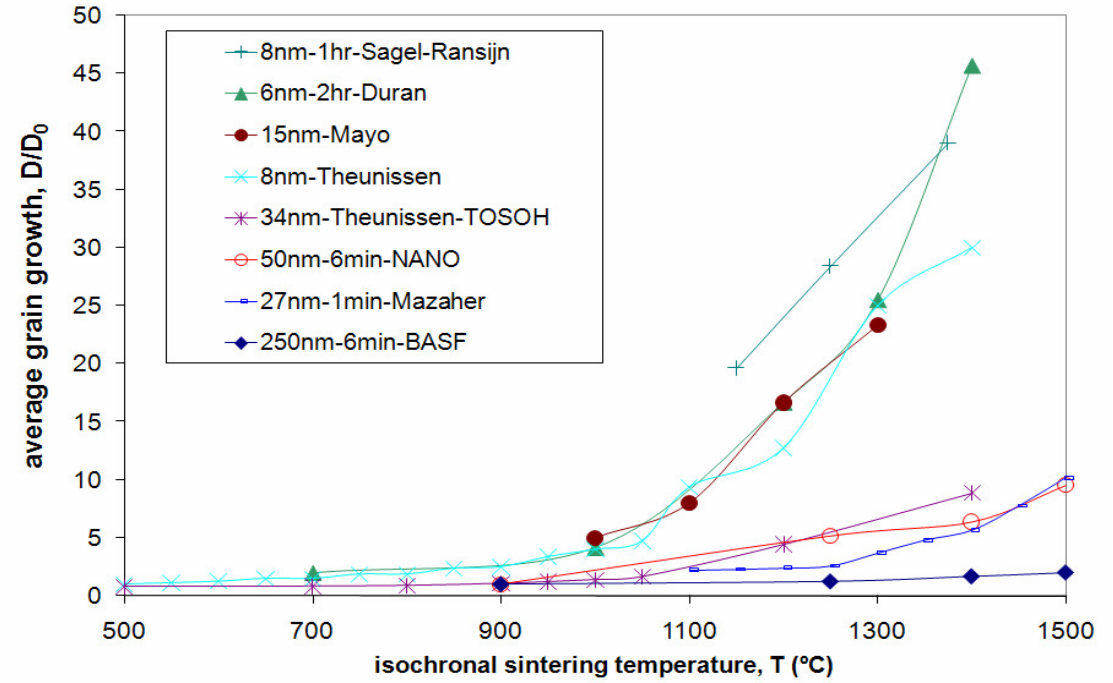

Figure 4-7 Relative grain size as a function of isochronal sintering temperature, in comparison with prior works, shows exponential growth, depending on initial size and sintering duration

durations. Loose packing condition was inherent after debinding process of powder injection molded parts. Assuming homogenous packing of 41% solid loading feedstock, after binder removal, the green density was 41 vol. %, while 150 MPa compaction of 27 nm powder resulted in 45% green density. High green density compact is desired to control the grain growth as it is likely to be more uniformly packed, thus unlikely to cause exaggerated grain growth[94]. In other words, the coarse grains observed in the NANO sample in Figure 4-5 (b) may be a result of inhomogenous packing condition. If this is true, one should expect to see exaggerated grain growth in the BASF sample at 1400˚C, resultant of the heterogeneous packing condition observed in Figure 4-5 (b). Opposed to prediction, the BASF only grew to 379 from 282 nm. Therefore, extra 5 minutes holding in isochronal sintering appeared to be responsible for the higher growth in the NANO sample, rather than the packing condition. This is rational as grain growth is significant during initial sintering stage. Also, even though 5 minutes is short, but it is 5 times longer than one minute and can cause significant grain growth. The packing condition inherent from debinding process did not appear to cause significant difference in sintering behavior of nanosized powder. Generally, the finer starting size and/or longer sintering duration caused more extensive growth. The decrease in powder size of nanosized powder was better accounted for the exaggerated grain growth.

4.2.2 Irregular Shaped Grains

As discussed in Section 1.3.2, grain growth via curvature migration yields

smooth and straight grain boundary. In Section 1.4.2, irregular shaped grains thus indirectly suggests grain growth is via grain coalescence[67, 68]. Figure 4-8 highlights some irregular shaped grains that observed from the microstructure of NANO sample sintered for 6 minutes at the temperature of 1350˚C. As discussed in Section 1.4, irregular shaped grain is thermodynamically unfavorable, therefore unlikely to grow from curvature migration. Previous reports suggested that irregular shaped grains were the result of grain coalescence. Two grains grow to about 1 μm, with ridged grain boundary, implies that the growth is not via curvature migration that will yield smooth grain boundary. Others smaller grains have irregular grain shapes, like elongated shape, L shape or X shape. Although grain boundary anisotropy was also reported to cause abnormal shaped grains, usually presence as exceptionally large angular shaped grains in the matrix of fine grains, the shape are differ from these irregular shaped grains observed in Figure 4-8. Furthermore, these abnormal grains often observed in materials that experience certain extend of liquid phase sintering and have large difference interface energy, such as tungsten carbide material. The abnormality also becomes severe as sintering proceeds due the anisotropy in interface energy. On the other hand, the irregularity only observed in certain stage, which so far only found in sample sintered for 6 minutes at 1300ºC. The disappearance of irregular shaped grains during sintering process suggests that these boundaries are not help in energy minimization unlike the case of anisotropy. Therefore, the presence of these irregular shaped grains is unlikely due to anisotropy of grain boundary energy, may be a result of coalescence of several nanosized powders.

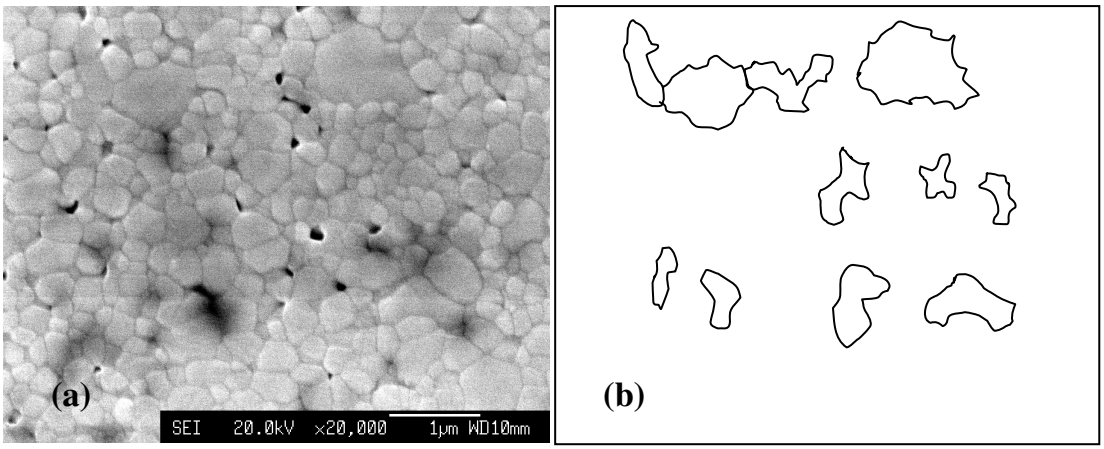

Figure 4-8 (a) microstructure of sample sintered at 1350˚C for 6 minutes, with some of the irregular shaped grains being traced out at the sketch (b), suggesting grain growth through grain coalescence

4.2.3 Isothermal Sintering at Temperature of 1300ºC

To further study the sintering behavior, the nanosized and coarse powder were evaluated through isothermal sintering. Figure 4-9 demonstrates the morphological evolution of the NANO and BASF isothermally sintered at temperature of 1300ºC. The overall size of the NANO was larger than the initially coarse BASF at all durations. One hour sintering achieved intermediate sintering stage where pores are connected in tabular shape. Some NANO grains have grown to 1 μm at this stage. After 10 hours sintering, both NANO and BASF achieved final stage sintering. Most of the pores shrunk and closed and the remaining pores were isolated at grains junction. Grain growth was slow from intermediate stage to final stage. 40 hours sintering at 1300ºC had marginal effect on grain growth and pore closure.

Preliminary results on isochronal sintering suggest nanosized powder, the NANO grow differently from its coarse counterpart, BASF. Figure 4-10 plots the

average grain size as a function of isothermal sintering duration. The NANO showed over 6 times growth to 379nm, after 6 minutes of sintering at temperature of 1300˚C. It is noted that the measured grain diameter after 1 hour sintering is slightly smaller than 0.1 hours, which is 365 nm and 379 nm, respectively; whereas grain area measurement shows a 0.01 μm^2 increment. Before multiplied by correction factor, the difference was less than 4 nm. This small deviation was acceptable as error from linear intercept method. Subsequent growth was slowed down, where size at 40 hours (2400 minutes) was 628 nm, grew about 1.5 times from 0.1 hour (6 minutes). Absence of such sudden growth at initial sintering stage results in overall growth of 100% after 40 hours for BASF. The growth curves for both NANO and BASF are quite similar, with a slow growth plateau after 1 hour. The significant difference was the extensive growth during initial sintering stage that observed only in the NANO samples.

Figure 4-11 compares the isothermal growth behavior of the NANO and BASF with prior works [4, 93]. Generally, the lower the sintering temperature, the lesser the grain growth was. The 8 nm powder was isothermally sintered at 1000-1275˚C. Except for 1275˚C, other sintering temperatures resulted in a slow growth plateau, like the NANO samples. For example, 1050˚C isothermal sintering result from Theunissen et al.[93] suggested that densification be the most important mechanism sintering duration below 7 hours. The density and grain size increased to 96% and 60 nm, respectively. In other words, the 8 nm powder grew by a factor of 7.5 during densification stage. This was in strong agreement with isochronal sintering results, where extensive grain growth was occurred at initial sintering stage. Coarse counterpart however did not subject to such extensive grain growth during

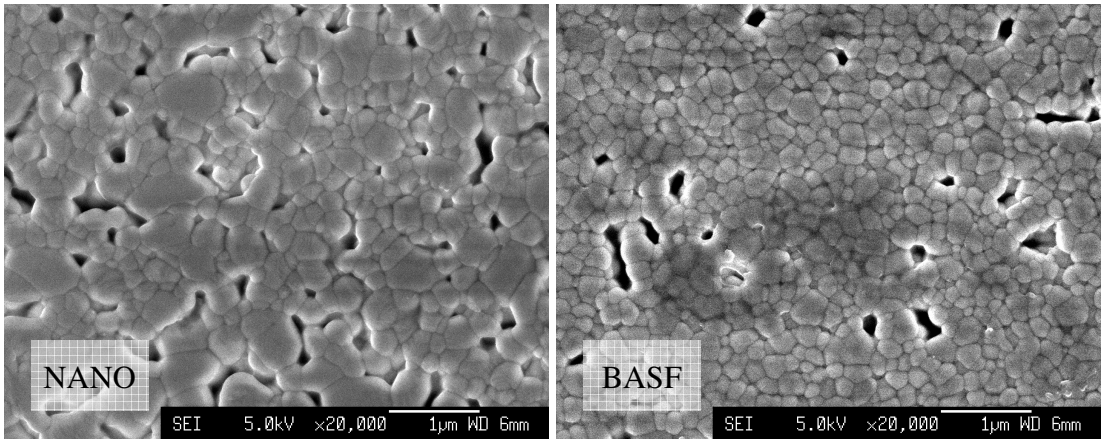

(a) 1 hour sintering at 1300ºC

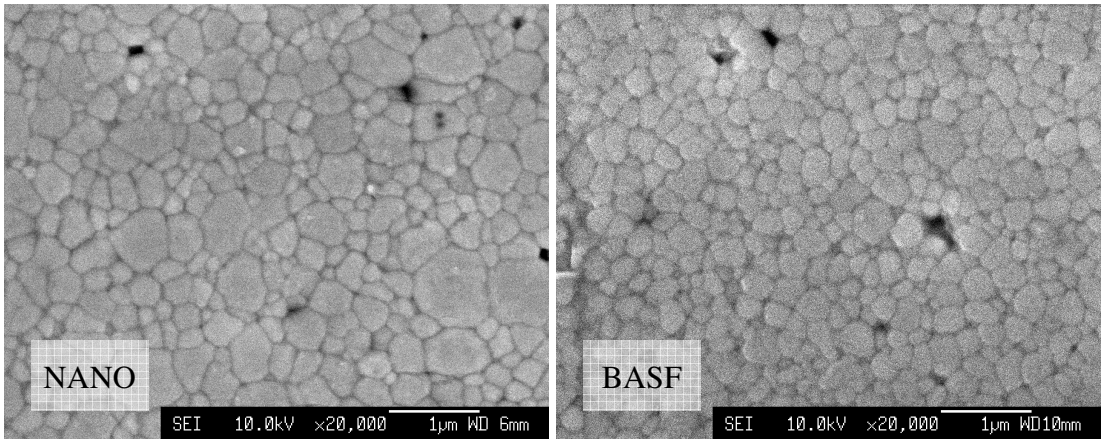

(b) 10 hours sintering at 1300ºC

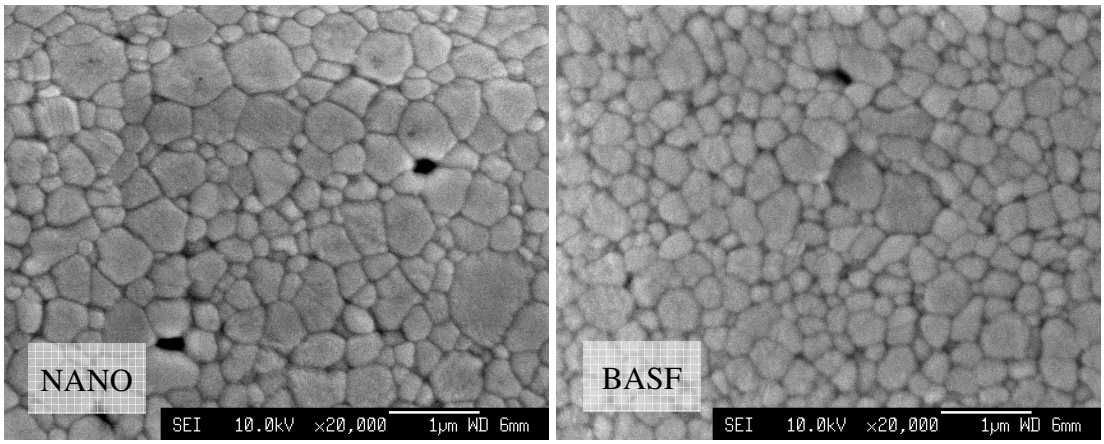

(c) 40 hours sintering at 1300ºC

Figure 4-9 Isothermal morphology evolution of NANO and BASF samples, NANO appeared coarser than BASF despite the starting nanosize

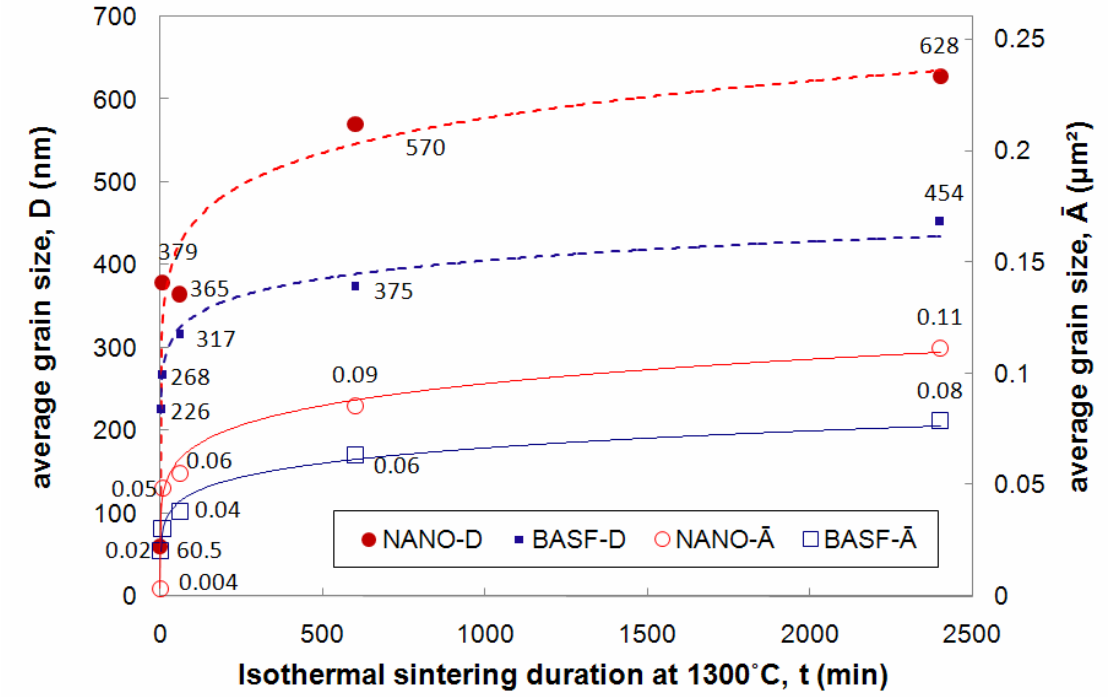

Figure 4-10 Average grain size as a function of isothermal sintering duration, where NANO demonstrates extensive grain growth after 6 minutes, follows by slow grain growth as BASF.

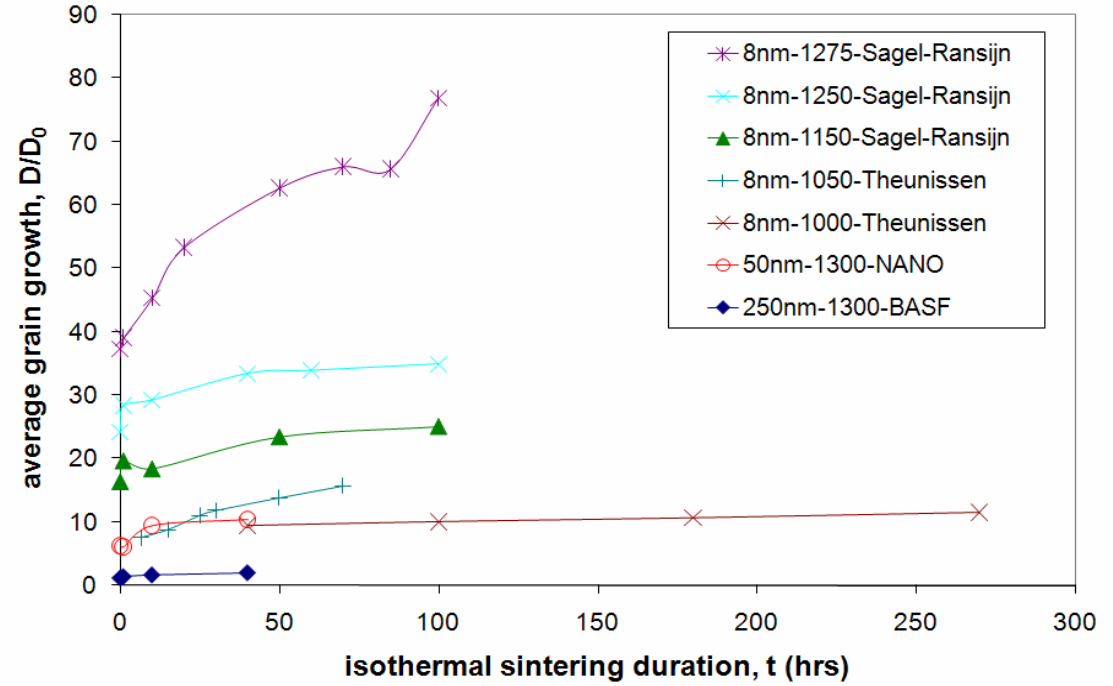

Figure 4-11 Relative grain size in comparison with prior works generally shows a rapid initial grain growth, follows by a slow growth plateau

densification. The reason of this extensive grain growth thus is likely related to grain coalescence, with the support of irregular shaped grains.

4.2.4 Relationship between Grain Size and Hardness Value

The classic relationship between grain boundaries and material strength was published by Hall and Petch around 1950 with conclusion that the grain size dependence yield strength, σ_y can be expressed as equation below, where K is a constant and d is the mean grain size:

$$\sigma_y = \sigma_0 + \frac{K}{\sqrt{d}} \tag{4-1}$$

According to Hall-Petch theory, mechanical properties could be improved with decreasing grain size. This has been confirmed theoretically and experimentally in many metallic materials[95] and 3Y-TZP[1, 2] thus motivates the research in grain refinement. However, Hall-Petch relationship may not be valid for some of the nanocrystalline materials[96-99], which means that finer grain size does not always improve the material property. Therefore, material property measurement is important in the study of nanocrystalline materials. To identify the relationship between grain size and material property, Vickers hardness for the NANO and BASF samples, in particular is compared with their average grain size in Figure 4-12 and 4-13, for isochronal and isothermal sintering, respectively. Despite higher grain growth for the NANO than BASF samples, the hardness increased drastically from about 20 Hv to

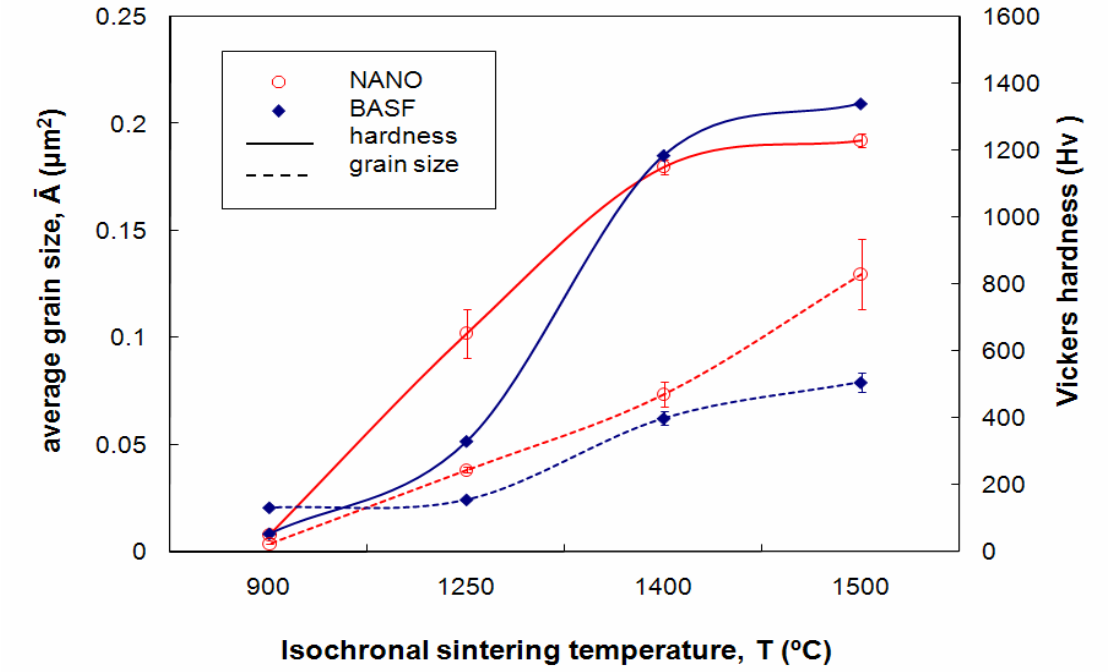

Figure 4-12 Average grain size and Vickers hardness as a function sintering temperature with one hour sintering duration at the sintering temperature

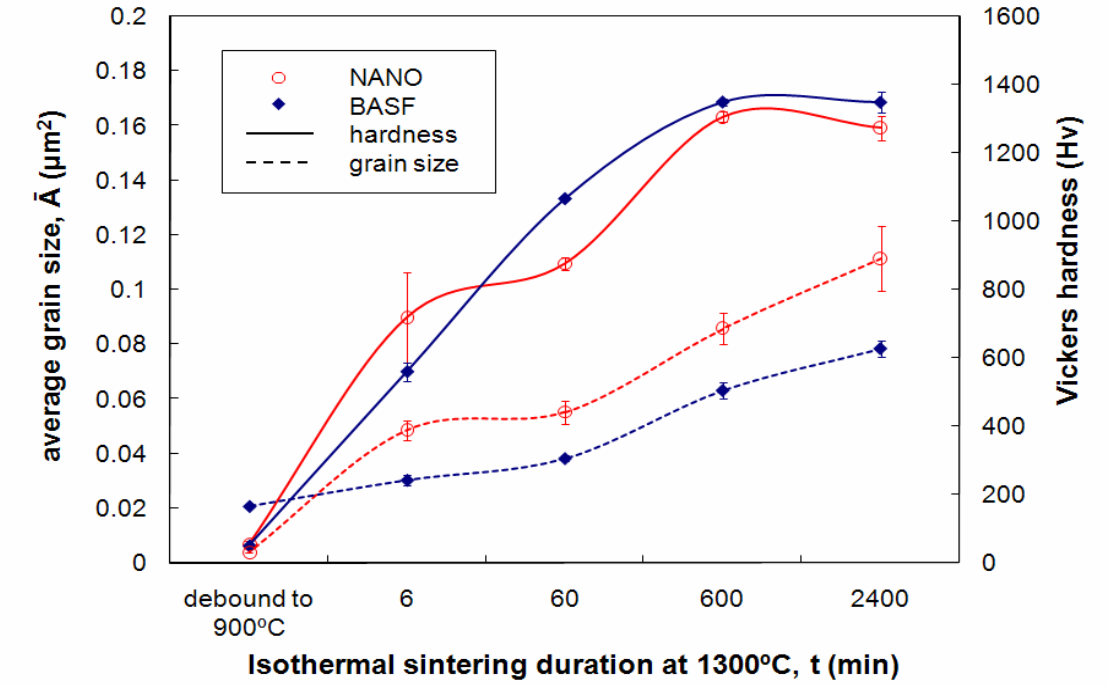

Figure 4-13 Average grain size and Vickers hardness as a function of sintering duration at the sintering temperature of 1300ºC

1300 Hv with increase sintering temperature and holding duration. At one glance, it was true that the smaller the grains size, the harder the material, where BASF was finer and harder than NANO, except at the debound and initial sintering stage. Debinding and pre-sintering to 900˚C removed most of the added binder in both samples. At this stage, both the samples were weak powder compacts, with the measured hardness at about 50 Hv. 6 minutes sintering at temperature of 1250˚C increased the hardness of the NANO samples to about 625 ± 72 Hv. At such short duration and low temperature sintering, the NANO samples achieved higher degree of sintering than the BASF where the BASF samples only achieved 331 ± 9 Hv. The increment in hardness is associate density and grain size. However, when focus on BASF in Figure 4-12, hardness is less dependent on grain size. The hardness of BASF increases about 280 Hv, without much grain growth (0.003 μm^2). The higher hardness for the NANO samples suggests that the sintering stage approaching final stage, while the BASF samples was in the beginning of intermediate stage. This was in qualitative agreement with micrographs shown in Figure 4-5 (b). Again, micrograph for the NANO demonstrates denser structure compared to the BASF which contributes to higher hardness. The high standard deviation for the NANO samples may attribute to the differential sintering degree, demonstrated by different grain size.

When focused on either the NANO or BASF samples, the increased grain size was corresponding to the higher sintering degree. Higher sintering temperature or holding duration caused morphological evolution from powder compact to initial stage, intermediate stage and eventually final stage. This was parallel with the increase in sintering degree and average grain size. Both the grain size and hardness

were increasing with the sintering duration, except for 40 hours. When referred to Figure 4-9, both 10 and 40 hours (600 and 2400 minutes) sintering led to final stage sintering. Increase in grain size for both cases impaired the measured hardness.

Hall-Petch theory is thus valid only when the compared grain sizes were at the same sintering stage, such as final sintering stage. Grain size is small during initial sintering stage with weak bonding between particles, on the other hand material property increase together with increment in grain size in final sintering stage. Therefore, a best judgment of the Hall-Petch relationship is comparing the hardness of fully densed compact with different grain size. Also, Hall-Petch theory may not applicable to nanostructured materials as inverse Hall-Petch relationship for materials in nanometer regime has been documented[99-104]. This implies that the refined grain size may not directly manifest the improved properties. As suggested in Section 4.1, assessment on material and morphology properties is necessary to justify the contribution of grain refinement in material property betterment.

4.3 Sintering Optimization with Two-Stage Sintering (2SS)

Grain growth is highly associates with sintering temperature. With lower temperature, finer grain size can be obtained. Two-stage sintering (2SS) consists a short high temperature sintering to activate the sintering mechanism, followed by a long dwelling at a lower temperature to promote densification and limit grain growth. Lee[105] applied this sintering profile to the PIM sample with 82 wt. % or 41 vol. % solid loading and managed to obtain a finer microstructure. The sintering profile was

5 minutes at 1500ºC followed by 1300ºC for 10 hours. The bending strength was reported 4 times higher than that of the sample with a normal single stage sintering profile and was attributed to the refined microstructure. The average grain size is 0.59 µm or about two times grain growth. However, the initial particle size at 0.27 µm was relative high compared to the 50 nm that will be used in this study. Chen and Wang have successfully retained the final microstructure of Yttria at 60nm, or 4-6 times growth using 2SS[106]. Mazaheri et al. applied 2SS on 27 nm 3Y-TZP powder recently[9]. The optimum 2SS profile was identified as one minute sintering at 1300˚C followed by 1150˚C for 30 hours. Near fully dense compacts at grain size less than 110 nm were produced. The key factor for a success 2SS is high initial density. As documented earlier[9, 106], density as high as 75% and 83% relative density was to be obtained at first stage, to avoid the final stage grain growth. In this section, the effectiveness of 2SS on nanosized 3Y-TZP processed by PIM will be discussed and the optimum sintering profile will be determined.

4.3.1 ISO-T_2 versus 2SS-1500˚C/T_2

Two-stage sintering, 2SS in this section is designed where T_1=1500ºC and T_2 varied between 1100 to 1500˚C, as shown in Figure 4-14. 2SS-10 hours means holding of 10 hours at T_2. 2SS1500/1100 significantly increased the hardness of NANO samples compared to isothermal sintering (ISO). With initial short sintering at 1500ºC, 2SS-1500/1100 yielded hardness by a factor of 5 times than ISO-1100. This could be understood as holding temperature at 1100ºC was insufficient for sintering to

proceed to final stage. However, with additional 6 minutes holding at temperature of 1500ºC, followed by rapid cooling down to 1100ºC, the sintering was activated and holding at 1100ºC continued the sintering process and increased the hardness to 1137 Hv. Generally the 2SS-1 hour and 2SS-10 hours curve were overlapping. This implies that the one hour holding at second stage was adequate and prolong duration at this stage did not lead to further increase in sintering degree. As T_2 increased, difference in the hardness between ISO, 2SS and 2SS-10 hours was becoming smaller. This is rational as the material will be sintered at high temperature and the physical properties will be improved. 10 hours holding time at temperature of 1500ºC however marked a decrease in hardness. This could be due to grain and pore coarsening after prolonging sintering at elevated temperature, as discussed in Section 4.1.2. 2SS at sintering temperature of 1500ºC in this case is ISO-1500-10 hours as the

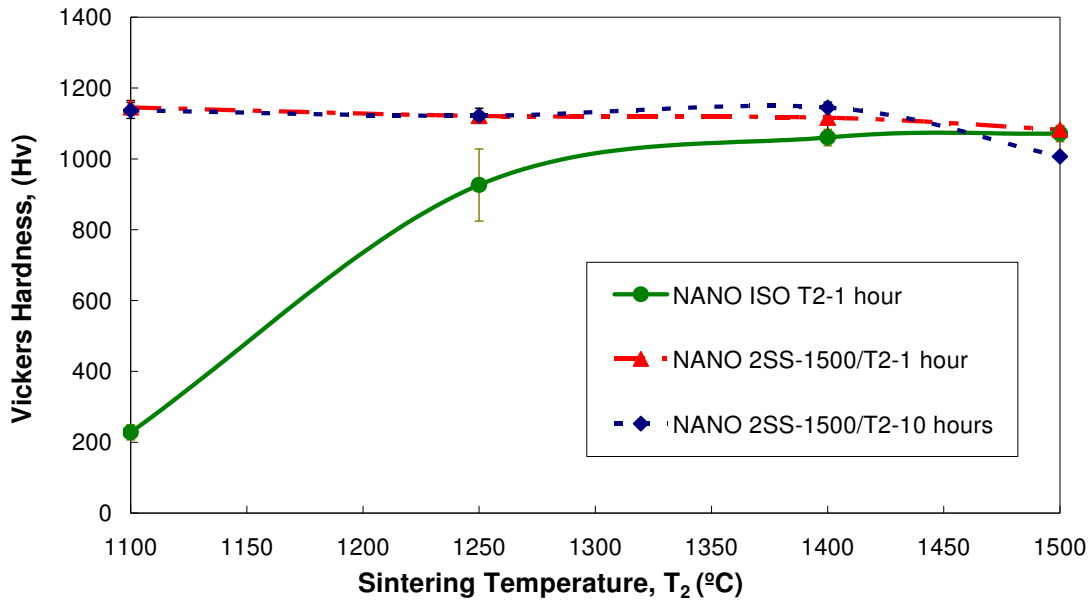

Figure 4-14 Hardness after two-stage sintering (T_1=1500ºC) and isothermal sintering (T_1=T_2). Longer holding time at T_2 does not increase the hardness, and 10 hours holding time at 1500ºC causes a decrease in hardness

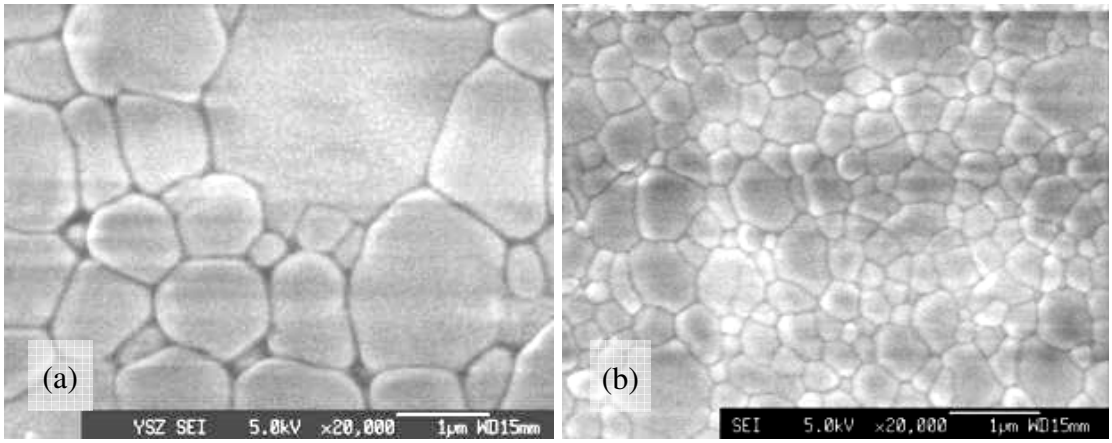

Figure 4-15 (a) ISO-1500-10hours shows exaggerated grain growth and (b) 2SS-1500/1100-1hour with finer grain size, while 1 hour sintering at temperature of 1100˚C shown in Figure 4-2 demonstrated a porous structure in initial sintering stage

T_1=T_2. Sintering at 1500ºC for 10 hours is too much for NANO. The microstructure after ISO-1500-10 hours (Figure 4-15 (a)) grown significantly, when compared to 2SS-1500/1100-1 hour (b). These results indicate that 2SS can obtain the desired sintering degree as ISO at reduced sintering temperature. Prolonging second stage holding is unnecessary.

4.3.2 Optimized Two-Stage Sintering Profile

In view of the higher sinterability of nanosized powder, in the first stage sintering, the temperature can be lower than 1500ºC to further limit the grain growth. From the previous results, high hardness was mostly obtained between 1250ºC-1400ºC. A temperature interval of 50ºC was therefore investigated. T_2 was further reduced to 900ºC. ISO was reduced to 6 minutes holding time at sintering temperature

to reflect the dwelling effect. All results were compared to BASF samples and plotted in Figure 4-16. Interestingly, the 2SS curve for NANO is always above ISO. However both ISO and 2SS curves for BASF were almost overlapping. This suggests that 2SS was ineffective for BASF mainly due to the coarse initial particle size (228 nm) that has lower sinterability. Submicron size powder required high sintering temperature, like 2SS 1500/1300[105]. On the other hand, both 2SS-1400/900 and 2SS-1350/900 achieved hardness above 1200 Hv for NANO samples. First stage sintering temperature at 1250ºC is too low to activate the sintering and yields low hardness

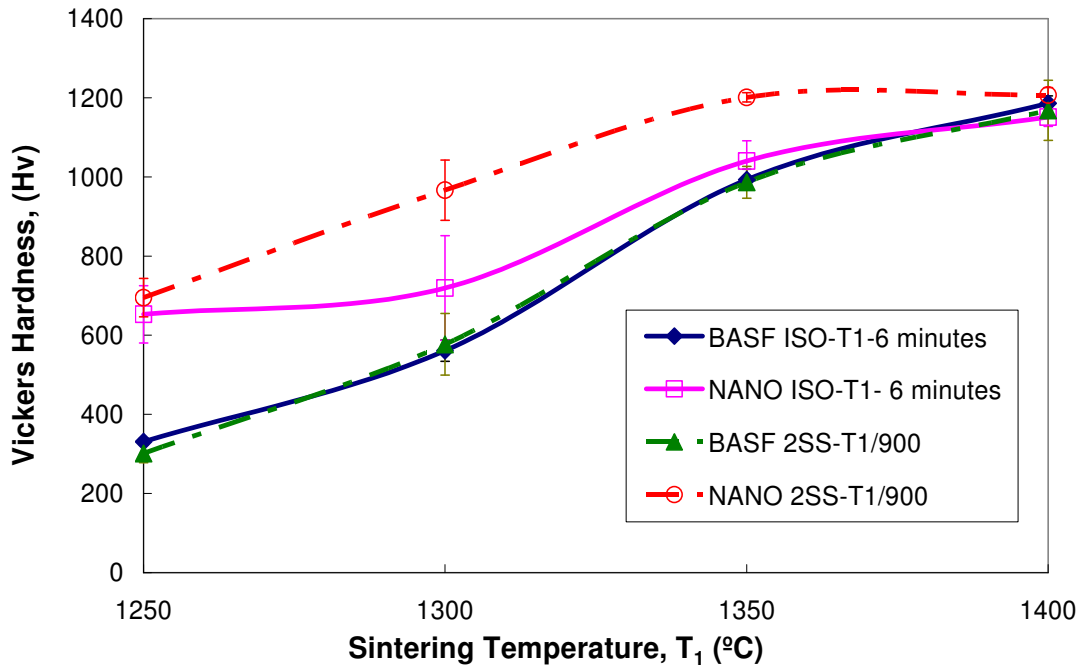

Figure 4-16 Hardness of samples sintered via two-stage sintering (T_2=900ºC) and isothermal sintering (T_1=T_2). Two-stage sintering significantly increase the hardness of NANO samples, in contrast to BASF samples that has negligible improvement

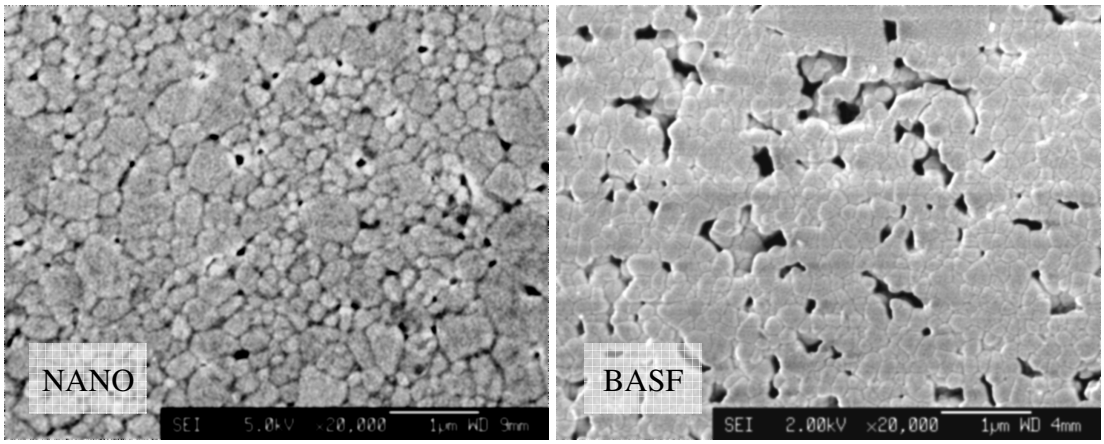

(a) 2SS-1300/ 900ºC

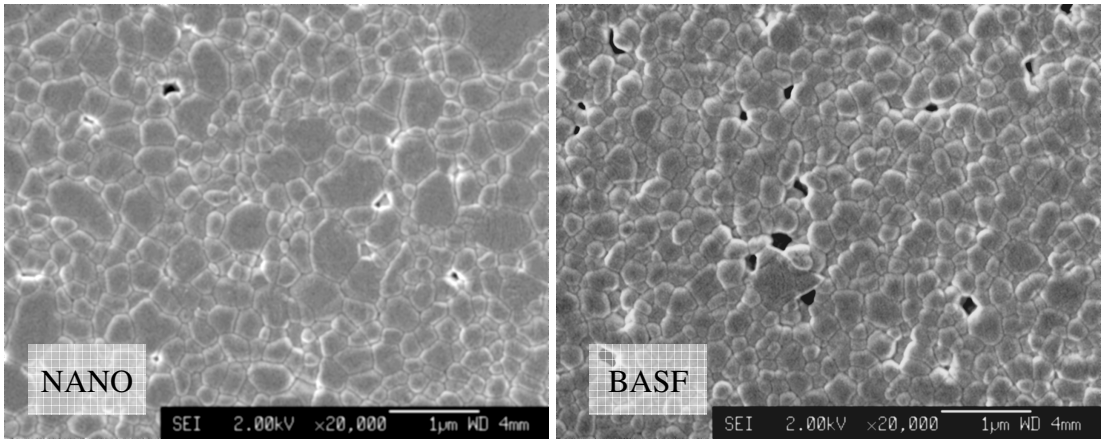

(b) 2SS-1350/900ºC

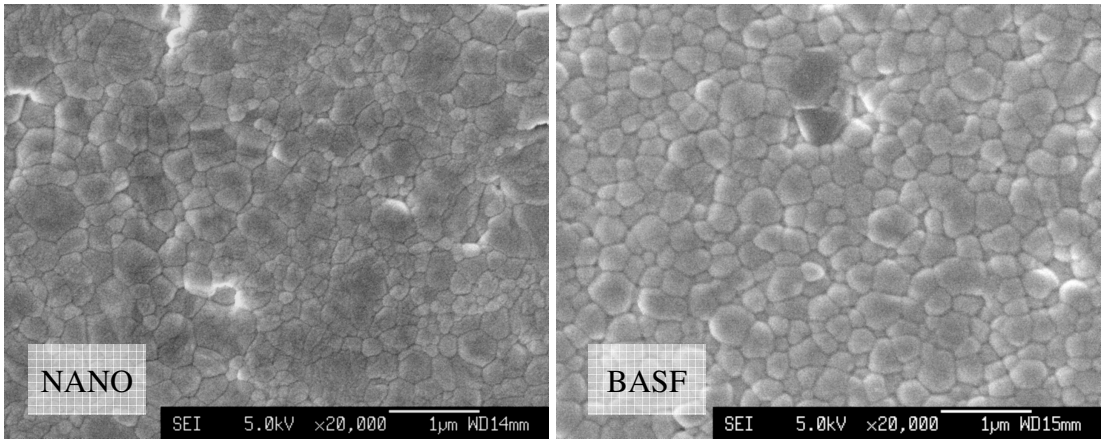

(c) 2SS-1400/900ºC

Figure 4-17 Microstructure evolution through two-stage sintering profile, which with 2SS-1350/900, both NANO and BASF show closed pore structure at final sintering stage, with finer size than 2SS-1400/900

(<700 Hv). Figure 4-17 compares the microstructure of NANO and BASF at different first stage sintering temperatures. The NANO appeared to reach final sintering stage with 2SS-1300/900, while the BASF only achieved final stage sintering with 2SS-1350/900. Even though both samples reach final stage sintering with 2SS-1350/900, NANO is about 200 Hv harder than that of the BASF. Table 4-1 compares the average grain size and density of the NANO and BASF. It can be observed that even with finer grain size, the BASF did not achieve better property than NANO. This may be attributed to the lower density of the BASF than that of the NANO, which are 93.7% and 95.9%, respectively. The microstructures in Figure 4-17 (b) show slightly more residue pores in BASF sample than NANO. Porosity is detrimental to the material properties. This means that the porosity has greater damaging effect than the contributing effect of finer grain size to the material properties. This again suggests that material property measurement, such as Vickers hardness and morphological property are important to study the sintering behavior, besides grain size and density.

Table 4-1 Density and grain size for two-stage sintering BASF and NANO samples, reduction in density or increment in average grain size, both have adverse effect on hardness

Two-stage sintering		2SS-1300/900	2SS-1350/900	2SS-1400/900
BASF	relative density, %	96.2	93.7	97.1
	average grain size, nm	282	334	415
NANO	relative density, %	95.6	95.9	99.5
	average grain size, nm	390	403	461

2SS-1400/900 increased the density of NANO from 95.9% to 99.5%, with inevitablegrain growth from 403 nm to 461 nm, as compared to 2SS-1350/900. With the contributing effect of increment in density and the damaging effect of increment in grain size, the measured hardness was identical for both cases. With about 200 Hv higher than 2SS-1300/900, 2SS-1350/900, was defined as the optimum 2SS condition.

4.4 **Summary**

The results in this chapter suggest that sintering degree should be assessed by morphology and material property, in addition to common practice of measurement in density and average grain size. Sintering behavior of nanosized 3Y-TZP processed by PIM was characterized through isochronal and isothermal sintering. No noticeable difference in growth pattern for samples processed by PIM or other compaction methods. The microstructure evolution suggests that the NANO and BASF grow differently in initial sintering stage, where the NANO growth extensively at low temperature. One possible speculation for the extensive growth is grain coalescence, with the evidence of irregular shaped grains. Two-stage sintering, 2SS-1350/900 was defined as an optimized sintering profile for 50 nm 3Y-TZP, considering the high hardness with relatively short sintering cycle and sintering temperature.

CHAPTER 5 PHASE FIELD SIMULATION OF SOLID-STATE SINTERING

Chapter 3 showed an interesting behavior about nanosized powder that differed from its coarse counterpart, which was the extensive grain growth during initial sintering stage. Experimental result was limited to reveal the mechanism behind this extensive grain growth. Recently, phase field simulation arises as an important tool to get the insight of microstructure evolution. In this chapter, phase field simulation will be used to understand whether the reduction in size to nanometer range caused this extensive grain growth during initial sintering stage of nanosized powder.

5.1 Background of Phase Field Simulation

From the point of thermodynamic, microstructure evolution is driven by free energy minimization. Free energy minimization can be achieved with the reduction in the total grain boundary area, either via reduction in grain boundary curvature or increase in the grain size. This free energy minimization is a complicated process which involves various competing paths like surface diffusion, volume diffusion, vapor transport and grain boundary diffusion. With the fast development of high speed supercomputer system, complicated sintering process can be studied using a variety of computational techniques such as molecular dynamics simulation[107-113],

Monte Carlo simulation[114-124] and Finite Element simulation[125, 126]. These computer simulations have demonstrated their potential in the prediction of microstructure evolution and corresponding properties.

Among the computational techniques, phase field simulation is one of the emerging fields of mesoscale computational materials science that gives tremendous insight into the world of microstructure evolution. Figure 5-1 (a) shows the sharp interface profile that is often assumed in other computer simulation models. With sharp interface, properties are discontinuous at the interface and domains are described by the position of the interfacial boundaries that requires explicit tracking of moving interfaces. From a mathematical point of view, tracking moving interface explicitly causes difficulties when simulating multiple concurrent phenomena. Figure 5-1 (b) is the diffuse interface profile used in phase field approach to study a wide range of material phenomena such as solidification and grain growth. By this artificial, continuous phase field variable, phase field simulation excels from other computational techniques by avoiding explicitly tracking interfaces. With a set of phase field variables that represents the microstructure as continuous spatial and temporal functions, the interfaces position is implicitly traced by a contour of constant values of the phase-field variables. In the domains, the phase-field variables have a constant value, while at the interface, the transition is continuous. Thus the kinetic equations for the microstructure evolution are defined over the whole system. This important criterion of phase field approach enables examination of multiple concurrent sintering processes, including various diffusion paths and curvature migration in a competing manner.

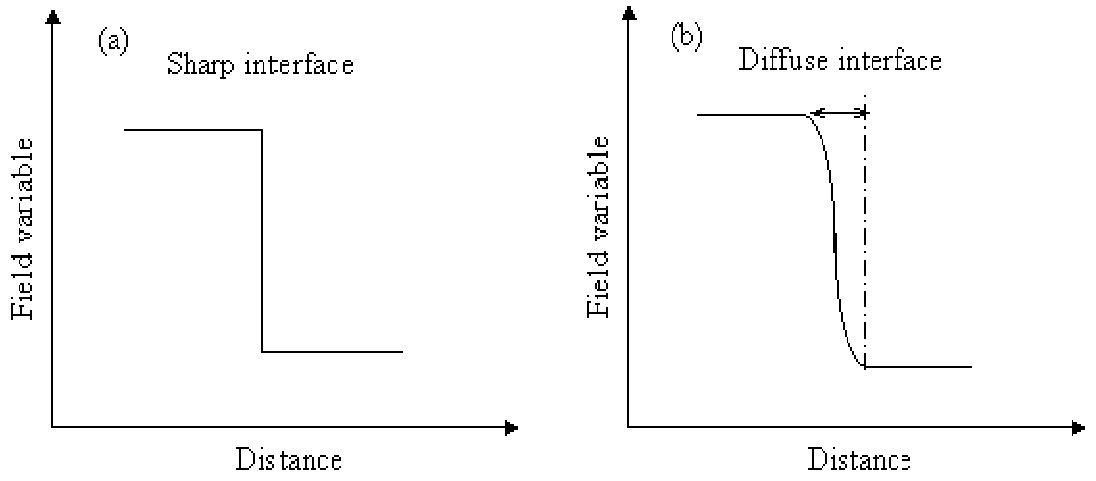

Figure 5-1 (a) the sharp interface and (b) diffuse interface can be distinguished as a function of field variable across a distance where interface is infinitely sharp or rapidly change by a continuous profile.

5.1.1 Governing Equations

The diffuse interface phase field approach is used to study the microstructure evolution observed in the experimental work. The free energy function as a function of temperature for a real system can be measured experimentally, if it is known, phase filed simulation can be directly used to predict the microstructure evolution[127]. The theoretical formulation is based on the thermodynamic of an inhomogeneous microstructure described by the diffuse-interface theory of Cahn and Hilliard[128] for conserved composition. The non linear diffuse equation or sometimes also called the time dependent Ginzburg-Landau equation for non conserved composition is proposed by Allen and Cahn[129].

The formulation for solid-state sintering was as previously presented by Wang[130]. The total free energy of a powder compact, F is described as a function of

the conserved mass density field and the non-conserved structural order parameter field. The mass density field ρ(x,t) and the non-conserved structural order parameter field η(x,t;α=1,2,…,p) are described across a range of length, x and time scale t, where the number of order parameter, p is equal to the number of particles in the powder compact. The mass density field represents the distribution of solid or pore when ρ(x, t)=1 or 0. The order parameter field η(x, t; α) specify the geometry and crystallographic orientation of the individual particle/grains. With these, the total free energy of the powder compact can be written according to equation (5-1).

$$F = \int_v \left[f(\rho, \{\eta(\alpha)\}) + \frac{1}{2}\beta_\rho \left|\nabla\rho\right|^2 + \sum_\alpha \beta_\eta \left|\nabla\eta(\alpha)\right|^2 \right] d^2 r \tag{5-1}$$

where free energy, F, is the summation of the local bulk chemical free energy, the surface and grain boundary energies over the diffuse interface regions of the field functions. The second and third terms are gradient energy terms that describe the energy contributions from surfaces and grain boundaries, respectively where βη and βρ are the gradient coefficients. The function f (ρ,) is the nonequilibrium bulk chemical free energy density that defines the homogeneous coexisting phases (solid and pore) and multiple solid domains (particles/grains of different crystallographic orientations). In this simulation, the local bulk chemical free energy function is approximated by a Landau-type polynomial potential, typically as in equation (5-2)

$$f(\rho, \{\eta(\alpha)\}) = A\rho^2(1-\rho)^2 + \tag{5-2}$$

$$B\left[\rho^2 + 6(1-\rho)\sum_\alpha \eta^2(\alpha) - 4(2-\rho)\sum_\alpha \eta^3(\alpha) + 3\left(\sum_\alpha \eta^2(\alpha)\right)^2 \right]$$

where A and B are constants, respectively, related to material and to grain boundary thickness. The exact form of the local bulk chemical free energy function is not important as long as it follows a double well potential. This Landau-type potential is plotted in Figure 5-2. It has the equilibrium value of mass density at $\rho = 0$ in pores and $\rho = 1$ in solid material. The equilibrium value of the order parameter vanishes in pores, i.e., $\{\eta(\alpha)\}_{\rho=0} = \{0, 0, \ldots, 0\}$, and is reached in solid at $\{\eta(\alpha)\}_{\rho=1} = \{1, 0, \ldots,0\} = \ldots = \{0, 0, \ldots,1\}$ of different crystallographic orientations. As shown in Figure 5-2, minimization of the local bulk chemical free energy ‘‘condenses’’ the spatial mass distribution into two phases: pores and solid particles/grains. This results in grain growth via curvature migration, as (1-1) in Section 1.3.

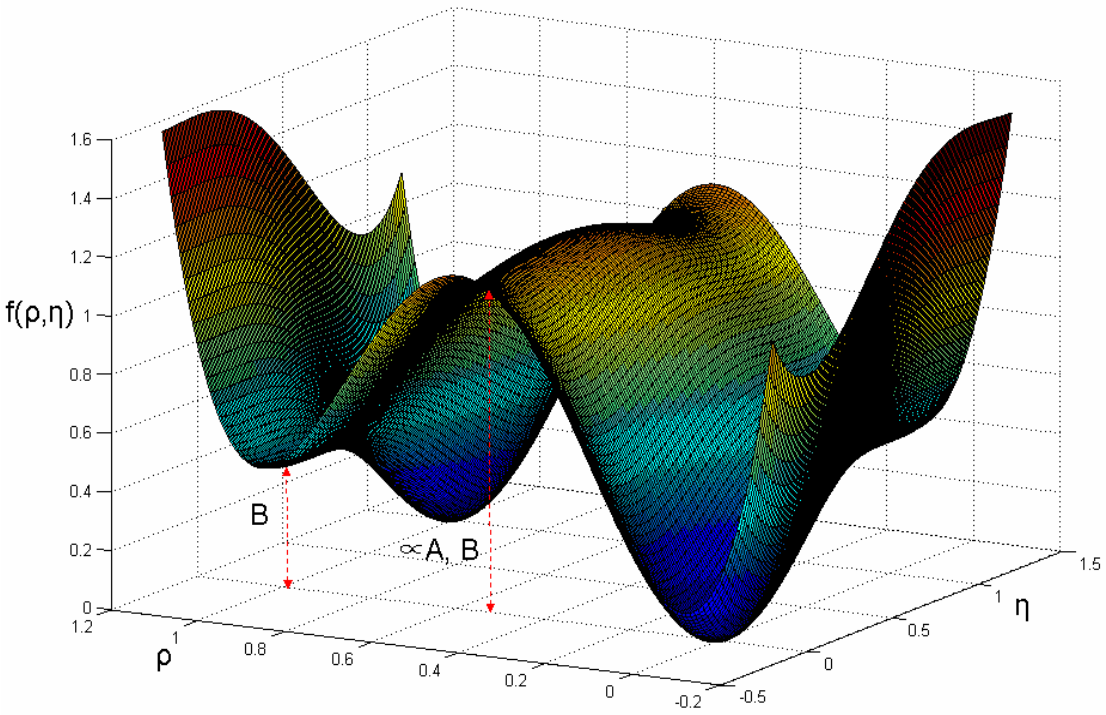

Figure 5-2: Local chemical free energy profile that condenses order parameter η to 1 when ρ=1, and η to 0 when ρ=0, the local minima has a value equal to constant B that contributes to the interface thickness.

Figure 5-3 (a) is the simplified 2-dimensional plot of Figure 5-2. The double well potential of (5-2) is clear, where constant B determine the change of free energy Δf, from higher energy state η =0 to the lower energy state η =1 and the activation energy, Q that proportional to constant A and B, is the energy barrier that needs to be overcome for this transition. Figure 5-3 (b) shows the plot of order parameter, η as a function of distance, x. Grain boundary formed when two or more interfaces meet as the η evolve smoothly from 1 in the grain, to 0 outside the grain. Constant B will determine how steep the transition from η =1 to η =0 and higher value of B results in a thinner grain boundary. The solid line is the diffuse interface profile with $B=B_1$, and dotted line for $B=B_2$, where $B_1>B_2$. By setting a η value as the grain boundary threshold, the grain boundary thickness that proportional to B can be defined. Thicker grain boundary corresponds to smaller grain size, or faster response time.

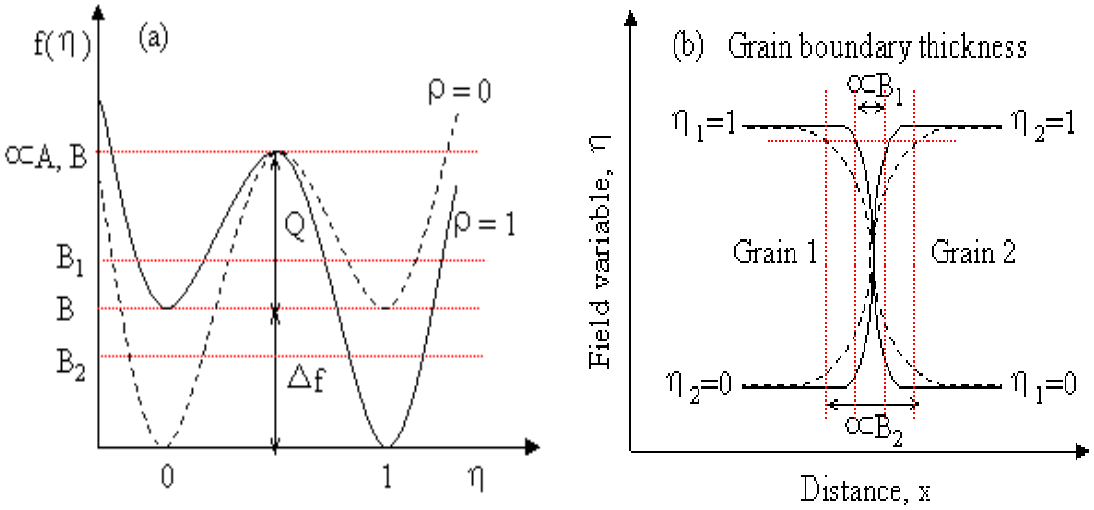

Figure 5-3 (a) the double well potential that condenses the order parameter to 0 or 1 (b) two or more interfaces will meet as the η evolve smoothly from 1 in the grain to 0 outside the grain and form grain boundary

The kinetics of this microstructure evolution is governed by two types of

continuum equations, which are the Cahn-Hilliard equation[131] and Allen-Cahn equation[129]. Cahn-Hilliard equation is a nonlinear diffusion equation that represents the conserved composition field by (5-3), which D is the diffusion coefficient.

$$\frac{\partial \rho}{\partial t} = \nabla.(D\nabla \frac{\partial F}{\partial \rho}) \tag{5-3}$$

With (5-1) and (5-2),

$$\frac{\partial \rho}{\partial t} = \nabla.\left\{ D\nabla\left[\frac{\partial}{\partial t}\left(\frac{1}{2}\beta_\rho |\nabla\rho|^2 \right) + \frac{\partial}{\partial t} f\left(\rho, \{\eta(\alpha)\}\right) \right] \right\}$$

$$\frac{\partial \rho}{\partial t} = \nabla.\left\{ D\nabla\left[-\beta_\rho \nabla^2 \rho + 2A\rho(1-2\rho)(1-\rho) + 2B\left\{ \rho - 3\sum_\alpha \eta^2(\alpha) + 2\sum_\alpha \eta^3(\alpha) \right\} \right] \right\} \tag{5-4}$$

The diffusion coefficient, D, can be described as a function of various diffusion paths involved in sintering as in (5-5). Dvol, Dvap, Dsurf and Dgb are the diffusivity coefficient for volume, vapor, surface and grain boundary diffusion, respectively.

$$D = D_{vol}\phi(\rho) + D_{vap}[1-\phi(\rho)] + D_{surf}\rho(1-\rho) + D_{gb}\sum_\alpha \sum_{\alpha\neq\alpha'} \eta(\alpha)\eta(\alpha') \tag{5-5}$$

$\phi(\rho)$ is a smooth function that condenses mass density to 1 or 0. Equation (5-6) is so used instead of the function used by Wang[130] to improve numerical stability during iteration if ρ(x,t) >1 or ρ(x,t) <0, as demonstrated in Figure 5-4.

$$\phi(\rho) = \frac{1}{2}\left[1 + \tanh(8\rho - \frac{1}{2}) \right] \tag{5-6}$$

The Allen-Cahn equation is the time-dependent Ginzburg–Landau structural relaxation equation for non-conserved structural order parameter fields by (5-7), where L is a constant related to the mobility of grain boundary migration.

$$\frac{\partial \eta(\alpha)}{\partial t} = -L\frac{\partial F\{\eta(\alpha)\}}{\partial \eta(\alpha)} \tag{5-7}$$

Again combine with equation (5-1) and (5-2),

$$\frac{\partial \eta(\alpha)}{\partial t} = -L\left\{\frac{\partial}{\partial \eta}\left(\frac{1}{2}\beta_\eta \left|\nabla \eta(\alpha)\right|^2\right) + \frac{\partial}{\partial \eta} f\left(\rho, \{\eta(\alpha)\}\right)\right\} \tag{5-8}$$

$$\frac{\partial \eta(\alpha)}{\partial t} = L\left\{\beta_\eta \nabla^2 \sum_\alpha \eta(\alpha) - 12B\left[(1-\rho)\sum_\alpha \eta(\alpha) - (2-\rho)\sum_\alpha \eta^2(\alpha) + \sum_\alpha \eta^2(\alpha)\sum_\alpha \eta(\alpha)\right]\right\}$$

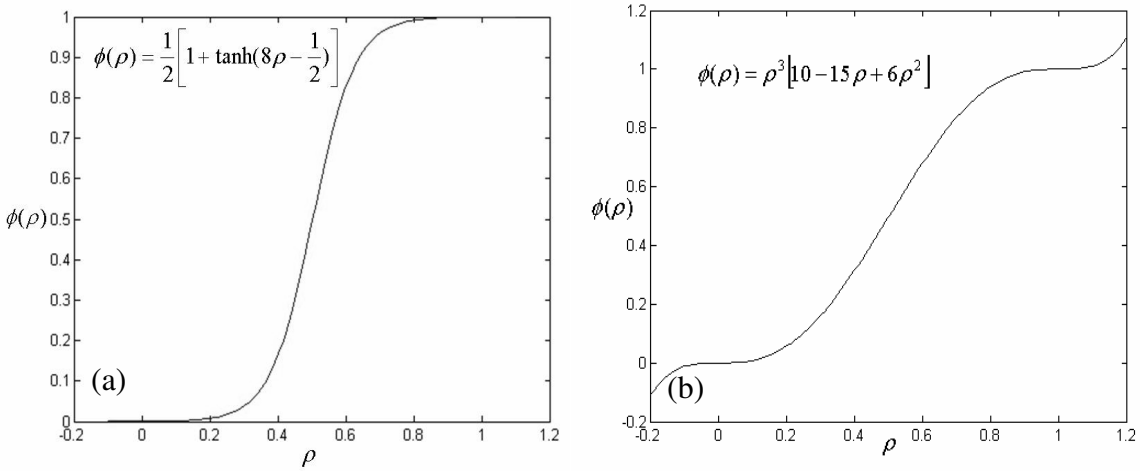

Figure 5-4 Function (a) that always condenses mass density, $\phi(\rho)$ at 1 for ρ=1 and 0 for ρ=0, is used instead of (b) so to always has local extrema at ρ=1 and ρ=0 in case ρ evolve beyond the range of 0≤ρ≤1

5.1.2 Numerical Solutions

One way to solve the above mentioned equations numerically is to approximate all derivatives by finite differences. (5-4) and (5-8) are discretized in space and time by explicit first forward-Euler difference scheme as (5-9)

$$\eta_i(x,t+\Delta t)=\eta_i(x,t)+\frac{\partial \eta_i(x,t)}{\partial t}\Delta t \quad \text{and} \quad \rho_i(x,t+\Delta t)=\rho_i(x,t)+\frac{\partial \rho_i(x,t)}{\partial t}\Delta t \tag{5-9}$$

The domain is partition using a mesh of i and j, both in space and time. A uniform partition in i and j is assumed so the difference between two consecutive space is dx where dx=dy and between two consecutive time points is dt. Using second central derivative scheme[132] as (5-10), the gradient energy term in (5-1) is discretized. The Laplacian term, ∇ in (5-3) can be approximated by using central first derivative as in (5-11). Figure 5-5 is the schematic Cartesian representation for (5-10) and (5-11).

$$\left|\nabla^2 f\right|=\frac{f_{i+1,j}+f_{i-1,j}+f_{i,j+1}+f_{i,j-1}-4f_{i,j}}{dx^2} \tag{5-10}$$

$$\nabla=\frac{\left[(i+1,j)-(i-1,j)\right]+\left[(i,j+1)-(i,j-1)\right]}{2dx} \tag{5-11}$$

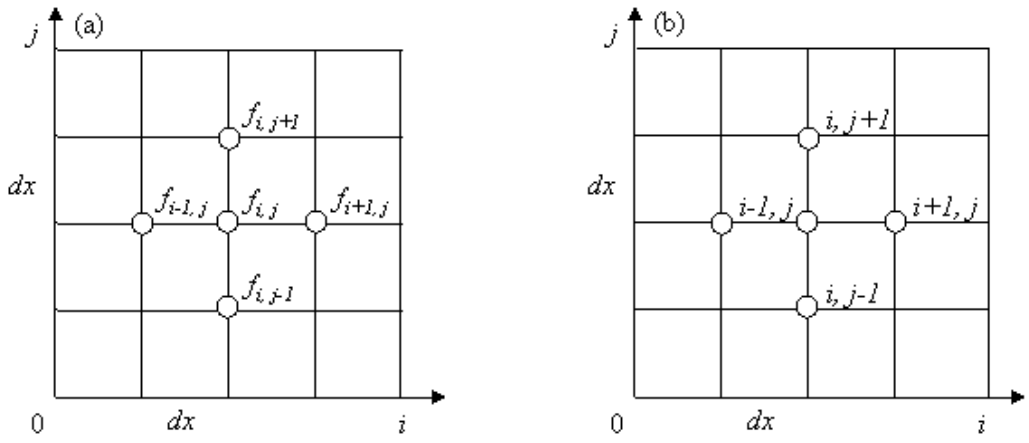

Figure 5-5 Numerical solution for (a) gradient energy term using second central derivative and (b) Laplacian term is approximated by central first derivative scheme

Solving all the equations at every grid point is very time consuming, especially when simulating a large powder system. Advanced numerical approaches

such as semi-implicit Fourier Spectral method and adaptive-grid finite-element method are reported to save computational tine and improve numerical accuracy[127]. To simplify, the simulation was written with an algorithm called "Active Parameter Tracking (APT)" developed by Vedantam and Patnaik[133], as shown in Appendices A1. At every grid point, not all phase field variables were contributing to microstructure evolution. A new set of active parameter was created by omitting the non contributing variables. This allowed unlimited number of phase field variables in the simulation with drastic reduction on computational time and memory requirement.

5.2 Validation of Phase Field Simulation for Solid-State Sintering

The microstructure evolution during sintering was simulated using the phase field model in Appendices A1, with the length scale, dx=dy=1 and time scale, dt=0.01. Small time step is preferred to maintain the stability during simulation. The time step, t* is linearly proportional to real sintering time. The reduced parameters used in the simulation are optimized from Wang's report[130]. A*=18, B*=0.45, L*=10, Bη*=1, Bρ*=10. Diffusion coefficient, D includes surface diffusion (D_s=0.4), grain boundary diffusion (D_{gb}=0.04), volume diffusion (D_{vol}=0.001) and vapor diffusion (D_v=0.0001). These diffusion coefficients provide a diffusivity ratio of about 1000:100:10:1 for Ds: Dgb: Dvol: Dv. The simulated microstructure can be obtained by plotting the order parameter, η using Matlab software. A three-particle model and a system with 16 ideally packed particles, in a domain of 128x128 were used to validate if the written algorithm can simulate solid-state sintering.

5.2.1 Sintering of Three Particles

The three particles sintering model is a classic model to study the solid-state sintering. The microstructure evolution is shown in Figure 5-6. At t*=0. the three particles are circular in shape and of the same size, touching each other to form a pore in the center. The pore edges are completely concave as the three particles touching one another. As sintering proceeds, neck grows at the contact point into grain boundary. The resulting grain boundary is smooth and straight, to achieve energy minimization by reducing the grain boundary curvature according (1-1). Shrinkage and densification are observed with the center of mass of the three particles approaching one another. Concave curvature of the pore becomes increasingly convex during pore shrinkage, as the classic pore evolution shown in Figure 1-4. At t*=900, the pore shrinks and disappears, forming a new grain triple junction. Further sintering after pore closure results in the round up of the grain outer surface to continue lowering the total free surface energy. Simulated microstructure evolution of the three particles was consistent with kinetic Monte Carlo simulation[134] and Brakke's Surface Evolver program[135], suggesting the feasibility of the written phase field algorithm in simulating solid-state sintering.

5.2.2 Sintering of Ideal Packed Structure

The microstructure evolution of the ideally packed system is demonstrated in Figure 5-7. This system is an accumulation of several three particle model at t*=0. As densification progress, many new grain triple junctions formed. Unlike three-particle

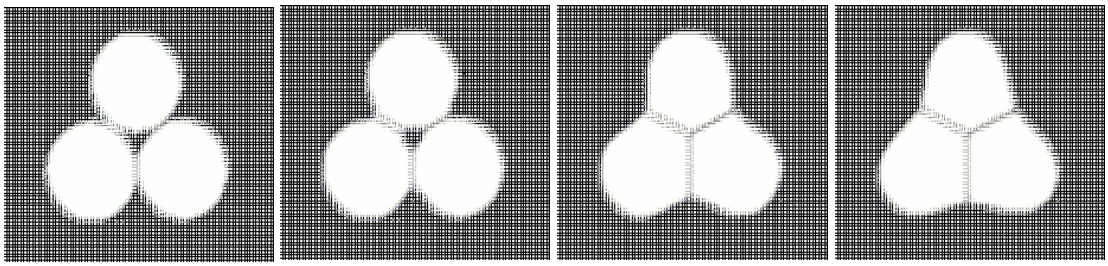

(a) t*=0 (b) t*=20 (c) t*=900 (d) t*=2400

Figure 5-6 Simulated three particles sintering (a) three touching particles (b) neck growth and pore round up (c) disappearance of pore (d) round up of grain surface

model, each the grain at the center has 6 neighbors. When t*=7000, four stable hexagonal grain structures are observed. These grain have dihedral angle of 120º, thus further sintering does not change the internal structure. However, the outer surface is not stable with the concave and convex curvature inherent from the shape of powder compact. Further sintering straightens the surface curvature, in the mean time causes the grains with concave surface grow at the expense of convex surface. The atoms transfer from the convex surface to concave surface, according to (1-1). This is observed at t*=14200, the four inner grains remain in stable hexagonal structure, while the outer grains evolved to different sizes. As the system continues evolving to minimize the total free energy, in infinite time, the coarse grains may grow at the expense of the finer grain and eventually become one coarse grain. With more than three particles, the written phase field algorithm is able to simulate suppressed grain growth for hexagonal shaped grain and the grain growth driven by curvature migration.

The diffusional activities in such a system are highlighted to ensure the

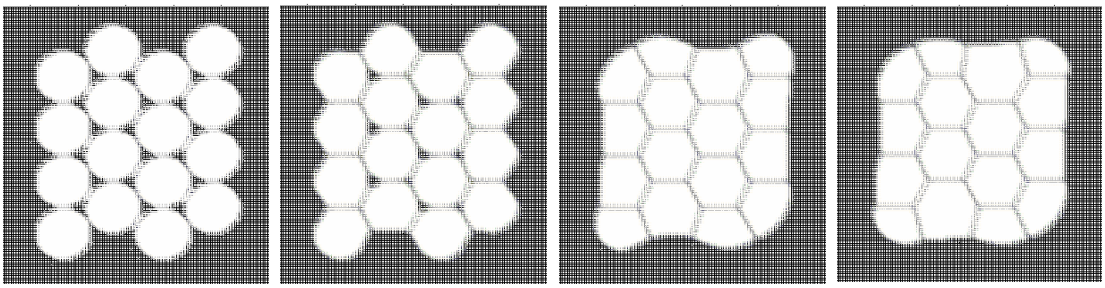

(a) t*=0 (b) t*=100 (c) t*=7000 (d) t*=14200

Figure 5-7 Simulated morphology evolution for ideal packed system shows overall densification without increase in the average grain size

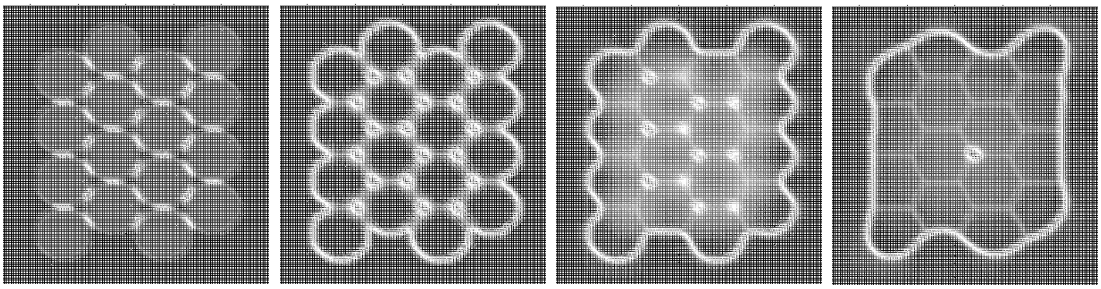

(a) t*=0 (b) t*=6 (c) t*=100 (d) t*=6000

Figure 5-8 The distribution of diffusional activities at t*=0, 6, 100 and 6000, of an ideally packed system, the brighter color corresponds to higher diffusional activity, ∑D

diffusivity coefficients ratio is appropriate. Figure 5-8 compares the diffusional activities, ∑D at different simulation time. Even though the diffusivity coefficients ratio is 1000:100:10:1 for diffusion in surface: grain boundary: volume: vapor (Ds: Dgb: Dvol: Dv), the diffusion at outer surface is not the most active initially. When t*=0, diffusion only occur at contact points, with ∑D less than $16x10^{-3}$. At t*=6, sintering is governed by densification where pore area has the highest diffusion with a combination of surface diffusion, grain boundary diffusion and vapor diffusion. ∑D is about 0.1 at pore area, and about 0.03 at grain boundary. Vigorous diffusional activity

also occurs at surface with sharp angle to increase the dihedral angle towards 180˚. As the pores shrink and close with time, surface diffusion becomes dominant with secondary diffusion activity at grain boundaries, as shown in figure (d). Such a diffusional activities ratio has shown advantage in simplifying the complicated sintering process and successfully simulates all stages of sintering, from a porous powder compact, to a densified structure without any remaining porosity.

5.3 Random Packed Structure

Two-dimensional simulation was performed on a coarse and a fine random packed structure. The random structures were generated using Material Studio Software while the random orientations were generated using a random number generator program as in Appendices A2. The data was transform into a domain of 256x256 grids using program in Appendices A3 and A4. The diameter of coarse one is about four times larger than the fine one. This provides a phenomenological study on microstructure evolution, typically for the NANO and BASF, to understand whether the growth behavior of nanosized powder deviates from classic curvature migration.

5.3.1 Microstructure Evolution for Coarse Powder

To mimic the experiment finding, a more realistic random packed structure is used. Figure 5-9 shows the microstructure evolution of a coarse random packed

powder system with the initial size distribution is monotonic. Besides growth in average grain size, pore elimination and surface round up are consistent with ideal packed structure. The morphological evolution is in agreement with prior work[130]. Disappearance of three-sided grain and neighbor switching, are observed during simulation as circled in figure (c), (d) and (e), respectively. Generally disappearance of three-sided grain refers to as T2 and the neighbor switching is named T1 process[135]. These process are commonly observed in sintering, are also predicted in three-dimensional Monte Carlo simulation[123]. Given enough simulation time, grain growth in term of increase in average grain size is observed. The average grain size,

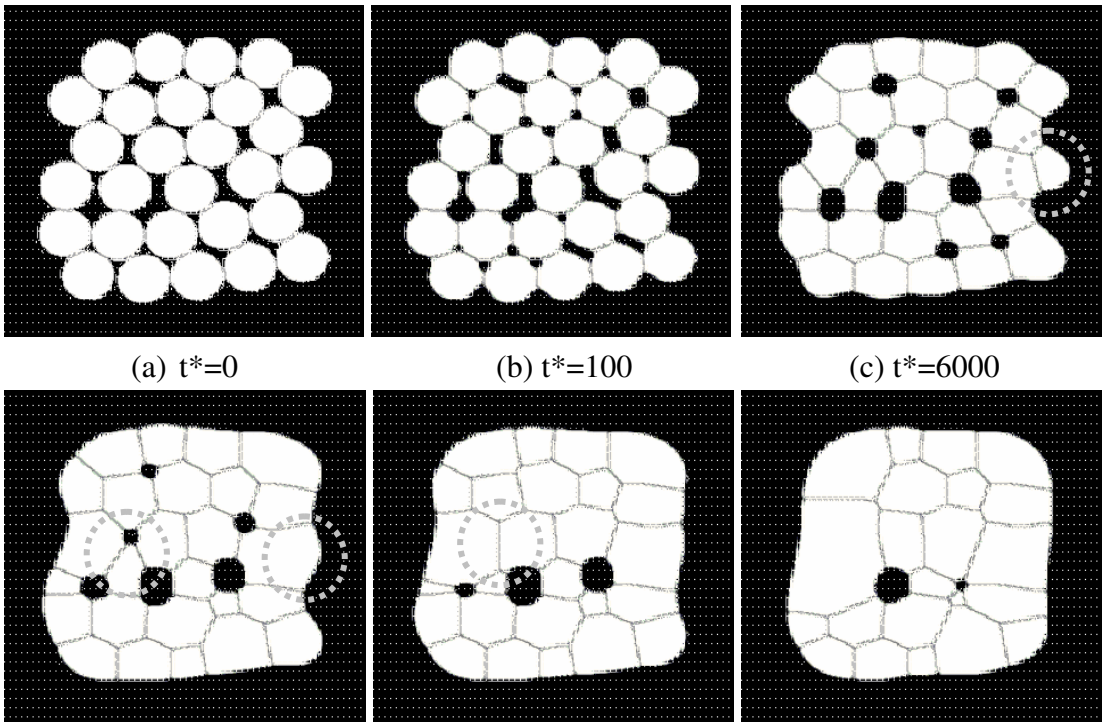

(a) t*=0 (b) t*=100 (c) t*=6000

(d) t*=40000 (e) t*=80000 (f) t*=220000

Figure 5-9 Simulated microstructure evolution of monosized random packed structure, the average grain growth is 1.3 time of initial powder size, is in consistent with experiment result of BASF.

refer to the total area per total number of grain, is 1122 unit^2 initially, as some of the grain disappeared after being consumed by the coarse grains, the average grain size increase to about 1492 unit^2 at t*=220000. The relative growth thus is 1.3 times of the initial powder size, and the biggest grain grows more than four times from initial size. The simulate grain growth based on the average grain size however, is slower than experimental observation. This is explicable with the difference in initial size and shape. The wide size distribution and irregularity in shape of BASF (as shown in Figure 3-5) may stimulated grain growth, whereas monosize and spherical shape used in simulation may slowed down grain growth. Besides the slower grain growth rate, simulated morphological evolution is generally consistent with the experiment result of coarse BASF in Figure 4-11. This implies that the written algorithm based on classic grain growth via curvature migration is accountable for coarse grain structure, not only in ideally packed structure, but can be extended to random packed structure.

5.3.2 Microstructure Evolution for Fine Powder

Experimental results in Section 4.2 revealed extensive grain growth during initial sintering stage for nanosized powder; even the initial size distribution is almost monotonic. To verify if the nanosize caused this extensive grain growth in initial sintering stage, microstructure evolution of monosized fine powder was simulated. Figure 5-10 shows the evolution of fine powders that are about four times smaller than those in Figure 5-9. In contrast to the experimentally observed extensive initial grain growth, the simulation result shows a suppressed grain growth initially. Due to

the monosized distribution, no significant grain growth is observed before t*=10. The suppressed grain growth is similar to simulation result in Section 5.2, suggesting that the monosized distribution is able to inhibit grain growth. Considering classic grain growth via curvature migration as (1-1), powders of same size have the same curvature, thus grain growth is not expected in monosized powder system.

Rapid growth occurs after t*=20, some grains, typically those found around a loose packing region, have gained extra energy during simulation and start to grow by consuming the neighbor grains. It is known that differences in bulk pressure, vacancy concentration and vapor pressure drive the mass transport. Bulk pressure depends on specific surface energy to the neck radius, while vacancy concentration and vapor pressure depends on the molar volume of vacancies[136]. Grains around loose packing region thus have higher driving force than those in stable hexagonal grain array. Considering the diffusion paths, grains near vacancies not only gain mass through grain boundary and volume diffusion, but also surface and vapor diffusion. These suggest that homogenous packing is important to prevent exaggerated grain growth.

Figure 5-10 (d) shows the microstructure when t*=100. Average grain size is 203 unit^2, which is 3.9 times coarser than the starting powder size in area. However, the biggest grain found at this stage is 4272 unit^2, which has grown 81 times from the starting powder. On the other hand, several clusters of grains appeared to be insusceptible to grain growth. They remain stable hexagonal shape after densification. The mixture of such distinctive coarse and fine grain regions is not observed experimentally. Experiment result (Figure 4-5 (b)) shows a homogenous mixture between coarse and fine grains. As sintering proceed, those coarse grains continue to

grow by consuming their neighbors, and eventually all fine grains disappeared when t*=600. The microstructure at this stage resembles the experimental result. Nevertheless, the average grain size has increased to 2391 unit^2, which is 46 times coarser than starting size. The biggest grain measures at 7954 unit^2, which has increased 153 times as compared to the initial fine powder size. The growth at the latter stage (d-f) cannot justify the experimental results. As shown in (b), the limited sites that grow locally is the cause of this exaggerated growth behavior. These grow sites consumed the neighboring fine grains until they impinged upon one another, where this limited amount of coarse grains eventually became very large in size. Referring back to the stable hexagonal structure induced from ideally packed system in Section 5.2.2, this exaggerated grain growth of nanosized powder may be inhibited if the nanosized powder is ideally packed, without imposing variation in vapor concentration. However, this is very unlikely to be achieving in real system, where powder are packed randomly. It is known that in a random system, the frequency of achieving ideally packing, or having 12 neighbors is very low. Even idealized random dense monosized spheres exhibited a distribution in coordination number spanning from 5 to 11 neighbors[137]. For this reason, the exaggerated growth of nanosized powder seems unavoidable in real system.

The simulation result for coarse counterpart is found in strong agreement with BASF, even though the simulation result of random packed fine powder system does not show the extensive initial grain growth that observed in NANO, the suppressed initial grain growth and the exaggerated grain growth at a later stage is explicable with current understanding in sintering. The inconsistency with fine powder

speculates that the growth mechanism for nanosized powder differs from conventional coarse powder. In other words, the classic sintering model that is developed from coarse powder may not be applicable to nanosized powder. Many has acknowledged that sintering of nanosized powder may be governed by other sintering mechanisms like dislocation motion, grain rotation, grain boundary slip and viscous flow, at least in the initial sintering stage[59]. With the trace of irregular shaped grains that speculated

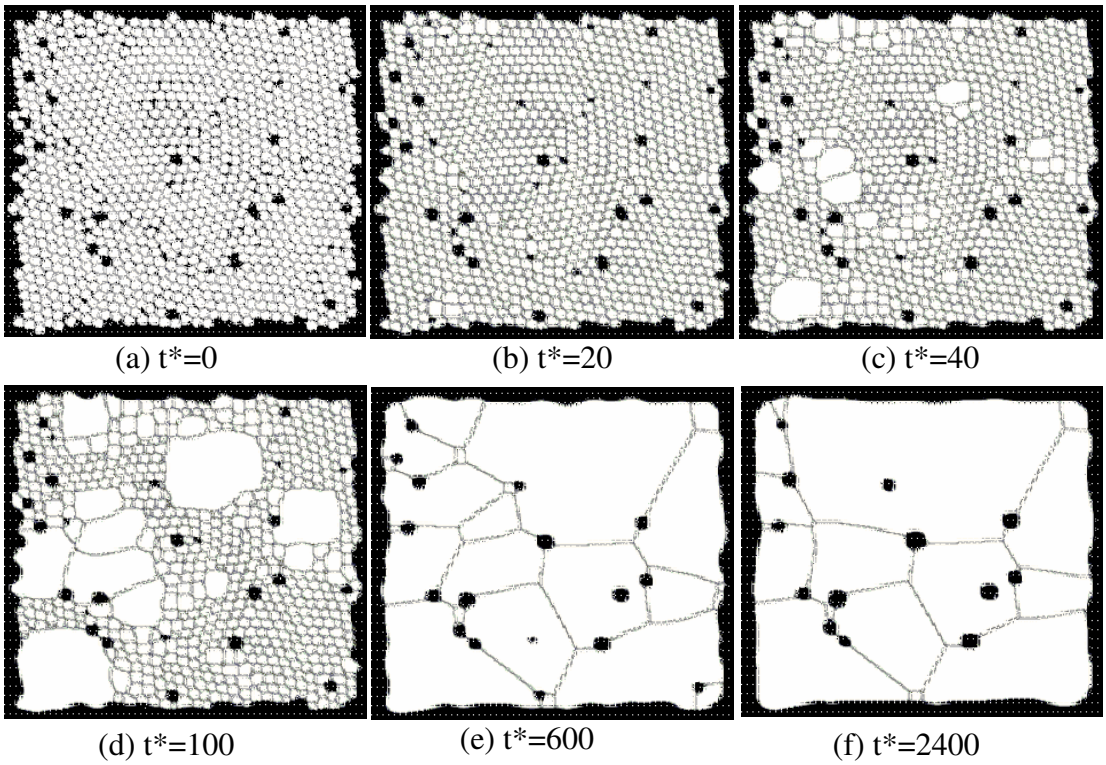

Figure 5-10 Simulated microstructure evolution of random packed fine powder, although the fine powder grows extensively as compared to coarse counterpart and the initial suppressed grain growth and the exaggerated grain growth at a later stage are explicable with current understanding in sintering, this growing behavior however is inconsistent with empirical result in Figure 4-9. This suggests that the nanosized powder grow differently from curvature migration and other grain growth mechanism, such as grain coalescence may be responsible for the observed extensive initial grain growth.

to be the evidence of grain coalescence, grain rotation induced grain coalescence is believed to play the dominant role for the extensive growth at initial sintering stage.

5.4 Summary

Solid-state sintering was modeled in this chapter using the phase field approach. The phase field algorithm was validated by three particles system and ideal packed system. It was subsequently applied to two random packed structures; the coarse structure has the size four times larger than the fine one, to mimic the experimental BASF and NANO powder. The coarse system again showed strong agreement with the sintering theory and experimental results. However, the fine system showed initial suppressed grain growth followed by an exaggerated grain growth morphology that deviates from experiment observations. The different sintering behavior of nanosized powder from coarse counterpart and simulation result was hypothesized governing by other sintering mechanisms like grain coalescence.

CHAPTER 6 GRAIN COALESCENCE DOMINATED SOLID-STATE SINTERING MODEL FOR NANOSIZED POWDER

The inconsistency of phase field simulated fine random packed powder system with experimental finding suggested that the reduction in powder size may cause the switch of dominant factors that control the sintering process from conventional coarse powder. The experimentally observed irregular shaped grains speculated that grain coalescence could possibly contribute to the extensive grain growth during initial sintering stage of nanosized powder. The adjacent grains with same crystallographic orientation would eliminate the common boundary, leading to instantaneous grain growth. The mismatch of crystallographic orientations acts as the driving force for the rotation of fine grains into a lower misorientation. A grain coalescence dominated solid-state sintering model will be proposed in this chapter.

6.1 Background of Grain Coalescence

6.1.1 Condition for Grain Coalescence

According to curvature migration theory in equation 1-1, grain growth is a form of energy minimization by reducing the total grain boundary area. Several numerical models have proven the capability of grain rotation driven by the urge to

minimize interfacial energy arising from grain orientation mismatch, according to (1-2)[65, 69-71, 76, 138-147]. Figure 6-1 shows the typical grain boundary energies as a function of misorientations. The several energy cusps correspond to Coincidence Site Lattice, CSLs, which vary with materials. The steep energy decrease from low angle misorientation to zero energy barriers for zero mismatch, on the other hand, is generally applied. For completely disordered boundary, the reported grain boundary energy is as high as 900 mJm^2, whereas for CSLs, the energy range from 300-700 mJm^2 [148]. Low angle boundaries are referring to those less than 15 °. As observed in Figure 6-1, in order to further reduce the total system free energy, low angle grains may rotate towards matching perfectly with the neighbor. This drastic reduction in grain boundary energy of low angle grains may drive the rotation of low angle grains to grain coalescence. This project only concerns the low angle grain that tends to rotate towards grain coalescence, rotation towards other CSLs, although is possible, is beyond the scope of this project.

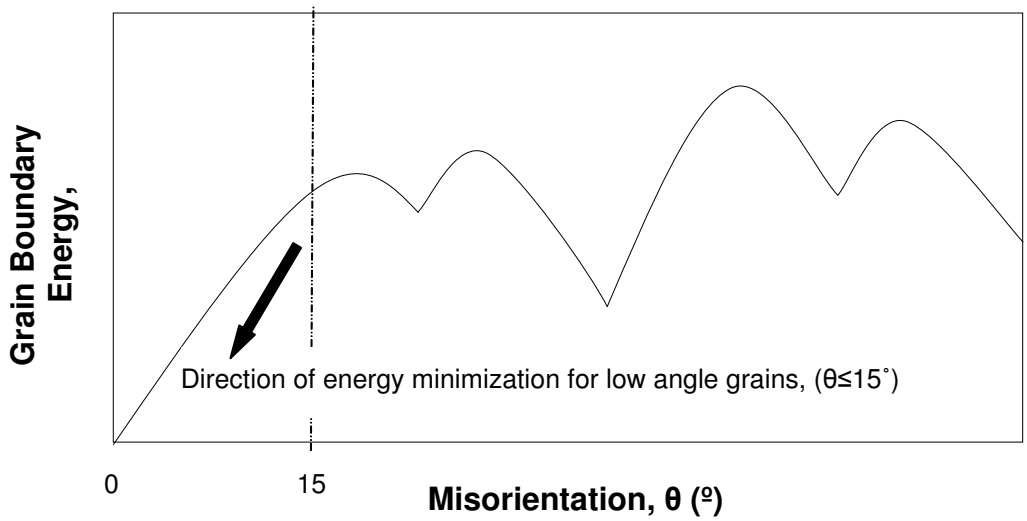

Figure 6-1 Grain boundary energy as a function of misorientation, for energy minimization, low angle grains (≤15°) rotate towards zero-mismatch

On the other hand, grain rotation may be restricted by forces such as inter particle friction, Van de Waals and electrostatic. As rotation is expected to occur during sintering, sintering force is assumed as the dominant restriction force, and influence from other forces is assumed negligible. Considering the three-particle model in Section 5.2.1, the microstructure evolution can be explained as a resultant of sintering force. Sintering force was first defined by Gregg and Rhines[149]. Shrinkage, or the motion of mass center towards one another, is a response to the sintering force acting between the particles. For equilibrium states, the external force just stops the sintering contraction along one axis of the sinter body. For a non-equilibrium sintering process, the sintering force can be expressed as a sum of the pressure acting through the grain boundary area and the surface tension acting between two particles[150]. Figure 6-2(a) shows the elements of sintering force in two particles model. The sintering force vector is defined as (6-1)

$$F = \gamma_s \bar{\kappa} A_{gb} e + \int_C \gamma_s \cos(n \times t) ds \tag{6-1}$$

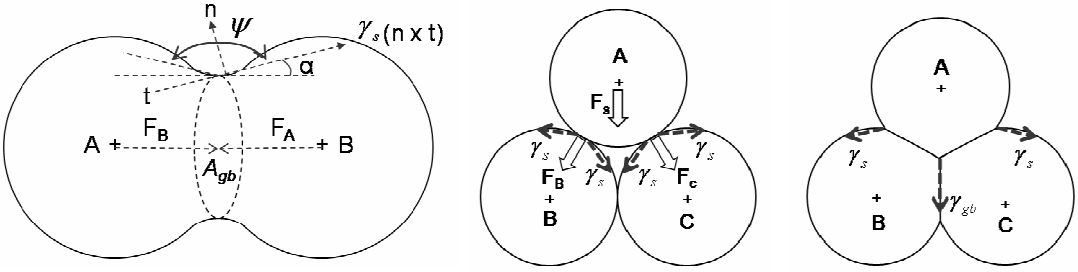

(a) sintering force elements (b) initial sintering stage (c) final sintering stage

Figure 6-2 (a) the elements for sintering force shown in a geometry of two-particle and sintering force acting on three particles model for (b) initial sintering stage (c) final sintering stage.

γ_s is the surface energy, $\bar{\kappa}$ is the average of surface curvature, A_{gb} is the grain boundary area, *e* is the unit normal vector to the grain boundary, *n* the unit normal vector to the surface, and *t* is the unit tangential vector along the surface triple junction *C*. The first term in (6-1) is induced from the average normal stress, or pressure $\gamma_s\bar{\kappa}$, in the interior of the particle immediately adjacent to the surface. The second term integrates the surface tension along the periphery of the neck[135]. The axial component of the sintering force vector can be expressed as (6-2)

$$F = \gamma_s \bar{\kappa} A_{gb} + \int_C \gamma_s \cos\alpha ds \tag{6-2}$$

where α is the angle between the tangent of the surface and the unit normal to the grain boundary. The sintering force on a particle is the total forces acting through grain boundaries with neighbor particles. Thus the sintering force acting on a particle increases with the number of neighbor particles, or the coordination number. During initial sintering stage, with pore present in the middle of three particles, as shown in Figure 6-2 (b), the net sintering force, F_s acting on particle A, pulls particle A to the pore center, where $F_s=F_B+F_C$. F_B and F_C are calculated by (6-1).

The sintering force is attractive and cause shrinkage between particles. Figure 6-2 (c) shows the center pore is eventually eliminated and the surface triple junction, *C* becomes a grain triple junction, *L*. This modifies the sintering force vector acting between particle B and C with an additional term integrates the grain boundary tension along the triple junction, *L*. The grain boundary tension, γ_{gb} is shared by B and C, thus is divided by 2. The sintering force vector, F_B or F_C thus becomes

$$F = \gamma_s \bar{\kappa} A_{gb} e + \int_C \gamma_s \cos(n \times t) ds + \frac{1}{2} \int_L \gamma_{gb} (n \times t) ds \qquad (6\text{-}3)$$

For grain or particle rotation to occur, the sintering force has to be small. Compared both (6-1) and (6-3) for a three particle model, the force from surface tension is reduced with the loss of two surface triple junctions, C; replaced by the force from grain boundary tension with the formation of a new grain triple junction, L. Grain rotation is restricted by the sintering force in (6-1), for initial sintering stage, or (6-3) for final sintering stage. The improvement in material strength in final sintering stage implies that the sintering force in (6-3) is greater than (6-1). Therefore, rotation is likely to occur during initial sintering stage with smaller restriction force. Refers to (6-2), grain/particle rotation is likely to occur at the very beginning of initial sintering stage, when α is near 90º, thus, the second term is negligible, result in a weak restriction force for grain/particle rotation. This is consistent with previous finding which highlighted the importance of grain coalescence for nanocrystalline materials, at least during early stages of grain growth[72]. Figure 6-3 shows the driving and restriction force for grain rotation/coalescence for a three-particle model. This weak restriction force can be expressed as a friction torque that counteract the cumulative torque at an opposite direction, arise from sintering force and the radius of particle, *R*, as (6-4). The friction is due to the sintering force exerted between the particles surface, as (6-5) where μ is a coefficient of friction, which is an empirical property of the contacting materials.

$$\tau_{F_f} = \sum F_f xR \tag{6-4}$$

$$F_f = \mu\left[\gamma_s \bar{\kappa} A_{gb} e + \int_C \gamma_s \cos(n \times t) ds\right] \tag{6-5}$$

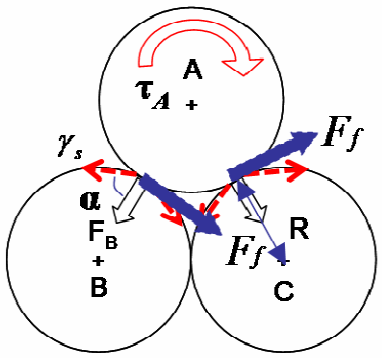

Figure 6-3 The cumulative rotation torque, τ_A drives the rotation while the friction torque, $\sum F_f R$, resultant from the sintering force, restricts such rotation

6.1.2 Misorientation Threshold

Numerical solution on rotation torque and sintering force for each particle may be computational unrealistic. Even for a three particle model, the rotation torque and sintering forces can be very complicated, with the different interfacial energies depending on the orientations and the sintering forces depending on the dihedral angles. With the assumption that the sintering force at the very beginning of the initial sintering stage is negligible, grain rotation for a more realistic random system can be simplified by considering only the probability of grain coalescence. Those adjacent particles with low angle grain boundary will be assumed to have same orientation in the input data, thus coalesced during initial phase field simulation, instead of solving

both equations (1-2) and (6-4) numerically.

To explore the possibility of grain coalescence, a misorientation threshold, θ* is introduced. Empirical evidences suggested that sintering is a complicated process depending on factors such as time, temperature, density, particle size, grain size and external pressure[20, 33]. θ* is thus proposed to be proportional to the sintering temperature, T and sintering duration, t, and the spherical factor, S; inversely correlated to initial particle size, d_o, green density, ρ, and sintering pressure, P; as proposed in (6-6)

$$\theta^* \propto \frac{TtS}{d_o \rho P} \tag{6-6}$$

The major factor is the initial particle size, d_o. Smaller particles are kinetically favorable for grain rotation with their lighter mass. This dramatically increases the mobility and reactivity of the particle. Based on phase field and molecular dynamic simulation, Upmanyu et al.[76] predicted the rotation rate to be roughly proportional to R^{-2} (radius of particle, $R = d_o/2$). The shape factor relates to the sphericity of a particle, S=1 for sphere that facilitate rotation and 1<S<0 for irregular shape that inhibit rotation. Pressure, P, corresponds to the external pressure applied during sintering that suppresses the particles mobility. Green density, ρ, explains the initial packing condition. Low green density or loose packing is subjected to rearrangement during sintering, as evident by the greater shrinkage. This encourages the grain rotation and thus, increases the chances of grain coalescence.

The sintering temperature, T, affects the sintering significantly and often

appears in an exponential term[20]. The sintering duration, t, has a relatively minor effect compared to other factors. Longer sintering duration increases the possibility for any adjacent fine grains to rotate into the zero-mismatch. Grain growth however is inevitable with high temperature and long duration sintering. When grains grow greater than the critical size with the increase sintering temperature and duration, grain rotation is inhibited and grain coalescence is no longer significant[70]. On the other hand, when the grain size is smaller than critical size, the increase in sintering temperature and duration allows the fine grain to rotate at higher degree overcoming greater misorientation barrier, thus increase the significance of grain coalescence. Relationship of θ^* with the governing factors is true for fine grain smaller than critical size, likely at the very beginning of initial sintering stage, which is consistent with the weak sintering force in early sintering that promotes grain rotation/coalescence. To determine the exact correlation of θ^* with the governing factors however requires further experimental works and may vary with materials.

6.2 Proposed Grain Coalescence Model for Nanosized Powder

Figure 6-4 shows the schematic drawing that represents the proposed morphological evolution for grain coalescence dominated solid-state sintering model. The evolution begins with the random packing structure. During sintering, the system enthalpy increases with the heating process. When the supplied heat reaches the activation energy, sintering begin with neck growth at contact points. Particle rearrangement is often observed in the form of rotation and translation.

Crystallography orientation mismatch is the driving force for rotation while translation is driven by the imbalanced surface energies and inhomogeneous packing condition[20]. The relative interfacial energy is significantly different with the misorientation. The interfacial energy is zero with zero-mismatch and then rapidly increases with the low angle misorientation ($\theta \leq 15^{\circ}$)[63, 151], as shown in Figure 6-1. When the rotation torque, τ_i greater than the friction torque, τ_{F_f}, particle rotates to reduce the system free energy. As a consequence, low angle grain/particle rotates to zero mismatch and rearrange for a higher packing density. Figure 6-4 (d) shows one possible preferred low energy state where some low angle grains/particles rotate to same orientations. Particle rearrangement only requires overcoming weak sintering forces and low interfacial energy at zero misorientation. The elimination of common boundaries is almost instantaneous thus grain coalescence can occur at pretty low temperature. This is consistent with previous works that reported the reduced activation energy for grain growth in nanosized powder[8, 93]. Sintering is highly complex and all possible sintering mechanisms competing among each other to lower the system free energy. Microstructure evolution that observed during sintering process is a result of free energy minimization. Grain coalescence induced by rotation of low angles grain achieves the purpose of free energy minimization as curvature migration. The grain size increases with the reduction in the number of grains and the total area of grain boundary. As rotation rate is reported to increase with decreasing grain size[76], grain coalescence may be significant for nanosized powder and cause the extensive grain growth during initial sintering stage. Therefore, under preferred condition, like sintering of nanosized powder, grain coalescence may dominate the

sintering mechanism, over curvature migration.

Grain coalescence widens the size distribution as observed experimentally in Figure 4-5 (b). After coalescence, curvature migration becomes dominant again. Variation in size and irregular shape promotes grain growth at the expense of finer grains. The remaining nanosized grains have high surface energy. Surface diffusion involves the random movement of atoms from the particle surface to other favorable sites. Evaporation-Condensation, E-C transport also plays an important role. E-C involves reposition of surface atoms to other preferable sites, similar to surface diffusion, but across pores space instead of grain boundary[20]. With sharp dihedral angle, the contact point of the coalesced grains, pointed by the arrows in Figure 6-4 (f) serves as suitable sites for atom reattachment. The remaining non-coalesced nanosized grains will be consumed by the neck via surface transport and E-C. The atomic diffusion contributes to the curvature migration to smoothen the irregular shape grain boundary induced by grain coalescence (Figure 6-4 (g)). This process stimulates the grain growth after grain coalescence, further exaggerates the grain growth after grain coalescence. Exaggerated curvature migration occurs within a short period of sintering process, due to the irregularity of coalesced grains, is in qualitative agreement with experiment observation. Figure 6-4 (h) shows the resultant microstructure after grain coalescence and exaggerated curvature migration induced from grain coalescence. Further sintering from here may eliminate all remaining porosity and further grain growth to lower the total free energy. However the grain growth rate is expected to be slow if compared to what induced by grain coalescence.

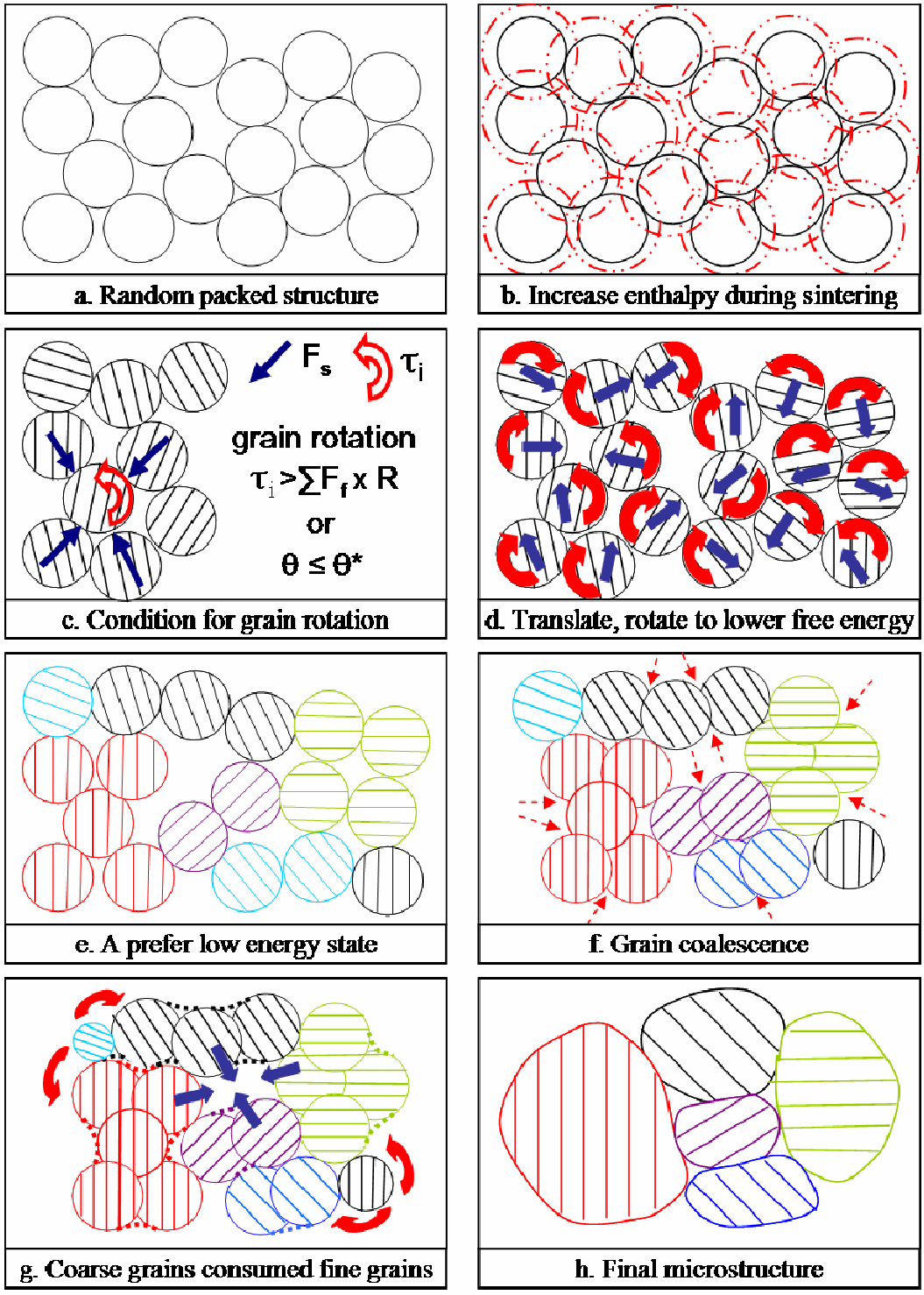

Figure 6-4 Schematic representation of the proposed grain coalescence dominated solid-state sintering model, morphological evolution of the proposed model differed from the classic curvature migration during the initial sintering stage when grain coalescence takes place and modifies the size and shape of the monosized powder.

6.3 Summary

For the first time, grain coalescence dominated solid-state sintering model, highlighting the significance of grain coalescence, due to fine grain/particle rotation, in addition to the classic grain growth driven by curvature migration, is proposed. To validate the proposed model, probability study on grain coalescence and its influence on microstructure evolution are required.

CHAPTER 7 QUANTITATIVE ANALYSIS FOR GRAIN COALESCENCE DOMINATED SOLID-STATE SINTERING MODEL

Numerical models and empirical findings demonstrated the elimination of low angle boundaries (≤15º) through rigid body rotation and grain coalescence to further reduce the system energy. Grain coalescence dominated solid-state sintering model was proposed in previous chapter. To quantify the potential of grain coalescence in solid-state sintering, a three dimensional structure highlighting the orientation of vicinity neighbors is modeled.

7.1 Quantitative Simulation Set-up

Figure 7-1 shows a box of 997 randomly packed particles generated using Material Studio Software, with the arrows indicate the random orientations. For 3-D condition, three random orientations were generated using a Random Number Generator as in Appendices A2, referred to rotation of the crystal structure at x, y and z direction. Referring to Figure 7-2 (a), contacting neighbors are those with their centre points within the 2R distance where R is the radius of the sphere. For example, D, E, H, F, N and O are contact neighbors of G. Unbalanced force during sintering drives particle rearrangement and overall dimensional shrinkage. Thus, non-contact

particles may potentially form new contacts. In the simulation, particles within the vicinity of 3R (>2R, ≤3R) are considered as non contact neighbors, which means A, B, C, H, J, K, L and M are the adjacent neighbors for I.

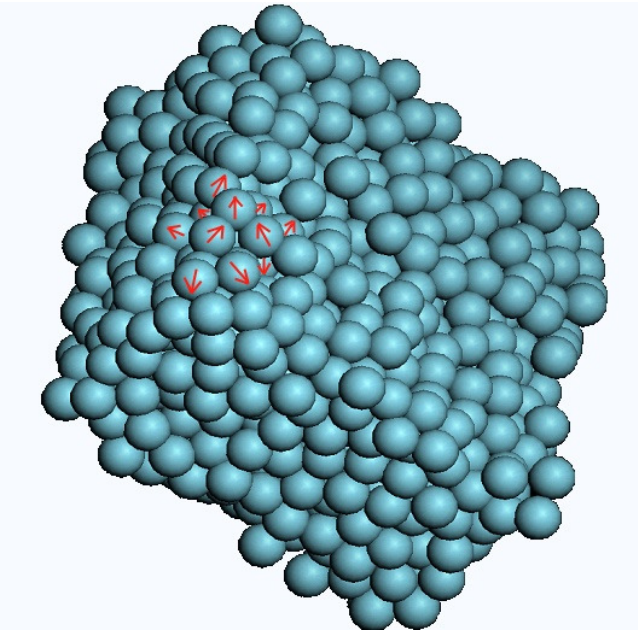

Figure 7-1 The 3-D random packed particles generated using Material Studio Software, was later assigned with random grain orientation (represent by the arrows), to mimic the real powder compact system.

Misorientation is defined by the rotation angle about the common axis. The orientation of each particle is randomly assigned to identify the misorientation angle, θ. For simplification, all spherical particles are assumed to be single crystal. The model can be applied to various materials with the random orientation generated according to respective crystal structure. For simple cubic structure, the biggest possible misorientation about common axis is 45º, for all three directions. Figure 7-2 (b) shows a tetragonal structure that is modeled for 3Y-TZP. Three random orientations were required to describe the misorientation about the common axis

XYZ. One orientation varies from 0-45º for z axis, represented by particle K in Figure 7-2b. The other two θ angles range from 0-90º, for rotation along elongated axis, x and y, denoted by particle A. For example, particles A and B, K and L have the same orientation.

A misorientation threshold, θ*, as discussed in Section 6.1.2, is used to simplify grain coalescence. For cases where θ > θ*, such as particle E and F, also C and D (Figure 7-2 (c)), grain boundaries will form during sintering. On the other hand, when θ ≤ θ*, the particles rotation will overcome the narrow misorientation, as such particles H and G, N and O coalesced (Figure 7-2 (d)). To reduce the bias, each θ* is accumulated from 10 sets of random orientation and that increases the

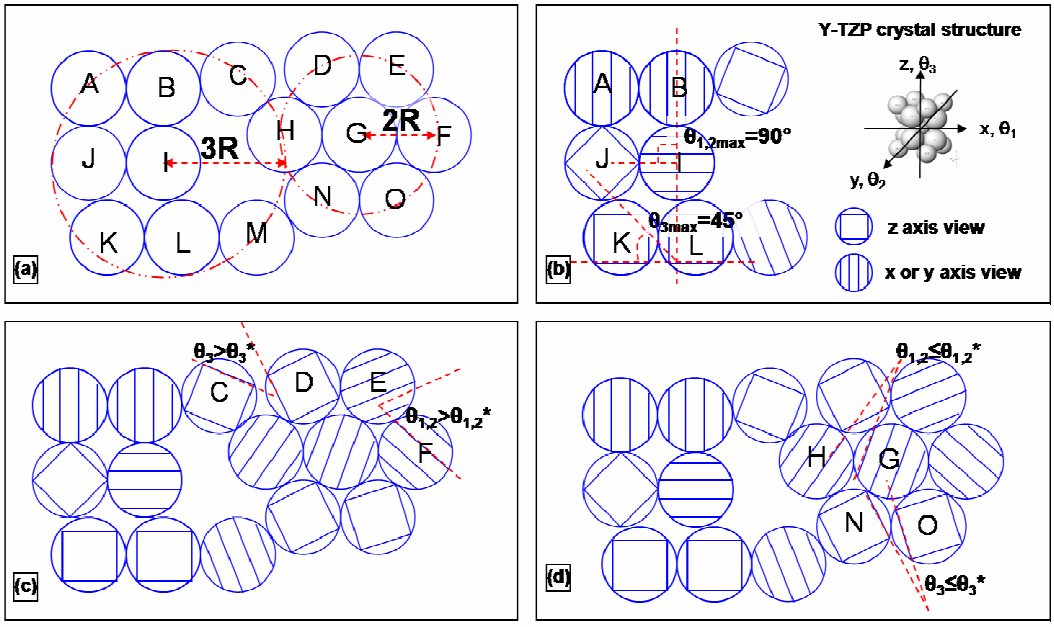

Figure 7-2 Simulation set up to identify probability of grain coalescence (a) criteria for contact and non contact neighbors, (b) maximum miorientation degree corresponding to the crystal structure, (c) criteria for grain boundary formation, θ> θ* and (d) criteria for grain coalescence, θ≤ θ*

simulation size to near 10,000 particles. When $\theta \leq \theta^*$, the grains coalesce; whereas beyond θ^*, the grain boundary formed. Higher θ^* means that the particle is more freely to rotate to overcome higher misorientation angle. Consequently, grain coalescence is more significant and results in higher grain growth.

The increase in misorientation threshold, θ^* is due to the increase of mobility which governs by the shape and size factor, sintering temperature and packing condition, as in (6-6). As the simulation is based on probability, rotation against common axis XYZ is possible. Only neighbors with all the three misorientations about the XYZ axis are less than θ^* will be identified as potential coalescence grains, which expressed in equation (7-1). The program was written in FORTRAN language as in Appendices A3, with different seeding number for Appendices A2, so to generate different sets of random orientation for to the system.

$$\left.\begin{aligned}\theta_1 - \theta_{1'}\\ \theta_2 - \theta_{2'}\\ \theta_3 - \theta_{3'}\end{aligned}\right\} \leq \theta^* \qquad (7\text{-}1)$$

7.2 Results and Discussions

7.2.1 Grain Coordination Number

Grain coordination number is the contacting neighbor that one particle has. Figure 7-3 shows the distribution of the contacting neighbors in the simulated monosized spheres. The histogram shows the highest percentage of particle has 8 neighbors, which the distribution in packing coordination is in substantial agreement

with random dense structure[137]. The Gaussian distribution curve shows an average of 7 contacts in the generated random packed system, consistent with literature where the average grain coordination number is spanning between 6-7 neighbors[20]. This implies that the simulated system mimics the empirical powder compact at a reasonably large scale without idealized columnar grains with 6 neighbors that formed only stable hexagonal grains that suppressed grain growth during simulation, as demonstrated in Figure 5-7.

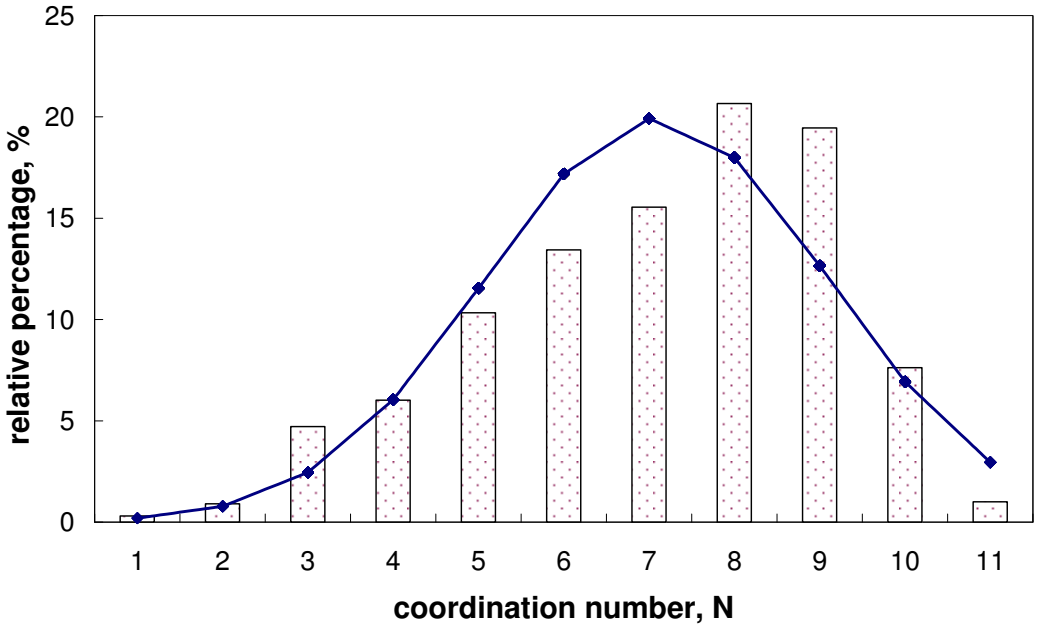

Figure 7-3 Simulated particle coordination number and the Gaussian distribution curve shows the average coordination number is 7, which is consistent with previous finding, suggesting a reasonably good input set for quantitative study.

7.2.2 Effect of Crystallographic Structure

The probability for grain coalescence can be quantified with the introduction of misorientation threshold. Figure 7-4 shows the percentage of coalescence grains as a function of misorientation threshold, θ*, for both cubic and tetragonal structure.

Grain coalescence is almost impossible in realistic case for conventional material, as the chance for adjacent grains to coincidently having zero misorientation is very rare. Often the orientation is far different and grain boundaries will form in between the particles. This is proven when both cubic and tetragonal structure show 0% coalescence grain with $\theta^* \leq 0^\circ$. Grain growth via grain coalescence depends on the number of particles that can potentially share the common orientation, generally increase with greater θ^*. The probability for $\theta \leq \theta^*$ also increase with the symmetry of crystal structures like simple cubic structure. Coalescence grains percentage for cubic structure is about 10 folds higher than tetragonal structure. Cubic structure such as Yttria often found with high grain growth probably implies the contribution of grain coalescence in grain growth.

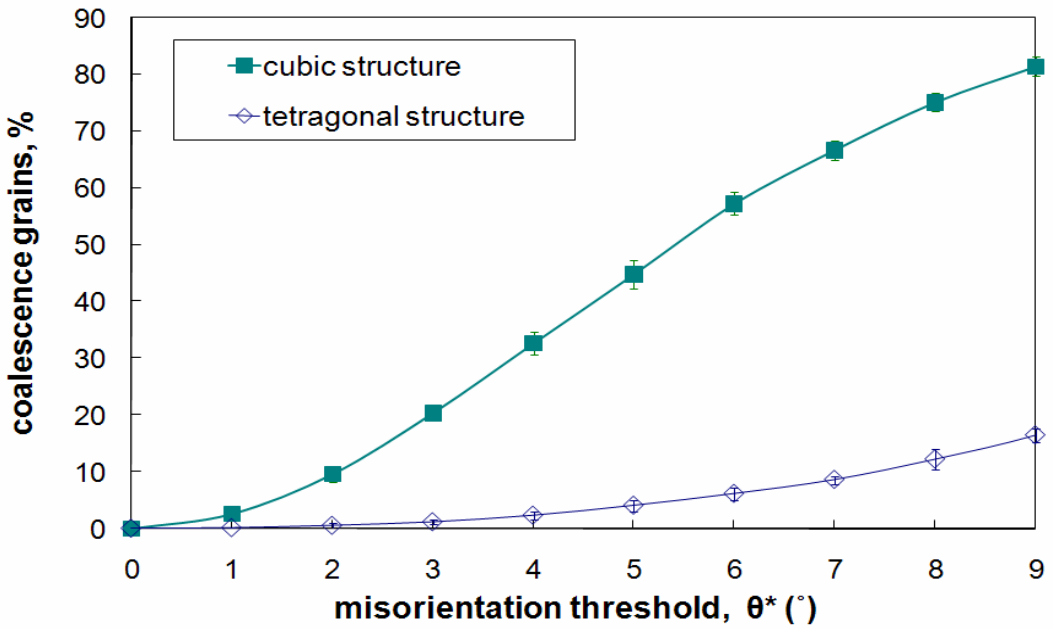

Figure 7-4 Percentage of calescence grains for tetragonal and cubic structure as a function of misorientation threshold, where simple crystal structure has higher probability for grain coalescence

7.2.3 Percentage of Coalescence and Non Coalescence Grains

Grain growth is curvature migration driven for conventional coarse powder, while grain growth may be a result of grain coalescence, especially for nanosized powder, as proposed in Chapter 5. Figure 7-5 shows a curvature migration dominant and grain coalescence dominant region with different misorientation threshold, θ*. Curvature migration is the dominant grain growth mechanism for the case θ*≤ 2˚. When θ*=0˚, the percentage of coalescence grains is zero, explains the rational of usual practice in ignoring the grain coalescence. The average percentage of total coalescence grains increases with increasing misorientation threshold, θ*. The amount of coalescence grains rise slowly with trivial fraction or less than 1% when θ* ≤ 2°. With such a small fraction of coalesced grain, curvature migration remained the dominant growth mechanism. However, this region may prone to abnormal grain growth. The amount of coalescence grain is less than 1%, which means > 99% grains remain in their initial size. The minority coalesced coarse grain may consume the surrounding fine grains and grow preferentially, like Figure 5-10 (d). With substantial sintering however, the grain size distribution will eventually approach each other and the abnormal grain may be less noticeable, as shown in Figure 5-10 (e). The coalescence grains increases significantly to 49% when θ*=15°. Grain coalescence is considered important when 3°≤θ*≤15°. The coalesced grains widen the size distribution and cause different microstructure evolution compared to non coalescence case. The coalesced coarse grains compete to grow at the expense of remaining fine grains, leading to overall coarsening at a fast pace.

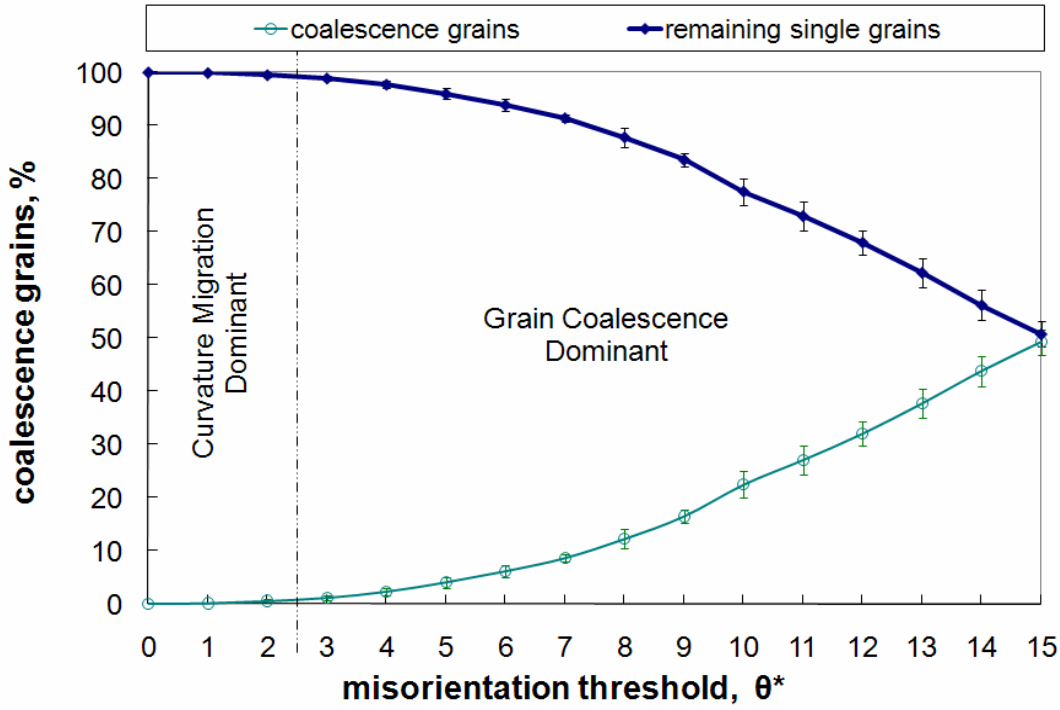

Figure 7-5 Percentage of coalescence grains as a function of misorientation threshold, θ*, for tetragonal structure. Grain growth is divided into curvature migration and grain coalescence dominant zone

7.2.4 Coalescence Size and Irregular Shaped Grains

Figure 7-6 shows the maximum coalescence size as a function of misorientation threshold, θ*. It is clear that for θ* = 0°, N=1, where all particles remain in their initial size without a coalescence neighbor. The number of coalescence grain increases with the increase of θ*. For 1° ≤ θ* ≤ 3°, the coalescence size is limited to two. When θ*≤ 3°, less than 2% particles coalesced with the size of two. Majority of the particles, more than 98% are without any coalescence neighbors. For coalescence size of two, the two particles are aligned in one line lead to slightly elongated shape. However, the size is not much different from initial size and the percentage of coalescence is very low, thus the irregularity may not be obvious. For

4°≤ θ*≤ 6°, the coalescence size is limited to three. The coalesced three particles may exist in the shape of 'C', 'L' or 'o', thus increase the irregularity. The larger the coalescence size speculates higher irregularity in coalescence shape. When θ*=15°, greatest coalescence size is 27 particles. About 50% of initial particle coalesced grains with the coalescence size span from 3 to 27. This may result in more complex shape like "Y", "X" and even corrugated shape. The greater coalescence size drastically increases the grain growth through instantaneous grain coalescence. On the other hand, the complex coalescence shape has greater driving force for grain growth via curvature migration to smoothen the irregular boundary towards straight boundary.

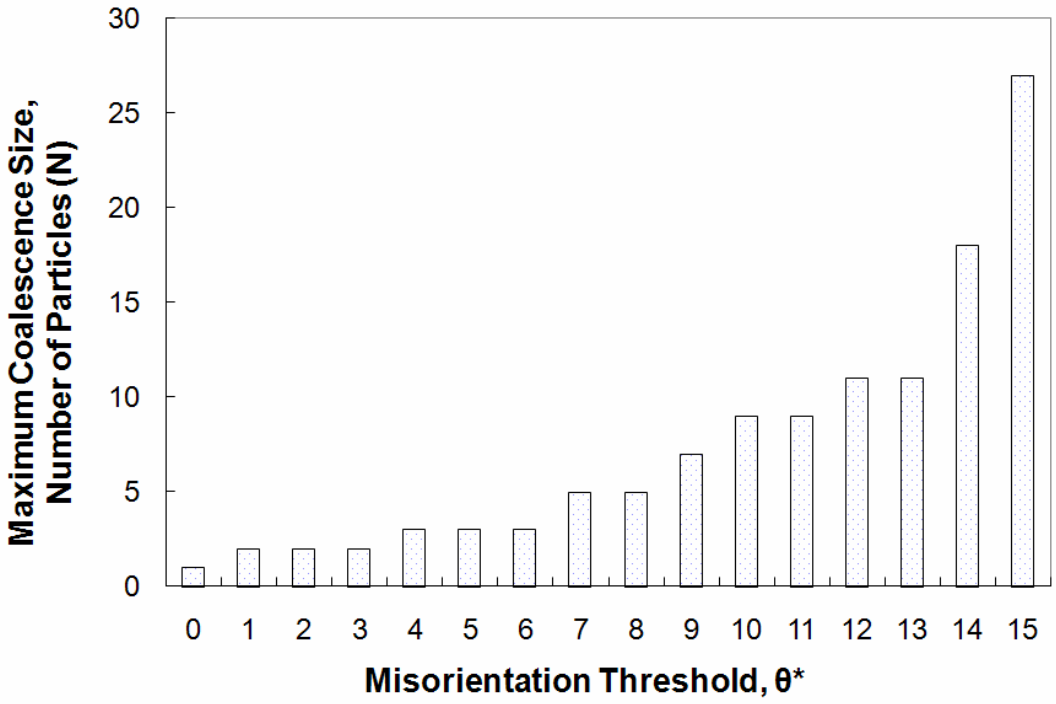

Figure 7-6 Maximum coalescence size as a function of misorientation threshold, θ*, the larger the coalescence size, the more irregular the coalescence grain shape stimulating higher grain growth via curvature migration

7.3 Summary

With the introduction of a misorientation threshold, θ*, the potential of grain coalescence was quantified. Grain coalescence increased with the symmetry of crystal structure, resulted in more significant coalescence percentage and size. Simulation results indicated about 50% of low angle grains within 15º of misorientation for tetragonal structure. The large coalescence size led to the formation of irregular shaped grain that further stimulated the initial grain growth via curvature migration. Therefore, it is important not to overlook the contribution of grain coalescence to the extensive grain growth during initial sintering stage of nanosized powder.

CHAPTER 8 QUALITATIVE ANALYSIS FOR GRAIN COALESCENCE DOMINATED SOLID-STATE SINTERING MODEL

Grain coalescence dominated solid-state sintering model was proposed in Chapter 5, and its significance was quantified in Chapter 6. It showed that the significance of grain coalescence increased with the grain rotation capability, or misorientation threshold, θ*. In this chapter, morphological evolution of grain coalescence dominated solid-state sintering model will be studied using phase field algorithm and grain coalescence probability discussed in Chapters 4 and 6.

8.1 Qualitative Simulation Set Up

In Chapter 6, probability of grain coalescence for tetragonal structure was simulated considering θ* for all three axis. This provided the probability of grain coalescence similar to the real powder compact. However, the written phase field algorithm was for 2-D microstructure evolution. A new set of input data for 2-D planar incorporating with the different grain coalescence degree or θ* was used. Reduced from 3-D to 2-D, only one random orientation, $0 \leq \theta \leq 45^{\circ}$ was generated, instead of three. The program to convert the random orientation of coalesced grains into one new orientation was as in Appendices A4. The reduced dimensionless temporal space, t* was compared with isothermal holding duration in minutes.

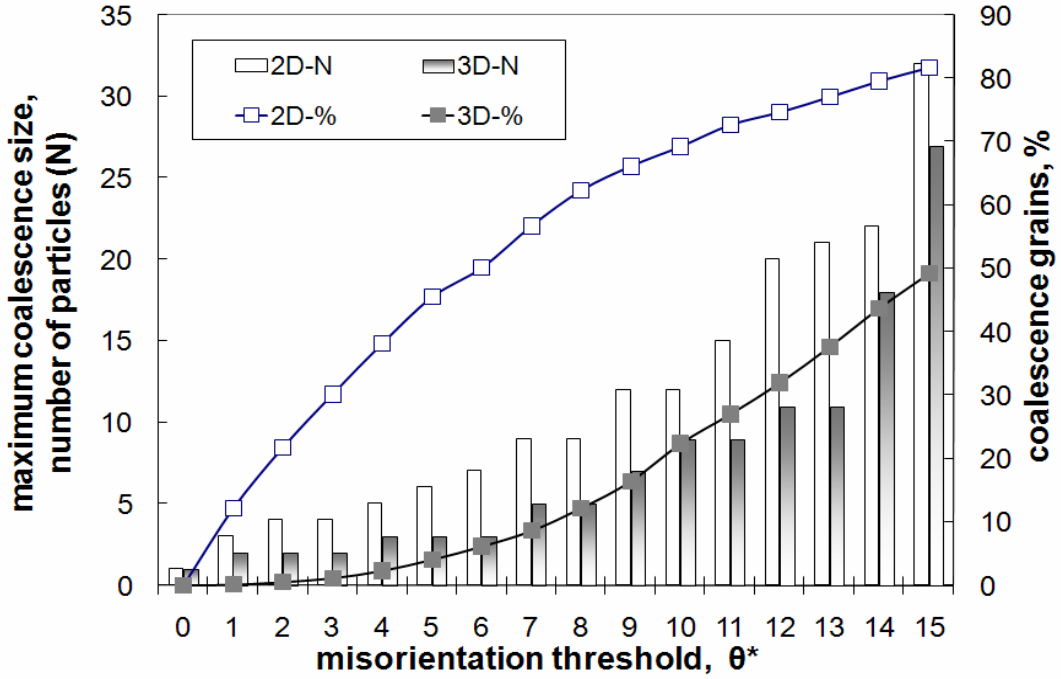

Figure 8-1 Maximum coalescence size and coalescence percentage for 2D and 3D shows the discrepancy between 2-D phase field simulation and 3-D probability analysis.

Figure 8-1 plots the maximum coalescence size and the coalescence percentage for 2-D planar simulation, compared to those for 3-D, obtained in Chapter 6. It can be seen that 2-D condition has higher maximum coalescence size and coalescence grain percentage than 3-D condition. For 3-D condition, in average, each particle has seven neighbors, while only three for 2-D condition. In view of the reduction in coordination number and random orientation when reducing simulation from 3-D to 2-D condition, discrepancy between 2-D phase field simulation and 3-D probability study is inevitable. Experimentally, the microstructure evolution is observed on 2-D cross section after grain growth three dimensionally. The coalesced clusters may have higher irregularity speculates a more drastic curvature migration to smoothen the odd shape grain boundary in all three dimensions. For 2-D phase field

simulation, even though with higher coalescence percentage and coalescence size, grain growth is occur only on 2-D planar. Without the influence from all three dimensions, the grain growth via curvature migration to straighten the grain boundary may be slow down. Moreover, the phase field algorithm was written based on a general double well potential and assumed diffusivity, which may deviates from the actual 3Y-TZP material that used experimentally. Therefore, some discrepancy of 2-D simulation from real system is unavoidable. Although 2-D phase field simulation may not directly manifest microstructure evolution of a real system, it will be able to provide phenomenological evidence, such as the effect of coalescence size and percentage, on microstructure evolution.

8.2 Results and Discussions

8.2.1 Relative Grain Growth

Isothermal grain growth can be characterized as function of average grain size versus sintering time. Figure 8-2 compares the simulated grain growth for different coalescence degree by varying the misorientation threshold (θ*), together with the experimental result of NANO. Generally, the relative average grain size, $\bar{A}/\bar{A}_0$ is increasing with simulation duration. The growth rate is rapid initially and then slows down after certain simulation time steps, t*, except for the case of θ*=0˚.For θ*=0˚, no grain growth is observed initially, follows by a rapid growth rate at t*=100. The growth then slows down and stagnant at t*=600. At t*=1100, grain growth is stimulated again and reaches a stagnant stage at t*=1300. The deviation of growth

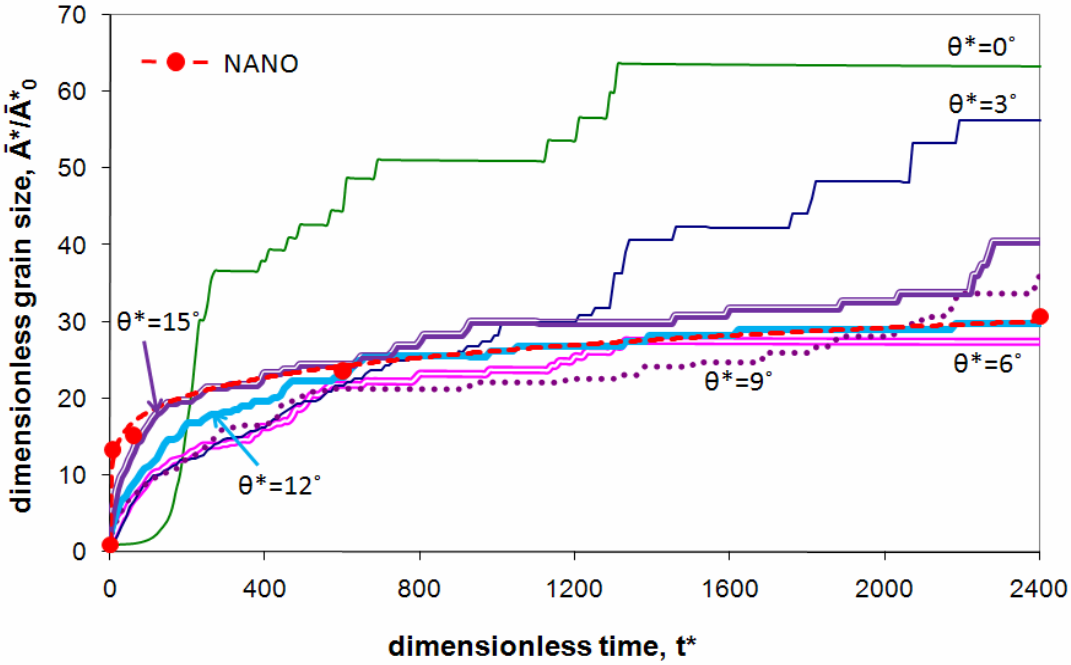

Figure 8-2 Simulated grain growth behavior for different coalescence degrees by varying the misorientation threshold (θ*), where θ*=12˚ and 15˚show strong agreement in initial rapid growth rate and the final grain size with NANO, suggesting that grain growth of nanosized powder is via grain coalescence dominated solid-state sintering model.

curve for θ*=0˚ from NANO suggests that grain growth of nanosized powder deviated from classic curvature migration. Rapid initial growth rate for θ*> 0˚ may be attributes to grain coalescence that widens the size distribution and subsequently leads to the consumption of fine grains at a fast rate. It is found that the higher the coalescence degree, the faster the initial growth rate. The slowdown in growth rate is postulate when the entire fine grains are being consumed and the coarse grains impinged upon one another thus competing to grow at a slower pace. For low θ*, 3˚, 6˚ and 9˚, the growth curves are almost overlapping one another before t*=600. Consider random condition, the limited amount of coalesced cluster and coalescence size are distribute homogenously in the fine grain matrix, promoting grain growth at a

constant rate. Despite the discrepancies of 2-D phase field simulation mentioned in Section 8.1, curves of θ*=12º and 15˚ are in strong agreement with NANO, in term of the final grain size and initial growth rate, implying that grain growth is via the proposed grain coalescence dominated solid-state sintering model. To control the grain growth, simulation result suggests that short sintering duration is beneficial for material with small misorientation threshold, θ*≤9˚, while long sintering duration is in advantage for material with high θ*, if comparing the curve for θ*=3 and 15˚. A mixture of 50% grain in the size ranging between 2 to 7 times coarser than the nanosized powder appears to best inhibit grain growth, as demonstrated by θ*=6˚.

8.2.2 Morphology Evolution

Microstructure evolution is a direct approach to understand the grain growth behavior. It provides extra information about the evolution of porosity as well as grain shape and size distribution. Figure 8-3 compares microstructure evolution of different θ*. The initial microstructure is identical for all cases, except the difference in coalescence degree. When the θ≤ θ*, the grains appear as a cluster of powder without grain boundaries in between. For non coalescence case (θ*=0˚), grain growth is initially inhibited due to the monosized distribution. The nanosized powder becomes unstable and grows to reduce the system free energy. Typically, those grains at a loose packing region grow first, as discussed in Section 5.3.2. Other θ* involved certain level of coalescence cluster. These clusters rapidly evolve to coarse grains by consuming the surrounding fine grains. From t*=6 onwards, the fine starting powder

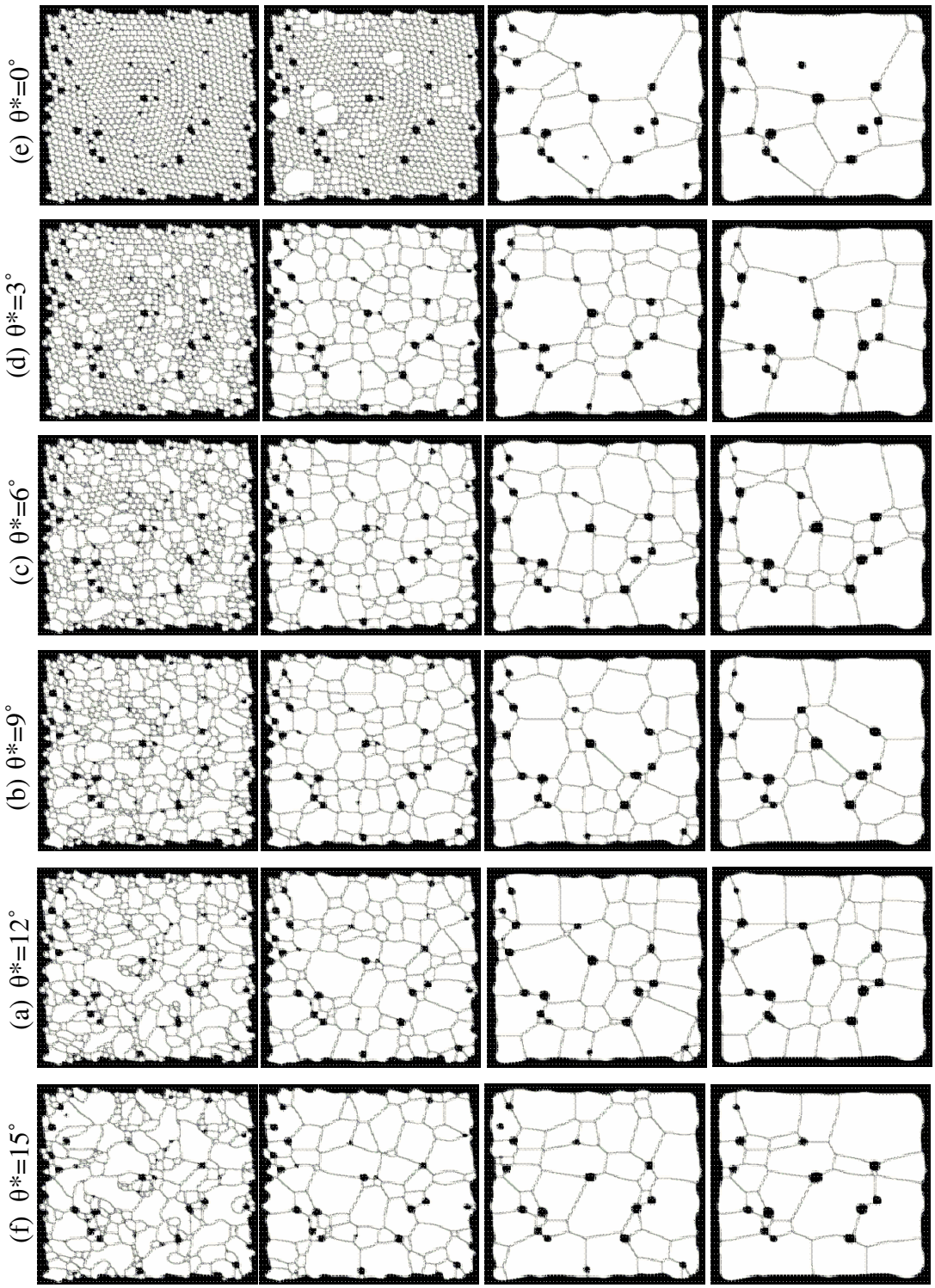

Figure 8-3 Microstructure for different misorientation thresholds, θ* at t*=6, 60, 600, 2400 respectively. With grain coalescence, the average grain size is higher than the case without coalescence (θ*=0˚) at t*<60. Surprisingly grain coalescence somehow slow down the grain growth, result in the smaller grain size for t*=600 onwards

can hardly be traced. From t*<60, the microstructure development is very fast and from t*=60 onwards, it is rather slow. Referring to the Figure 8-3, the growth rate is very much dependent on the impingement of coarse grains. This is clear for θ*=3, 6 and 9˚ when comparing the microstructure at t*= 6 and 60. Even though with different amount of remaining fine grains at t*=6, their microstructures for t*=60 are similar. Most of the fine powders have disappeared during the transition from t*=0 to 60. Therefore for t*> 60, the coarse grains impinge upon one another, slowing down the subsequent grain growth. The simulated morphology evolution for θ*=12˚ and 15˚ show substantial agreement with empirical finding on 50nm 3Y-TZP that discussed in Section 4.2.3, again support the proposed grain coalescence dominated solid-state sintering model.

8.2.3 Irregular Shaped Grains

To understand the rapid evolution of irregular shaped grains, Figure 8-4 compares the simulated microstructure at t*=0, 2 and 4. At t*=0, initial structure for all θ* appears in the same random packed structure, with only minor difference in some powder clusters that without a clear boundary. Those powder clusters are simulated as the program assumed no boundary for powders that are in same orientation. At t*=2, the coalesced powder clusters are obvious with their presence as irregular shape grains, typically several order coarser than the remaining fine powder. The irregularity increases with the increase of θ*. For low θ*, the coalescence size limited to 4 and 7 for θ*=3˚ and 6˚, respectively, referred to Figure 8-1. This causes

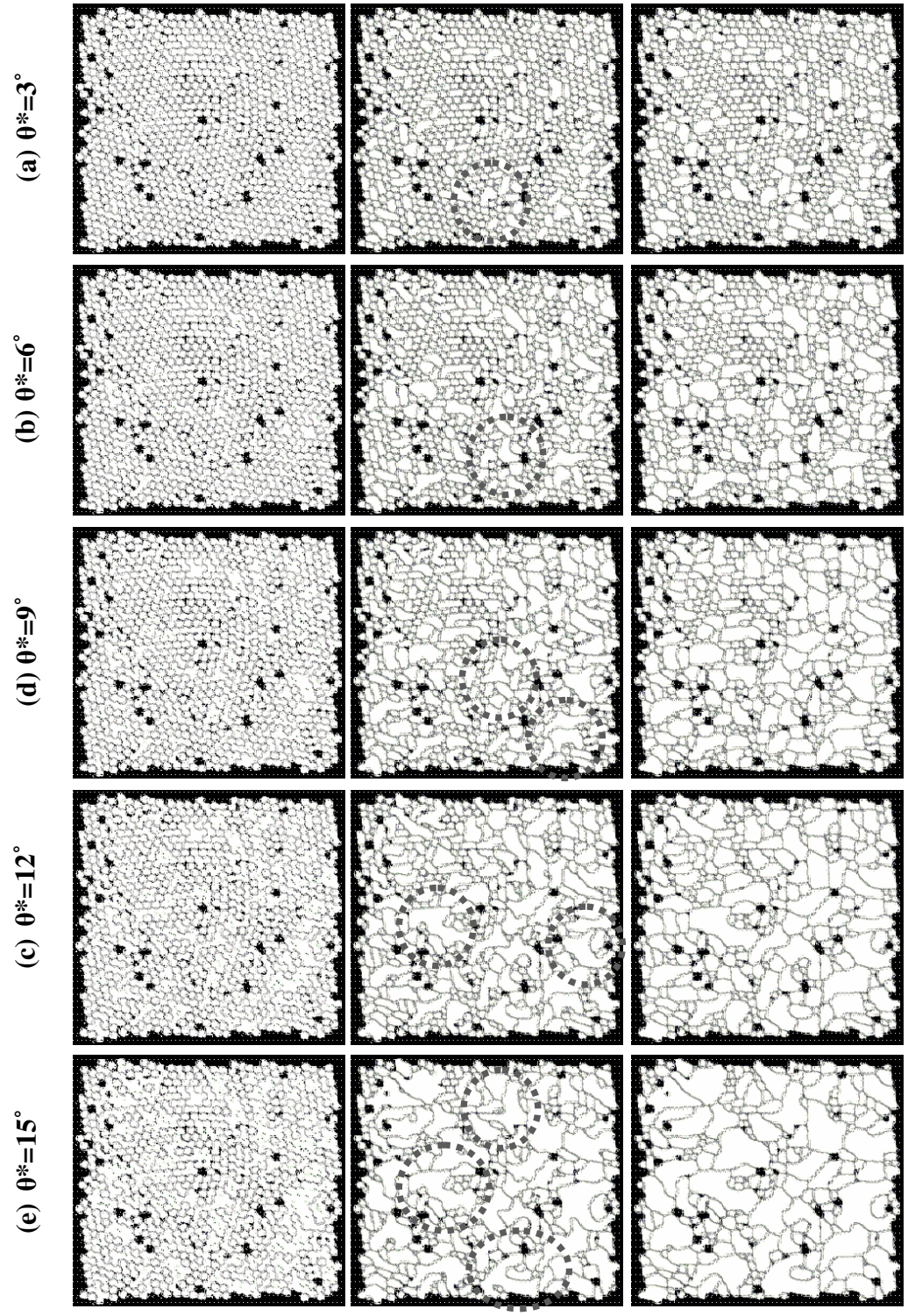

Figure 8-4 The evolution of irregular shape grains at initial stage of simulation, where from the left is t*=0, 2 and 4, respectively. Higher degree of misorientation threshold, θ* result in higher degree of irregularity. The irregularity further stimulates grain growth driven by curvature migration.

majority coalesced cluster are elongated in shape. For higher θ*, the coalescence size increase to 12, 20 and 27 respectively, for θ*=9˚, 12˚ and 15˚. This increase the chances for the coalesced cluster to be in irregular shape, such as "C", "Y" and "T" shape, as those circled in Figure 8-4. These irregular shapes and corrugated boundaries are also observed experimentally, as shown in Figure 4-8. However, only smooth and straight grain boundaries are simulated in Chapter 5. Therefore, the irregular shaped grains without straight grain boundary distinguish grain growth via curvature migration from other grain growth mechanism, such as grain coalescence.

These irregular shaped grains have high surface energy and will stimulate the grain growth driven by curvature migration. Within short simulation steps, when t*=4, most of the odd shape grains are evolving to normal grain shapes with straight grain boundary. Although no further grain coalescence occurs after t*=0, grain growth from t*=2 and 4 is significant as a result of the irregular shaped coalescence grains. This is consistent with the proposed grain coalescence dominated solid-state sintering model, where after grain coalescence, the contact point of coalesced grain serves as a suitable side for atom reattachment. The straight grain boundary has the lowest free energy, thus the odd curvature will evolve towards the straight boundary, at a faster pace compared to normal concave or convex boundary. The irregular shaped grains can hardly be traced even at such short simulation time where t*=4. The fast evolution of such irregular shape grain demonstrated in Figure 8-4 contributes to the extensive growth rate during initial sintering stage, observed in Figure 8-2. The fast evolution of irregular shaped grain can adequately explain why the irregular shape grains are predicted numerically[74, 152] but seldom observed experimentally. An irregular grain

that observed in tungsten carbide material was attributed to coalesced grain cluster [68]. The irregular shaped grains observed after 6 minutes sintering at 1350˚C, as discussed in Section 4.2.1 thus can be the evidence of grain coalescence.

8.3 Summary

For the first time, the influence of grain coalescence during solid-state sintering of nanosized powder was analyzed quantitatively and qualitatively using 2-D phase field simulation. With the incorporation of grain coalescence in random packed powder system, the simulation results were in qualitative agreement with experimental findings, in term of microstructure evolution and relative grain growth rate. The irregular shaped grains observed experimentally were also found in numerical simulation when considered grain coalescence. These suggested that the proposed grain coalescence dominated solid-state sintering model is likely responsible for the extensive grain growth at initial sintering stage of nanosized powder.

CHAPTER 9 CONCLUSION AND FUTURE WORK

9.1 Main Contributions

This research has first demonstrated the feasibility of micro powder injection molding (μPIM) for industry application by producing 3 mm micro gear using 50 nm 3 mol % yttria stabilized zirconia (3Y-TZP) powder. The critical issues emerged from the high surface area per unit volume of the nanosized powder (i.e. agglomeration) and the micron size features (i.e. incomplete demolding) were overcome. The sintered micro gear showed good shape retention and well defined gear teeth. The high hardness and toughness of 3Y-TZP was preserved in micro features molded using nanosized powder.

The project then investigated the sintering behavior of nanosized powder processed by powder injection molding. The isothermal sintering at temperature of 1300ºC demonstrated a very rapid growth initially, within 6 minutes, and a slowdown afterward. The extensive grain growth behavior in the initial sintering stage is consistent with prior works that used even lower sintering temperature, shorter holding duration, and higher compaction force or pressurized sintering environment. This extensive growth is inexplicable simply due to its nanosize. The presence of irregular shaped grains suggests that the extensive grain growth may be attributed to grain coalescence.

Grain growth based on classic curvature migration theory during solid-state sintering was simulated using phase field approach. Simulated fine powder was stable initially then rapidly grew to 6 times coarser. The growth started at loose packing area where the fine powders gained advantage in mass transport due to vacancies concentration and additional surface and vapor diffusion activities at pore region. These resulted in localized growth region and triggered rapid growth when the coarse grains consumed neighboring fine grains at a rapid rate. The simulation result suggested that the curvature migration itself cannot cause extensive initial grain growth observed in nanosized powder. From the trace of irregular shaped grains in experimental observation, grain coalescence may be of importance in causing the extensive grain growth during early stage of sintering.

A grain coalescence dominated solid-state sintering model was proposed in Chapter 5. Grain coalescence is a natural process that occurrs on top of curvature migration for free energy minimization. In the proposed model, the complex process of grain rotation and sintering force were simplified with the introduction of a misorientation threshold, θ^*. Neighboring grains within the misorientation threshold were considered as coincident grains that have zero mismatch and they coalesced to further reduce the system free energy. The misorientation threshold was proposed to be dependent on starting powder size, powder shape, initial packing, sintering temperature, holding duration at sintering and pressurized condition during sintering. The grain coalescence dominated solid-state sintering model was predicted to be significant at initial stage, when sintering force was less than rotation torque. The significance was dependent on the frequency of the grains to be in such small

misorientation threshold during initial sintering stage and thus, able to coalesce to further reduce the system free energy.

To determine the significance of grain coalescence in solid-state sintering, a probability analysis based on crystallite geometry was carried out. The analysis found high frequency of low angle grains that had misorientation less than 15º with its neighbors. For tetragonal structure of 3Y-TZP, almost 50% grains were found to be low angle grains. The percentage of low angle grains was unexpectedly high, thus suggesting that the grain coalescence may be extremely important when rotation of fine grain/ particle is possible.

With the quantitative result in probability analysis, the significance of grain coalescence was postulated using phase field simulation incorporating grain coalescence probability. Different degrees of misorientation threshold represented the flexibility in grain rotation. With the increase of misorientation threshold, between 12-15º, the initial growth became obvious followed by a plateau of slow growth. Coalescence of low angle grains instantaneously increased the grain size at initial stage and widened the size distribution. The coalesced coarse grains then grew at the expense of the non-coalesced fine grains via curvature migration. Once the fine grains were being consumed, the coarse grains impinged upon one another and competed to grow at a slow pace. This is in strong agreement with experiment results of nanosized 3Y-TZP powder, suggesting that the grain growth of nanosized powder was according to the proposed grain coalescence dominated solid-state sintering model.

9.2 Recommendation for Future Work

There are several limitations in this project. μPIM becomes more challenging with the decrease of powder and feature size. Even though μPIM of 3 mm micro gear using 50 nm 3Y-TZP powder was demonstrated experimentally, it may only serve as a guide line when changing to other features or materials. Viscosity measurement on the feedstock is highly recommended if available to optimize the powder binder ratio and injection molding temperature. Due to the high powder price and processing difficulties, μPIM of nanosized powder may be primarily applied to very fine features when micron size powder is no longer applicable. For the 3 mm micro gear, 5 μm mono dispersed powder, if available, may be a better choice at lower cost with less processing difficulties. To highlight the advantages of μPIM using 50 nm powder, features as fine as 0.5 μm should be demonstrated. However, such fine feature is currently not available in this lab.

The proposed grain coalescence dominated solid-state sintering model should be applicable to all nanosized powder where powder size is smaller than the critical size for grain rotation. The significance of grain coalescence however, depends on the crystal structure and the rotation ability. This project only did a preliminary modeling based on the probability of low angle grains for tetragonal structure and simplified the complicated driving force and restriction force for grain rotation by introducing a misorientation threshold. Grain coalescence in three dimensions was found to be different from two dimensional planar simulations in term of average coordination number, coalescence size and percentage. When computational capability is affordable, three dimensional phase field simulation should be used to study and

validate the actual relationship between misorientation threshold and grain growth behavior. In addition, the phase field algorithm is written based on a general double well potential, without considering the temperature factor. This can only predict the isothermal sintering condition. As suggested experimentally, sintering cycle is optimized using a two-stage sintering profile, the actual energy potential as a function of sintering temperature needs to be determined to predict the grain growth at different sintering profiles.

For the first time, grain coalescence dominated solid-state sintering for nanosized powder was proposed and its effect on microstructure evolution was analyzed quantitatively and qualitatively. The proposed grain coalescence dominated solid-state sintering model appeared appropriate in explaining the growth mechanism in nanosized particle/grain structure. It is crucial to understand the extensive growth in initial sintering stage of nanosized powder so as to control the final grain size and grain size dependent properties. Understanding the mechanism of this extensive growth during initial sintering stage provides the direction for grain refinement technology involved nanosized starting powder. Apparently, a good mixture in powder sizes, such as with 50% coarse powder that is 2-7 times larger than the nanosized powder, appeared to slow down the growth rate for single phase material. Alternatively, a good mixture in materials will reduce the probability in perfectly matched crystallography structure even with the ease of fine grain rotation, thus reducing the extensive initial growth due to grain coalescence.

On the other hand, μPIM becomes increasingly important in the light of current trends toward miniaturization. It provides an alternative to produce high

performance micro component. With the development in bi-material injection molding, μPIM can be used to produce functional micro components, such as combination of magnetic and non-magnetic micro component without additional joining process. Moreover, novel material properties of nanostructure may be achieved in near future with the technology to inhibit nanosized particle/grain coalescence. This will open up a huge market opportunity for μPIM using nanosized powder to produce micro component with improved tribological, mechanical or corrosion properties.

BIBLIOGRAPHY

1. Nieh, T.G. and J. Wadsworth, *Superelastic behaviour of a fine-grained, yttria-stabilized, tetragonal zirconia polycrystal (Y-TZP).* Acta Metallurgica et Materialia, 1990. **38**(6): p. 1121-1133.

2. Bikramjit Basu, J.-H.L.D.-Y.K., *Development of Nanocrystalline Wear-Resistant Y-TZP Ceramics.* Journal of the American Ceramic Society, 2004. **87**(9): p. 1771-1774.

3. Bourell, D.L., Parimal, and W. Kaysser, *Sol-Gel Synthesis of Nanophase Yttria-Stabilized Tetragonal Zirconia and Densification Behavior below 1600 K.* Journal of the American Ceramic Society, 1993. **76**(3): p. 705-711.

4. Sagel-Ransijn, C.D., et al., *Grain growth in ultrafine-grained Y-TZP ceramics.* Journal of the European Ceramic Society, 1997. **17**(9): p. 1133-1141.

5. Sagel-Ransijn, C.D., et al., *Production of defect-poor nanostructured ceramics of Yttria-Zirconia.* Journal of the European Ceramic Society, 1997. **17**(6): p. 831-841.

6. Liu, D.-M., *Densification of zirconia from submicron-sized to nano-sized powder particles.* Journal of Materials Science Letters, 1998. **17**(6): p. 467-469.

7. Li, W. and L. Gao, *Compacting and sintering behavior of nano ZrO2 powders.* Scripta Materialia, 2001. **44**(8-9): p. 2269-2272.

8. Maca, K., M. Trunec, and P. Dobsak, *Bulk Zirconia Nanoceramics prepared by Cold Isostatic Pressing and Pressureless Sintering* Reviews on Advanced Materials Science, 2005. **10**(1): p. 84-88.

9. Mazaheri, M., A. Simchi, and F. Golestani-Fard, *Densification and grain growth of nanocrystalline 3Y-TZP during two-step sintering.* Journal of the European Ceramic Society. **In Press, Corrected Proof**.

10. Chen, S.G., et al., *Reduced activation energy and crystalline size for yttria-*

stabilized zirconia nano-crystals: an experimental and theoretical study. Journal of Crystal Growth, 2004. **267**(1-2): p. 100-109.

11. David L. Bourell, P.W.K., *Sol-Gel Synthesis of Nanophase Yttria-Stabilized Tetragonal Zirconia and Densification Behavior below 1600 K.* Journal of the American Ceramic Society, 1993. **76**(3): p. 705-711.

12. Martin Trunec, K.M., *Compaction and Pressureless Sintering of Zirconia Nanoparticles.* Journal of the American Ceramic Society, 2007. **90**(9): p. 2735-2740.

13. Trunec, M. and K. Maca, *Compaction and Pressureless Sintering of Zirconia Nanoparticles.* Journal of the American Ceramic Society, 2007. **90**(9): p. 2735-2740.

14. Vladimir V. Srdi, M.W.H.H., *Sintering Behavior of Nanocrystalline Zirconia Prepared by Chemical Vapor Synthesis.* Journal of the American Ceramic Society, 2000. **83**(4): p. 729-736.

15. Zych, L. and K. Haberko, *Filter pressing and sintering of a zirconia nanopowder.* Journal of the European Ceramic Society, 2006. **26**(4-5): p. 373-378.

16. Hague, D.C. and M.J. Mayo, *Sinter-Forging of Nanocrystalline Zirconia: I, Experimental.* Journal of the American Ceramic Society, 1997. **80**(1): p. 149-156.

17. Kim, H.-C., et al., *Sintering of ultra-fine tetragonal yttria-stabilized zirconia ceramics.* Journal of Materials Science, 2007. **42**(22): p. 9409-9414.

18. Trunec, M., K. Maca, and Z. Shen, *Warm pressing of zirconia nanoparticles by the spark plasma sintering technique.* Scripta Materialia, 2008. **59**(1): p. 23-26.

19. Lee, W.E. and W.M. Rainforth, *Ceramic Microstructures: Property Control by Processing*. 1994: Kluwer Academic Publishers.

20. German, R.M., *Sintering theory and practice*. Vol. 893073. 1996, New York: : Wiley.

21. Brook, R.J., *Processing technology for high performance ceramics.* Materials science and engineering, 1985. **71**(1-2): p. 305-312.

22. Duran, P., et al., *Densification behaviour, microstructure development and dielectric properties of pure BaTiO3 prepared by thermal decomposition of (Ba, Ti)-citrate polyester resins.* Ceramics International, 2002. **28**(3): p. 283-292.

23. Duran, P., et al., *Nanostructured and near defect-free ceramics by low-temperature pressureless sintering of nanosized Y-TZP powders.* Journal of Materials Science, 1997. **32**(17): p. 4507-4512.

24. Groza, J.R. and C. Suryanarayana, *Chapter 13 Powder consolidation*, in *Pergamon Materials Series*. 1999, Pergamon. p. 347-372.

25. German, R.M. and A. Bose, *Injection molding of metals and ceramics*. 1997, Princeton, N.J., U.S.A. :: Metal Powder Industries Federation.

26. Yoshikawa, K. and H. Ohmori, *Outstanding features of powder injection molding for micro parts manufacturing*. 2001, RIKEN Review. p. 13-18.

27. Kirkland, C., *A look at the market for powder injection molding*, in *immnet*. 1997.

28. *Polymer Nano-Rheology Lab, Department of Chemical Engineering, POSTECH, Korea* [cited 13 Oct 2008]; Available from: http://www.postech.ac.kr/see/pmr/work.htm.

29. Karatas, C., et al., *Rheological properties of feedstocks prepared with steatite powder and polyethylene-based thermoplastic binders.* Journal of Materials Processing Tech., 2004. **152**(1): p. 77-83.

30. Cornwall, R.G. and R.M. German, *Powder Injection Molding – World Markets and Technologies*. 1997, Center For Advance Vehicular Systems.

31. Loh, N., et al., *Fabrication of micro gear by micro powder injection molding.* Microsystem Technologies, 2008. **14**(1): p. 43-50.

32. Baek, E.R., et al., *Effect of Particle Size in Feedstock Properties in Micro*

Powder Injection Molding. Materials Science Forum. **534-536**: p. 349-352.

33. German, R.M., *Injection molding of metals and ceramics*. 1997, Princeton, N.J., U.S.A. : Metal Powder Industries Federation.

34. Xie, Z.-p., et al., *The effect of organic vehicle on the injection molding of ultra-fine zirconia powders.* Materials & Design, 2005. **26**(1): p. 79-82.

35. Song, J.H. and J.R.G. Evans, *The injection moulding of fine and ultra-fine zirconia powders.* Ceramics International, 1995. **21**(5): p. 325-333.

36. Trunec, M. and J. Hrazdera, *Effect of ceramic nanopowders on rheology of thermoplastic suspensions.* Ceramics International, 2005. **31**(6): p. 845-849.

37. Wu, R.-Y. and W.-C.J. Wei, *Kneading behaviour and homogeneity of zirconia feedstocks for micro-injection molding.* Journal of the European Ceramic Society, 2004. **24**(14): p. 3653-3662.

38. Luo, J., et al., *Injection Moulding of Ultra-fine Zirconia (Y-TZP) Powders.* Journal of Ceramic Processing & Research, 2006. **7**(1): p. 14-19.

39. Trunec, M., P. Dobsák, and J. Cihlár, *Effect of powder treatment on injection moulded zirconia ceramics.* Journal of the European Ceramic Society, 2000. **20**(7): p. 859-866.

40. Ruprecht, R., et al., *Injection molding of microstructured components from plastics, metals and ceramics.* Microsystem Technologies, 2002. **8**(4): p. 351-358.

41. Osada, T., et al., *Effect of Mixing Condition on Feedstock Properties for Micro Size Parts by MIM.* Advances in Powder Metallurgy and Particulate Materials, 2003: p. 8-52.

42. Liu, L., et al., *Mixing and characterisation of 316L stainless steel feedstock for micro powder injection molding.* Materials Characterization, 2005. **54**(3): p. 230-238.

43. Tay, B.Y., et al., *Injection molding of 3D microstructures by μPIM.* Microsystem Technologies, 2005. **11**(2): p. 210-213.

44. Fu, G., et al., *A micro powder injection molding apparatus for high aspect ratio metal micro-structure production.* JOURNAL OF MICROMECHANICS AND MICROENGINEERING, 2007. **17**(9): p. 1803.

45. Li, S.G., et al., *Dimensional variation in production of high-aspect-ratio micro-pillars array by micro powder injection molding.* Applied Physics A: Materials Science & Processing, 2007. **89**(3): p. 721-728.

46. Yin, H., X. Qu, and C. Jia, *Fabrication of micro gear wheels by micropowder injection molding.* Journal of University of Science and Technology Beijing, 2008. **15**(4): p. 480-483.

47. Supriadi, S., et al., *Binder system for STS 316 nanopowder feedstocks in micro-metal injection molding.* Journal of Materials Processing Tech., 2007. **187**: p. 270-273.

48. Fu, G., et al., *A variotherm mold for micro metal injection molding.* Microsystem Technologies, 2005. **11**(12): p. 1267-1271.

49. Fu, G., et al., *The demolding of powder injection molded micro-structures: analysis, simulation and experiment.* Journal of Micromechanics and Microengineering, 2008. **18**(7): p. 075024.

50. Liu, L., et al., *Micro powder injection molding: Sintering kinetics of microstructured components.* Scripta Materialia, 2006. **55**(12): p. 1103-1106.

51. German, R.M., *Powder injection molding : design and applications*. 2003, State College, PA :: Innovative Materials Solutions.

52. De Jonghe, L.C. and M.N. Rahaman, *4.1 Sintering of Ceramics*, in *Handbook of Advanced Ceramics*. 2003, Academic Press: Oxford. p. 187-264.

53. Burke, J.E. and D. Turnbull, *Recrystallization and grain growth.* Progress in Metal Physics, 1952. **3**: p. 220-244.

54. Chen, D.J. and M.J. Mayo, *Densification and grain growth of ultrafine 3 mol % Y_2O_3-ZrO_2 ceramics.* Nanostructured Materials, 1993. **2**(5): p. 469-478.

55. Morris, M.A. and H.M. Reidy, *Preparation of ceria-zirconia and yttria-zirconia*

mixed oxides of unusual pore structures. Ceramics International, 2005. **31**(7): p. 929-935.

56. Morita, K. and K. Hiraga, *Critical assessment of high-temperature deformation and deformed microstructure in high-purity tetragonal zirconia containing 3 mol.% yttria.* Acta Materialia, 2002. **50**(5): p. 1075-1085.

57. Ross, I.M., et al., *The role of trace additions of alumina to yttria-tetragonal zirconia polycrystals (Y-TZP).* Scripta Materialia, 2001. **45**(6): p. 653-660.

58. Liu, C., et al., *Progress on grain growth dynamics in sintering of nano-powders.* Rare Metals, 2006. **25**(6, Supplement 1): p. 471-475.

59. Groza, J.R., *Nanosintering.* Nanostructured Materials, 1999. **12**(5-8): p. 987-992.

60. Li, J.C.M., *Possibility of Subgrain Rotation during Recrystallization.* Journal of Applied Physics, 1962. **33**(10): p. 2958-2965.

61. Penn, R.L. and J.F. Banfield, *Imperfect Oriented Attachment: Dislocation Generation in Defect-Free Nanocrystals.* Science, 1998. **281**(5379): p. 969-971.

62. Banfield, J.F., et al., *Aggregation-Based Crystal Growth and Microstructure Development in Natural Iron Oxyhydroxide Biomineralization Products.* Science, 2000. **289**(5480): p. 751-754.

63. Leite, E.R., et al., *Crystal growth in colloidal tin oxide nanocrystals induced by coalescence at room temperature.* Applied Physics Letters, 2003. **83**(8): p. 1566-1568.

64. Courtney, T.H. and J.K. Lee, *An Analysis for Estimating the Probability of Particle Coalescence in Liquid Phase Sintered Systems.* Metall. Trans. A, 1980. **11**(6): p. 943-947.

65. Harris, K.E., V.V. Singh, and A.H. King, *Grain rotation in thin films of gold.* Acta Materialia, 1998. **46**(8): p. 2623-2633.

66. Koga, K. and H. Takeo, *In situ observation of coalescence growth of small gold clusters by X-ray diffraction technique.* The European Physical Journal D -

Atomic, Molecular, Optical and Plasma Physics, 1999. **9**(1): p. 535-538.

67. Chaim, R., *Densification mechanisms in spark plasma sintering of nanocrystalline ceramics.* Materials Science and Engineering: A, 2007. **443**(1-2): p. 25-32.

68. Wang, X., Z.Z. Fang, and H.Y. Sohn, *Grain growth during the early stage of sintering of nanosized WC–Co powder.* International Journal of Refractory Metals and Hard Materials, 2008. **26**(3): p. 232-241.

69. Moldovan, D., D. Wolf, and S.R. Phillpot, *Theory of diffusion-accommodated grain rotation in columnar polycrystalline microstructures.* Acta Materialia, 2001. **49**(17): p. 3521-3532.

70. Moldovan, D., et al., *Role of grain rotation during grain growth in a columnar microstructure by mesoscale simulation.* Acta Materialia, 2002. **50**(13): p. 3397-3414.

71. Moldovan, D., et al., *Scaling Behavior of Grain-Rotation-Induced Grain Growth.* Physical Review Letters, 2002. **89**(20): p. 206101.

72. Haslam, A.J., et al., *Mechanisms of grain growth in nanocrystalline fcc metals by molecular-dynamics simulation.* Materials Science and Engineering A, 2001. **318**(1-2): p. 293-312.

73. Raj, R. and M.F. Ashby, *On grain boundary sliding and diffusional creep.* Metallurgical and Materials Transactions B, 1971. **2**(4): p. 1113-1127.

74. Chen, L.Q. and W. Yang, *Computer simulation of the domain dynamics of a quenched system with a large number of nonconserved order parameters: The grain-growth kinetics.* Physical Review B, 1994. **50**(21): p. 15752-15756.

75. Yang, W., L.-Q. Chen, and G.L. Messing, *Computer simulation of anisotropic grain growth.* Materials Science and Engineering A, 1995. **195**: p. 179-187.

76. Upmanyu, M., et al., *Simultaneous grain boundary migration and grain rotation.* Acta Materialia, 2006. **54**(7): p. 1707-1719.

77. Shi, J.L., et al., *Microstructure and micro-mechanical properties of Y-TZP and*

Y-TZP/Al2O3 composite after superplastic deformation. Acta Materialia, 1998. **46**(6): p. 1923-1932.

78. Vleugels, J., Z.X. Yuan, and O. Van Der Biest, *Mechanical properties of Y2O3/Al2O3-coated Y-TZP ceramics.* Journal of the European Ceramic Society, 2002. **22**(6): p. 873-881.

79. Yuan, Z.X., J. Vleugels, and O. Van Der Biest, *Synthesis and characterisation of CeO2-coated ZrO2 powder-based TZP.* Materials Letters, 2000. **46**(5): p. 249-254.

80. Xu, T., et al., *Phase stability and mechanical properties of TZP with a low mixed Nd2O3/Y2O3 stabiliser content.* Journal of the European Ceramic Society, 2006. **26**(7): p. 1205-1211.

81. Chinn, R.E., *Ceramography: Preparation and Analysis of Ceramic Microstructures*. 2002: Wiley-American Ceramic Society.

82. Morita, K. and K. Hiraga, *Deformed substructures in fine-grained tetragonal zirconia.* Philosophical Magazine Letters, 2001. **81**(5): p. 311-319.

83. Bukaemskiy, A.A., D. Barrier, and G. Modolo, *Physical properties of 8 mol% Ceria doped yttria stabilised zirconia powder and ceramic and their behaviour during annealing and sintering.* Journal of the European Ceramic Society, 2006. **26**(8): p. 1507-1515.

84. Zhu, Q. and B. Fan, *Low temperature sintering of 8YSZ electrolyte film for intermediate temperature solid oxide fuel cells.* Solid State Ionics, 2005. **176**(9-10): p. 889-894.

85. Fleischer, J. and A.M. Dieckmann, *Automation of the powder injection molding process.* Microsystem Technologies, 2006. **12**(7): p. 702-706.

86. Hwang, K.S. and Y.M. Hsieh, *Comparative study of pore structure evolution during solvent and thermal debinding of powder injection molded parts.* Metallurgical and Materials Transactions A, 1996. **27**(2): p. 245-253.

87. Oliveira, R.V.B., et al., *Ceramic injection moulding: influence of specimen dimensions and temperature on solvent debinding kinetics.* Journal of Materials

Processing Technology, 2005. **160**(2): p. 213-220.

88. Thomas-Vielma, P., et al., *Production of alumina parts by powder injection molding with a binder system based on high density polyethylene.* Journal of the European Ceramic Society, 2008. **28**(4): p. 763-771.

89. Liu, Z.Y., et al., *Binder system for micropowder injection molding.* Materials Letters, 2001. **48**(1): p. 31-38.

90. Kingery, W.D. and B. Francois, *The Sintering of Crystalline Oxides: I.* Interactions between Grain Boundaries and Pores in GC Kuczynski, NA Hooton and CF Gibbon (Eds.) Sintering and Related Phenomena, Gordon and Breach, New York, 1967: p. 471.

91. Chen, P.L. and I.W. Chen, *Sintering of Fine Oxide Powders: II, Sintering Mechanisms.* Journal of the American Ceramic Society, 1997. **80**(3): p. 637-645.

92. Lawn, B.R. and D.B. Marshall, *Hardness, Toughness, and Brittleness: An Indentation Analysis.* Journal of The American Ceramic Society 1979. **62**: p. 347-350.

93. Theunissen, G.S.A.M., A.J.A. Winnubst, and A.J. Burggraaf, *Sintering kinetics and microstructure development of nanoscale Y-TZP ceramics.* Journal of the European Ceramic Society, 1993. **11**(4): p. 315-324.

94. Moya, J.S., et al., *Sintering*, in *Encyclopedia of Physical Science and Technology*. 2001, Academic Press: New York. p. 865-878.

95. Lasalmonie, A. and J.L. Strudel, *Influence of grain size on the mechanical behaviour of some high strength materials.* Journal of Materials Science, 1986. **21**(6): p. 1837-1852.

96. Nieman, G.W., J.R. Weertman, and R.W. Siegel, *Microhardness of nanocrystalline palladium and copper produced by inert-gas condensation.* Scr. Metall, 1987. **23**: p. 2013.

97. Takeuchi, S., *The mechanism of the inverse Hall-Petch relation of nanocrystals.* Scripta Materialia, 2001. **44**(8-9): p. 1483-1487.

98. Giga, A., et al., *Demonstration of an inverse Hall–Petch relationship in electrodeposited nanocrystalline Ni–W alloys through tensile testing.* Scripta Materialia, 2006. **55**(2): p. 143-146.

99. Hahn, H., P. Mondal, and K.A. Padmanabhan, *Plastic deformation of nanocrystalline materials.* Nanostructured Materials, 1997. **9**(1-8): p. 603-606.

100. Bohn, R., T. Klassen, and R. Bormann, *Room temperature mechanical behavior of silicon-doped TiAl alloys with grain sizes in the nano-and submicron-range.* Acta Materialia, 2001. **49**(2): p. 299-311.

101. Padmanabhan, K.A., *Mechanical properties of nanostructured materials.* Materials Science & Engineering A, 2001. **304**: p. 200-205.

102. Schuh, C.A., T.G. Nieh, and T. Yamasaki, *Hall–Petch breakdown manifested in abrasive wear resistance of nanocrystalline nickel.* Scripta Materialia, 2002. **46**(10): p. 735-740.

103. Bellosi, A., D. Sciti, and S. Guicciardi, *Synergy and competition in nano-and micro-design of structural ceramics.* Journal of the European Ceramic Society, 2004. **24**(12): p. 3295-3302.

104. Guicciardi, S., et al., *Nanoindentation Characterization of Submicro-and Nano-Sized Liquid-Phase-Sintered SiC Ceramics.* Journal of the American Ceramic Society, 2004. **87**(11): p. 2101-2107.

105. Lee, S.-Y., *Sintering behavior and mechanical properties of injection-molded zirconia powder.* Ceramics International, 2004. **30**(4): p. 579-584.

106. Chen, I.W. and X.H. Wang, *Sintering dense nanocrystalline ceramics without final-stage grain growth.* Nature, 2000. **404**(6774): p. 168-171.

107. Zhang, H., M. Upmanyu, and D.J. Srolovitz, *Curvature driven grain boundary migration in aluminum: molecular dynamics simulations.* Acta Materialia, 2005. **53**(1): p. 79-86.

108. Robach, J.S., et al., *In-situ transmission electron microscopy observations and molecular dynamics simulations of dislocation-defect interactions in ion-irradiated copper.* Philosophical Magazine, 2003. **83**(8): p. 955-967.

109. Upmanyu, M., et al., *Molecular dynamics simulation of triple junction migration.* Acta Materialia, 2002. **50**(6): p. 1405-1420.

110. Zhu, H. and R.S. Averback, *Molecular dynamics simulations of densification processes in nanocrystalline materials.* Materials Science and Engineering A, 1995. **204**(1-2): p. 96-100.

111. Xiao, S. and W. Hu, *Molecular dynamics simulations of grain growth in nanocrystalline Ag.* Journal of Crystal Growth, 2006. **286**(2): p. 512-517.

112. Bacon, D.J., F. Gao, and Y.N. Osetsky, *The primary damage state in fcc, bcc and hcp metals as seen in molecular dynamics simulations.* Journal of Nuclear Materials, 2000. **276**(1-3): p. 1-12.

113. Zhu, H. and R.S. Averback, *Sintering processes of two nanoparticles: a study by molecular dynamics.* Philos. Mag. Lett, 1996. **73**: p. 27–33.

114. Radhakrishnan, B., G.B. Sarma, and T. Zacharia, *Modeling the kinetics and microstructural evolution during static recrystallization—Monte Carlo simulation of recrystallization.* Acta Materialia, 1998. **46**(12): p. 4415-4433.

115. Soneda, N., et al., *Modeling the microstructural evolution in bcc-Fe during irradiation using kinetic Monte Carlo computer simulation.* Journal of Nuclear Materials, 2003. **323**(2-3): p. 169-180.

116. Saito, Y., *Monte Carlo simulation of grain boundary precipitation.* Materials Science and Engineering: A, 1997. **223**(1-2): p. 125-133.

117. Saito, Y. and M. Enomoto, *Monte Carlo Simulation of Grain Growth.* ISIJ International, 1992. **32**(3): p. 267-274.

118. Saito, Y., *The Monte Carlo simulation of microstructural evolution in metals.* Materials Science and Engineering: A, 1997. **223**(1-2): p. 114-124.

119. Saito, Y., *The Monte Carlo simulation of microstructural evolution in metals.* Materials science & engineering. A, Structural materials: properties, microstructure and processing, 1997. **223**(1-2): p. 114-124.

120. Saito, Y. and H. Harada, *The Monte Carlo simulation of ordering kinetics in Ni-*

base superalloys. Materials Science and Engineering: A, 1997. **223**(1-2): p. 1-9.

121. Caleyo, F., T. Baudin, and R. Penelle, *Monte Carlo simulation of recrystallization in Fe-50%Ni starting from EBSD and bulk texture measurements.* Scripta Materialia, 2002. **46**(12): p. 829-835.

122. Saito, Y., *The Monte Carlo simulation of the ordering kinetics of fcc to Ll2 structure in NiAlX ternary alloys.* Materials Science and Engineering: A, 1997. **223**(1-2): p. 10-16.

123. Song, X.Y. and G.Q. Liu, *A Simple and Efficient Three-Dimensional Monte Carlo Simulation of Grain Growth.* Scripta Materialia, 1998. **38**(11): p. 1691-1696.

124. Radhakrishnan, B. and T. Zacharia, *Simulation of curvature-driven grain growth by using a modified monte carlo algorithm.* Metallurgical and Materials Transactions A, 1995. **26**(1): p. 167-180.

125. Jang, Y.S., D.C. Ko, and B.M. Kim, *Application of the finite element method to predict microstructure evolution in the hot forging of steel.* Journal of Materials Processing Tech., 2000. **101**(1-3): p. 85-94.

126. Langer, S.A., E.R. Fuller, and W.C. Carter, *OOF: An Image-Based Finite-Element Analysis of Material Microstructures.* Computing in Science & Engineering, 2001: p. 15-23.

127. Chen, L.Q., *Introduction to the Phase-Field Method of Micostructure Evolution*, in *Continuum scale simulation of engineering materials: fundamentals, microstructures, process applications*. 2004, Wiley-VCH; John Wiley: Weinheim, Germany: Chichester p. 37-50.

128. Cahn, J.W., *Free Energy of a Nonuniform System.I. Interfacial Free Energy.* . J. Chem. Phys, 1958. **28**: p. 258-267.

129. Cahn, J.W. and S.M. Allen. *A Microscopic Theory For Domain Wall Motion And Its Experimental Verification In Fe-AI Alloy Domain Growth Kinetics*. 1977.

130. Wang, Y.U., *Computer modeling and simulation of solid-state sintering: A*

phase field approach. Acta Materialia, 2006. **54**(4): p. 953-961.

131. Cahn, J.W. and J.E. Hilliard, *Free Energy of a Nonuniform System I: Interfacial Free Energy.* The Journal of Chemical Physics, 1958. **28**(2): p. 258-267.

132. Al-Khafaji, A.W. and J.R. Tooley, *Numerical Methods in Engineering Practice*. 1986: Holt, Rinehart and Winston.

133. Vedantam, S. and B.S.V. Patnaik, *Efficient numerical algorithm for multiphase field simulations.* Physical Review E (Statistical, Nonlinear, and Soft Matter Physics), 2006. **73**(1): p. 016703-8.

134. Tikare, V., M. Braginsky, and E.A. Olevsky, *Numerical Simulation of Solid-State Sintering: I, Sintering of Three Particles.* Journal of the American Ceramic Society, 2003. **86**(1): p. 49-53.

135. Wakai, F., *Modeling and Simulation of Elementary Processes in Ideal Sintering.* Journal of the American Ceramic Society, 2006. **89**(5): p. 1471-1484.

136. Kang, S.J.L., *Sintering : densification, grain growth, and microstructure*. 2005, Oxford :: Elsevier Butterworth-Heinemann.

137. German, R.M., *Particle packing characteristics*. 1989, Princeton, N.J.: Metal Powder Industries Federation.

138. Bernstein, N., *The influence of geometry on grain boundary motion and rotation.* Acta Materialia, 2008. **56**(5): p. 1106-1113.

139. Cahn, J.W. and J.E. Taylor, *A unified approach to motion of grain boundaries, relative tangential translation along grain boundaries, and grain rotation.* Acta Materialia, 2004. **52**(16): p. 4887-4898.

140. Farkas, D., S. Mohanty, and J. Monk, *Linear Grain Growth Kinetics and Rotation in Nanocrystalline Ni.* Physical Review Letters, 2007. **98**(16): p. 165502-4.

141. Joshi, S.P. and K.T. Ramesh, *Rotational diffusion and grain size dependent shear instability in nanostructured materials.* Acta Materialia, 2008. **56**(2): p. 282-291.

142. Kim, B.N., K. Hiraga, and K. Morita, *Viscous grain-boundary sliding and grain rotation accommodated by grain-boundary diffusion.* Acta Materialia, 2005. **53**(6): p. 1791-1798.

143. Pignol, R.J., et al., *Grain rotation in 2d-hexagonal systems with competing interactions.* Physica B: Condensed Matter, 2007. **389**(1): p. 94-97.

144. Saetre, T.O. and N. Ryum, *On grain and subgrain rotations in two dimensions.* Metallurgical and Materials Transactions A, 1995. **26**(7): p. 1687-1697.

145. Wang, M., et al., *Consecutive Rotation of Crystallographic Orientation in Lateral Growth.* Physical Review Letters, 2005. **94**(12): p. 125505-4.

146. Wang, Y.B., et al., *Deformation-induced grain rotation and growth in nanocrystalline Ni.* Applied Physics Letters, 2008. **92**(1): p. 011903-3.

147. Winther, G., *Slip systems extracted from lattice rotations and dislocation structures.* Acta Materialia, 2008. **56**(9): p. 1919-1932.

148. Randle, V., *The role of the coincidence site lattice in grain boundary engineering.* 1997.

149. Gregg, R.A. and F.N. Rhines, *Surface tension and the sintering force in copper.* Metallurgical and Materials Transactions B, 1973. **4**(5): p. 1365-1374.

150. Beere, W., *The Second Stage Sintering Kinetics of Powder Compacts.* Acta Metall., 1975. **23**(1).

151. Warrington, D.H. and M. Boon, *Ordered structures in random grain boundaries; some geometrical probabilities.* Acta Metallurgica, 1975. **23**(5): p. 599-607.

152. Krill, C.E. and L.Q. Chen, *Computer simulation of 3-D grain growth using a phase-field model.* Acta Materialia, 2002. **50**(12): p. 3059-3075.

APPENDICES

A1 Phase field simulation written in FORTRAN language

```
C=============================================================
module etas
  integer,parameter::NN1=128,NN2=128,NACT=25,NUMGR=11000
  integer::nunieta,nprtcls
  double precision, parameter:: dx=1.0, dt=0.01
  integer,dimension(1:NN1,1:NN2) :: nactive,nactiven
  double precision,dimension(1:NN1,1:NN2,1:NACT,1:2)::eta,etanew
  double precision,dimension(1:NACT,1:8)::unieta
  double precision,dimension(1:NN1,1:NN2)::rho,rhon
  double precision,dimension(1:NUMGR):: part,rcx,rcy,area
end module etas
C=============================================================

PROGRAM pf2d
  use etas
  implicit none
  integer :: itime,totT
  integer::i,j,s,bdry,u1,u2,v1,v2
  double precision::temp
  double precision,dimension(1:NN1,1:NN2)::aveeta,maxeta

  interface
      subroutine initeta
      use etas
      implicit none
    end subroutine initeta
    subroutine velocity(time)
      use etas
      implicit none
      integer,intent(in)::time
    end subroutine velocity
    subroutine unioneta(ii,jj)
      use etas
      implicit none
      integer,intent(in):: ii,jj
    end subroutine unioneta
    subroutine evolveta(ii,jj)
      use etas
      implicit none
      integer,intent(in) :: ii,jj
    end subroutine evolveta
```

```
   subroutine evolverho
     use etas
     implicit none
   end subroutine evolverho
end interface


!       Initialize
call initeta

!       Perform simulation
do itime=1,6000000

   call velocity(itime)

   do i=3,NN1-3
      do j=3,NN2-3
         u1=0
         u2=0
         v1=0
         v2=0
         if (i==1) then
            u1=NN1
            u2=0
         end if
         if (i==NN1) then
            u2=-NN1
            u1=0
         end if
         if (j==1) then
            v1=NN2
            v2=0
         end if
         if(j==NN2) then
            v2=-NN2
            v1=0
         end if
         bdry=nactive(i,j)+nactive(i+1+u2,j)+nactive(i-1+u1,j)+&
         nactive(i,j+1+v2)+nactive(i,j-1+v1)
         if (bdry.eq.5) then
               call unioneta(i,j)
               call evolveta(i,j)
         else
            call unioneta(i,j)
            call evolveta(i,j)
         end if
      end do
```

```
    end do

    do i=1,NN1
      do j=1,NN2
        do s=1,nactiven(i,j)
          eta(i,j,s,1)=etanew(i,j,s,1)
          eta(i,j,s,2)=etanew(i,j,s,2)
        end do
        do s=nactiven(i,j)+1,NACT
          eta(i,j,s,1)=0.0
          eta(i,j,s,2)=0.0
        end do
        nactive(i,j)=nactiven(i,j)
      end do
    end do

    call evolverho

    if (itime.eq.2) then
      do j=1,NN2
        do i=1,NN1
          aveeta(i,j)=0.0
          do s=1,nactive(i,j)
            aveeta(i,j)=aveeta(i,j)+eta(i,j,s,2)**2
          end do
          if (nactive(i,j).eq.1) then
          endif
        end do
      end do
      do j=1,NN2
        do i=1,NN1
          temp=etanew(i,j,1,2)
          maxeta(i,j)=eta(i,j,1,1)
          do s=2,nactive(i,j)
            if (etanew(i,j,s,2).gt.temp) then
              maxeta(i,j)=eta(i,j,s,1)
              temp=eta(i,j,s,2)
            endif
          enddo
        enddo
      enddo

do j=1,NN2
    write(1,101)(aveeta(i,j),i=1,NN1)
end do
end if
```

```
if (itime.lt.7000)then
    if (mod(itime,100).eq.0) then
      do j=1,NN2
        do i=1,NN1
          aveeta(i,j)=0.0
          do s=1,nactive(i,j)
            aveeta(i,j)=aveeta(i,j)+eta(i,j,s,2)**2
          end do
          if (nactive(i,j).eq.1) then
          endif
        end do
      end do
      do j=1,NN2
        do i=1,NN1
          temp=etanew(i,j,1,2)
          maxeta(i,j)=eta(i,j,1,1)
          do s=2,nactive(i,j)
            if (etanew(i,j,s,2).gt.temp) then
              maxeta(i,j)=eta(i,j,s,1)
              temp=eta(i,j,s,2)
            endif
          enddo
        enddo
      enddo

      do j=1,NN2
        write(1+itime/10,101)(aveeta(i,j),i=1,NN1)
101       format(128(F12.8,2x))
      end do
    end if
    end if

if (itime.gt.7000)then
     if (mod(itime,10000).eq.0) then
      do j=1,NN2
        do i=1,NN1
          aveeta(i,j)=0.0
          do s=1,nactive(i,j)
            aveeta(i,j)=aveeta(i,j)+eta(i,j,s,2)**2
          end do
          if (nactive(i,j).eq.1) then
          endif
        end do
      end do
      do j=1,NN2
        do i=1,NN1
          temp=etanew(i,j,1,2)
```

```
            maxeta(i,j)=eta(i,j,1,1)
            do s=2,nactive(i,j)
              if (etanew(i,j,s,2).gt.temp) then
                maxeta(i,j)=eta(i,j,s,1)
                temp=eta(i,j,s,2)
              endif
            enddo
          enddo
        enddo

        do j=1,NN2
          write(1+itime/10,101)(aveeta(i,j),i=1,NN1)
         end do
     end if
     end if
  end do

end PROGRAM pf2d

-----------------------------------------------------------------------------------------------
subroutine initeta
  use etas
  implicit none

  !local variables
  integer :: i,j

  open(unit=25,file='orien.txt')
  open(unit=26,file='rho.txt')

  do j=1,NN2
    do i=1,NN1
      rho(i,j)=0.0
      eta(i,j,1,1)=0.0
      eta(i,j,1,2)=0.0
    enddo
  enddo

  read(25,*)((eta(i,j,1,1),j=1,NN2),i=1,NN1)
  read(26,*)((eta(i,j,1,2),j=1,NN2),i=1,NN1)

  do j=1,NN2
    do i=1,NN1
      rho(i,j)=eta(i,j,1,2)
      nactive(i,j)=1
    enddo
  enddo
```

```
  close(25)
  close(26)

end subroutine initeta

subroutine velocity(time)
  use etas
  implicit none
  integer:: i,j,m,n,s,sfound
  integer,intent(in)::time
  logical:: found

  do i=1,NUMGR
    rcx(i)=0.0
    rcy(i)=0.0
    area(i)=0.0
  enddo

  nprtcls=0
  part(1)=eta(1,1,1,1)
  do j=1,NN2
    do i=1,NN1
      do m=1,nactive(i,j)
        found=.false.
        do s=1,nprtcls
          if (eta(i,j,m,1).eq.part(s).and.(.not.found)) then
            found=.true.
            sfound=s
          endif
        enddo

        if (found) then
          area(sfound)=area(sfound)+eta(i,j,m,2)*dx**2
          rcx(sfound)=rcx(sfound)+(i-1)*dx*eta(i,j,m,2)*dx**2
          rcy(sfound)=rcy(sfound)+(j-1)*dx*eta(i,j,m,2)*dx**2
        else
          nprtcls=nprtcls+1
          part(nprtcls)=eta(i,j,m,1)
          area(nprtcls)=area(nprtcls)+eta(i,j,m,2)*dx**2
          rcx(nprtcls)=rcx(nprtcls)+(i-1)*dx*eta(i,j,m,2)*dx**2
          rcy(nprtcls)=rcy(nprtcls)+(j-1)*dx*eta(i,j,m,2)*dx**2
        endif
      enddo
    enddo
  enddo

  write(*,*) time, sum(area), nprtcls
```

```
  open(unit=20,file='check.txt')
  if (time.eq.2) then
  write(20,107) time*dt,nprtcls,sum(area)/nprtcls
  do i=1,nprtcls
     write(20,111)i,area(i)
  enddo
  endif

  if (time.eq.100) then
  write(20,107) time*dt,nprtcls,sum(area)/nprtcls
  do i=1,nprtcls
     write(20,111)i,area(i)
  enddo
  endif

  if (time.eq.1200) then
  write(20,107) time*dt,nprtcls,sum(area)/nprtcls
  do i=1,nprtcls
     write(20,111)i,area(i)
  enddo
  endif

  if (mod(time,1000).eq.0) then
  write(20,107) time*dt,nprtcls,sum(area)/nprtcls
  do i=1,nprtcls
     write(20,111)i,area(i)
  enddo
  endif

107 format (f9.1,2x,I4,2x,f15.2,2x)
111 format(36x,I3,5x, f15.2)
end subroutine velocity

subroutine unioneta(ii,jj)
  use etas
  implicit none
  integer,intent(in)::ii,jj

  !local variables
  integer:: a,m,s,tt,matched,i,j,u,v
  integer,dimension(1:4):: ai,aj

  do u=1,NACT
     do v=1,2
         etanew(ii,jj,u,v)=0.0
     end do
  end do
```

```
do i=1,NACT
  do j=1,8
    unieta(i,j)=0.0
  end do
end do

m=1
do s=1,nactive(ii,jj)
  unieta(m,1)=eta(ii,jj,s,1)
  unieta(m,2)=eta(ii,jj,s,2)
  m=m+1
end do

do a=1,4
  ai(a)=ii
  aj(a)=jj
end do
aj(1)=aj(1)+1
aj(2)=aj(2)-1
ai(3)=ai(3)+1
ai(4)=ai(4)-1
if (ii==1) ai(4)=NN1
if (ii==NN1) ai(3)=1
if (jj==1) aj(2)=NN2
if (jj==NN2) aj(1)=1
do a=1,4
  do s=1,nactive(ai(a),aj(a))
    matched=0
    tt=1
    do while (tt<=m-1)
      if (eta(ai(a),aj(a),s,1)==unieta(tt,1)) then
        unieta(tt,2+a)=eta(ai(a),aj(a),s,2)
        matched=1
        tt=10000
      end if
      tt=tt+1
    end do
    if (matched==0) then
      unieta(m,1)=eta(ai(a),aj(a),s,1)
      unieta(m,2+a)=eta(ai(a),aj(a),s,2)
      m=m+1
    end if
  end do
end do
nunieta=m-1
```

```
end subroutine unioneta

subroutine evolveta(ii,jj)
  use etas
  implicit none
  integer,intent(in) :: ii,jj

! local variables
  integer::s,m,i,j
  double precision,dimension(1:NACT)::unietan
  double precision :: B, betan,L
  double precision:: sumall,doubwel,etasq

! Theory parameters
  B=0.45
  L=10.0
  betan=1.0

  etasq=0.0
  do i=1,NACT
     unietan(i)=0.0
  end do

  do m=1,nunieta
    etasq=etasq+unieta(m,2)**2
  end do

  do m=1,nunieta
       sumall=betan*(unieta(m,3)+unieta(m,4)+unieta(m,5)&
            +unieta(m,6)-4*unieta(m,2))/dx**2
       doubwel=12*B*((1-rho(ii,jj))*unieta(m,2)-&
            (2-rho(ii,jj))*unieta(m,2)**2+unieta(m,2)*etasq)
       unietan(m)=unieta(m,2)+dt*(L*sumall-L*doubwel)
  end do

  s=0
  do m=1,nunieta
    if (abs(unietan(m))>=0.0001) then
          s=s+1
       etanew(ii,jj,s,1)=unieta(m,1)
          etanew(ii,jj,s,2)=abs(unietan(m))
          end if
  end do
  nactiven(ii,jj)=s

end subroutine evolveta
```

```
subroutine evolverho
  use etas
  implicit none
  integer::ii,jj,m,s,n
  logical::found
  double precision::A,B,etasq,etacub,biharm,divrhov,betar,sumr,phi
  double precision::Dvol,Dvap,Dsurf,Dgb,ds
  double precision,dimension(1:NN1,1:NN2)::dfdr,D,Lap,rhsx,rhsy

  ! Theory parameters
  A=18.
  B=0.45
  betar=10.
  Dvol=0.001
  Dvap=0.0001
  Dsurf=0.4
  Dgb=0.04

  do jj=1,NN2
    do ii=1,NN1
      Lap(ii,jj)=0.0
      dfdr(ii,jj)=0.0
      rhsx(ii,jj)=0.0
      rhsy(ii,jj)=0.0
    enddo
  enddo

  do jj=1,NN2
    do ii=1,NN1
      etasq=0.0
      etacub=0.0
      do m=1,nactiven(ii,jj)
        etasq=etasq+eta(ii,jj,m,2)**2
        etacub=etacub+eta(ii,jj,m,2)**3
      enddo
      dfdr(ii,jj)=(2*A*rho(ii,jj)*(1-2*rho(ii,jj))*(1-rho(ii,jj))+&
          2*B*(rho(ii,jj)-3*etasq+2*etacub))
    enddo
  enddo

  do jj=2,NN2-1
    do ii=2,NN1-1
      Lap(ii,jj)=-Betar*(rho(ii+1,jj)+rho(ii-1,jj)+rho(ii,jj+1)+rho(ii,jj-1)-
4*rho(ii,jj))/dx**2
    enddo
  enddo
```

```
do jj=1,NN2
  do ii=1,NN1
    sumr=0.0
    do m=1,nactive(ii,jj)
      do n=1,nactive(ii,jj)
        if (m.ne.n) then
          sumr=sumr+abs(eta(ii,jj,m,2)*eta(ii,jj,n,2))
        endif
      end do
    end do

    phi=0.5*(1+tanh(8*(rho(ii,jj)-.5)))
    if (rho(ii,jj)*(1-rho(ii,jj)).ge.0) then
      ds=Dsurf*rho(ii,jj)*(1-rho(ii,jj))
    else
      ds=0
    endif
    D(ii,jj)=Dvol*phi+Dvap*(1-phi)+ds+Dgb*sumr
  end do
end do

do jj=3,NN2-2
  do ii=3,NN1-2
    rhsx(ii,jj)=D(ii,jj)*((Lap(ii+1,jj)-Lap(ii-1,jj))+&
        (dfdr(ii+1,jj)-dfdr(ii-1,jj)))/(2*dx)
    rhsy(ii,jj)=D(ii,jj)*((Lap(ii,jj+1)-Lap(ii,jj-1))+&
        (dfdr(ii,jj+1)-dfdr(ii,jj-1)))/(2*dx)
  enddo
enddo
do jj=4,NN2-3
  do ii=4,NN1-3
    rhon(ii,jj)=rho(ii,jj)+dt*(((rhsx(ii+1,jj)-rhsx(ii-1,jj))/(2*dx)+&
        (rhsy(ii,jj+1)-rhsy(ii,jj-1))/(2*dx)))
    if (rhon(ii,jj).gt.1.5) then
      write(*,*)D(ii,jj),Lap(ii,jj),dfdr(ii,jj)
    endif
  enddo
enddo

do ii=1,NN1
  do jj=1,3
    rhon(jj,ii)=0.0
    rhon(NN1+1-jj,ii)=0.0
    rhon(ii,jj)=0.0
    rhon(ii,NN1+1-jj)=0.0
  enddo
enddo
```

```
  do jj=1,NN2
    do ii=1,NN1
      rho(ii,jj)=rhon(ii,jj)
    enddo
  enddo

end subroutine evolverho
```

A2 Random number generator

```
C=============================================================
      SUBROUTINE RAND(SEEDIN,SEEDOUT,RAN)
C=============================================================
      IMPLICIT DOUBLE PRECISION (A-H,O-Z)
      XM=65539.0
      DIV=2.0**31
      X=SEEDIN*XM/DIV
1     CONTINUE
      DO 2 J=14,0,-1
      IF(X.GT.10.0**J) GO TO 3
2     CONTINUE
      GO TO 4
3     X=X-10.0**J
4     IF(X.LE.1.0E0) GO TO 5
      GO TO 1
5     RAN=X
      SEEDOUT=RAN*DIV
      ran=2.0*x-1.0
      seedout=abs(seedout)
      RETURN
      END
```

A3 Quantitative analysis for grain coalescence

```
      implicit double precision (a-h,o-z)
      parameter (n=10000, m=500)
       dimension x(n),y(n),z(n),theta(n),phi(n),eta(n),numA(n),numB(n),
     * icon(n,m),ifar(n,m),xdiff(n,m),xdiff2(n,m),xdiff3(n,m),
     * xdiff4(n,m),xdiff5(n,m),xdiff6(n,m),icluster(n,m),igroup(n),
     * isinter(n,m), igroup2(n)
C=============================================================
      logical sinter=.true.
      logical sinter2=.true.
      logical sinter3=.true.
      logical size=.true.
      logical size2=.true.
      logical size3=.true.
      logical size4=.true.

      R=0.65d0
      npoin=997
      ztouch=15.0d0
      zclose=15.0d0

      SEEDIN=853492
      pi=dacos(-1.0d0)

      do i=1,n
      do j=1,m
            icon(i,j)=0
      end do
      end do

      do i=1,10000
            x(i)=0.0d0; y(i)=0.0d0; z(i)=0.0d0;
      end do

            open(unit=10,file='997 3D R0.7.txt')
      do ipoin=1,npoin
            read(10,*) x(ipoin),y(ipoin), z(ipoin)
      end do
      close(unit=10)

C     To indentify contacting neighbors and close neighbors

      open(unit=15,file='output.txt')
      do ipoin=1,npoin
```

```
        call RAND(SEEDIN,SEEDOUT,RAN)
                SEEDIN=SEEDOUT
        theta(ipoin)=dabs(RAN*pi/4.0d0)*360.0d0/(2.0d0*pi)

                call RAND(SEEDIN,SEEDOUT,RAN)
                SEEDIN=SEEDOUT
            phi(ipoin)=dabs(RAN*pi/2.0d0)*360.0d0/(2.0d0*pi)

                call RAND(SEEDIN,SEEDOUT,RAN)
                SEEDIN=SEEDOUT
            eta(ipoin)=dabs(RAN*pi/2.0d0)*360.0d0/(2.0d0*pi)

          numA=0; numB=0
          do jpoin=1,npoin
                if (ipoin.ne.jpoin) then
dist=dsqrt((x(ipoin)-x(jpoin))**2 + (y(ipoin)-y(jpoin))**2+(z(ipoin)-z(jpoin))**2)
              if (dist.le.2.0d0*R) then
                              numA=numA+1
                                    icon(ipoin,numA)=jpoin
              end if
              if (dist.gt.2.0d0*R.and.dist.le.3.0d0*R) then
                 numB=numB+1
                                    ifar(ipoin,numB)=jpoin
                           end if
                 end if
          end do

          write(15,1001) ipoin, x(ipoin),y(ipoin),z(ipoin),theta(ipoin),
     *    phi(ipoin),eta(ipoin),numA(ipoin),numB(ipoin)
          end do

          close (unit=15)
1001    format(I5, 6(g15.5,1x),2(I5,1x))

          open (unit=50, file='conn.txt')
                write (50,5001) ((icon(i,j), j=1,12), i=1,npoin)
          close (unit=50)
5001    format (12(I5,1x))

          open (unit=60, file='far.txt')
                write (60,6001) ((ifar(i,j), j=1,24), i=1,npoin)
          close (unit=60)
6001    format (24(I5,1x))

C       To calculate misorientation angle and neighbors within the range

          open (unit=15, file='output.txt')
```

```
        do ipoin=1,npoin
                read (15, 1501) theta(n), phi(n),eta(n)
        end do
1501    format (53x, 3(g16.5,1x))

        open (unit=70, file='group.txt')
        open (unit=91, file='cluster.txt')
        open (unit=60, file='far.txt')
        open (unit=50, file='conn.txt')

        do ipoin=1,npoin
                igroup=1; xdiff=0.0d0; xdiff2=0.0d0
                read (50,5001) ((icon(i,j), j=1,6), i=ipoin,ipoin)
                read (60,6001) ((ifar(i,j), j=1,12), i=ipoin,ipoin)

                do j=1,6; i=ipoin
                jpoin=icon(i,j)
                  if (jpoin.eq.0) then
                  end if
                  if (jpoin.ne.0) then
            xdiff= dabs(theta(ipoin)-theta(jpoin))
            xdiff2= dabs(phi(ipoin)-phi(jpoin))
            xdiff3= dabs(eta(ipoin)-eta(jpoin))
                        if (xdiff(i,j).gt.0.0d0.and.xdiff2(i,j).gt.0.0d0.and.
    *                   xdiff3(i,j).gt.0.and.xdiff(i,j).lt.ztouch.and.
    *               xdiff2(i,j).lt.ztouch.and.xdiff3(i,j).lt.ztouch) then
                        igroup=igroup+1
                        icluster(ipoin,igroup)=jpoin
                        end if
                        if (xdiff(i,j).gt.ztouch.and.xdiff2(i,j).gt.ztouch.and.
    *               xdiff3(i,j).gt.ztouch)then
                        end if
                  end if
        end do

C       For non contact neighbors

        do j=1,12; i=ipoin
                jpoin=ifar(i,j)
                  if (jpoin.eq.0) then
                  end if
                  if (jpoin.ne.0) then
                        xdiff4= dabs(theta(ipoin)-theta(jpoin))
              xdiff5= dabs(phi(ipoin)-phi(jpoin))
              xdiff6= dabs(eta(ipoin)-eta(jpoin))

                        if (xdiff4(i,j).gt.0.0d0.and.xdiff5(i,j).gt.0.0d0.and.
```

```
*               xdiff6(i,j).gt.0.0d0.and.xdiff4(i,j).lt.zclose.and.
*               xdiff5(i,j).lt.zclose.and.xdiff6(i,j).lt.zclose)then
                        igroup=igroup+1
                        icluster(ipoin,igroup)=jpoin
                        end if
                        if (xdiff3(i,j).gt.zclose.and.xdiff4(i,j).gt.zclose.and.
*       xdiff6(i,j).gt.zclose)then
                        end if
                 end if
                end do
                write (70, 7011) igroup(n)
        end do
        write(91,1550) (i,(icluster(i,j),j=2,12),i=1,npoin)

        close (unit=15)
        close (unit=20)
        close (unit=70)
        close (unit=91)
        close (unit=60)
        close (unit=25)
        close (unit=50)

1550  format(12(I3,1x))
7001  format (I5)
3001  format (12(g10.5, 1x))
7011  format(I5)
3011  format(24(g10.5, 1x))
2011  format(24(I5,1x))
9001  format(38(I3,1x)/)
1850  format(200(I3,1x))


C       To reduce grain quantity with increasing size

        open (unit=92, file='group2.txt')
        open (unit=99, file='sinter.txt')
        open (unit=91, file='cluster.txt')
        read (91,1550) ((icluster(i,j), j=1,12), i=1,npoin)
        close (unit=91)
        open (unit=70, file='group.txt')
        do i=1,npoin
                read (70,7001) igroup(i)
        end do

        numC=0
        do i=1,npoin
          do j=1,npoin
```

```
            do k=1,igroup(j)

          sinter=any (icluster(i,1:igroup(i)).eq.icluster(j,k))
          size= all(icluster(i,1:igroup(i)).gt.0)
          size2= all(icluster(j,1:igroup(j)).gt.0)
 if((sinter==.true.).and.(size==.true.).and.(size2==.true.).and.(i.ne.j)) then
          write (99,1850) icluster(j,1:igroup(j)),icluster(i,1:igroup(i))
          igroup2=igroup(j)+igroup(i)
          numC=numC+1
          icluster(i,1)=0
          icluster(j,1)=0
          write (92,7001) igroup2(j)
          end if
                  end do
           end do

          if((size==.true.).and.(igroup(i).ge.1)) then
          write (99,1850) icluster(i,1:igroup(i))
          igroup2=igroup(i)
          numC=numC+1
          icluster(i,1)=0
          write (92,7001) igroup2(i)
          end if
          end do

          close (unit=92)
          close (unit=70)
          close (unit=99)

C         2nd reduction

          open (unit=91, file='cluster.txt')
          open (unit=70, file='group.txt')
          open (unit=99, file='sinter.txt')
          open (unit=92, file='group2.txt')
          do i=1,numC
                  read (92,7001) igroup2(i)
          end do

          do i=1,numC
                  read (99,1850) (isinter(i,j),j=1,igroup2(i))
          end do
          close (unit=99)

          numD=0
          do i=1,numC
           do j=1,numC
```

```
            do k=1,igroup2(j)

          sinter3=any (isinter(i,1:igroup2(i)).eq.isinter(j,k))
          size3= all(isinter(i,1:igroup2(i)).gt.0)
          size4= all(isinter(j,1:igroup2(j)).gt.0)

if((sinter3==.true.).and.(size3==.true.).and.(size4==.true.).and.(i.ne.j)) then
          write (91,1850) isinter(j,1:igroup2(j)),isinter(i,1:igroup2(i))
          igroup=igroup2(j)+igroup2(i)
          numD=numD+1
          isinter(i,1)=0
          isinter(j,1)=0
          write (70,7001) igroup(j)
          end if
                    end do
           end do

          if((size3==.true.).and.(igroup2(i).ge.1))then
          write (91,1850) isinter(i,1:igroup2(i))
          igroup=igroup2(i)
          numD=numD+1
          isinter(i,1)=0
          write (70,7001) igroup(i)
          end if
          end do

          close (unit=91)
          close (unit=92)
          close (unit=70)

C         Repeat reduction

999       open (unit=92, file='group2.txt')
          open (unit=99, file='sinter.txt')
          open (unit=70, file='group.txt')
          do i=1,numD
                    read (70,7001) igroup(i)
          end do

          open (unit=91, file='cluster.txt')
          do i=1,numD
                     read (91,1850) (icluster(i,j), j=1,igroup(i))
          end do
          close (unit=91)


          numC=0
```

```
          do i=1,numD
            do j=1,numD
              do k=1,igroup(j)

sinter=any (icluster(i,1:igroup(i)).eq.icluster(j,k).and.icluster(j,k).ne.0)
          size= all(icluster(i,1:igroup(i)).gt.0)
          size2= all(icluster(j,1:igroup(j)).gt.0)

if((sinter==.true.).and.(size==.true.).and.(size2==.true.).and.(i.ne.j)) then
          write (99,1850) icluster(j,1:igroup(j)),icluster(i,1:igroup(i))
          igroup2=igroup(j)+igroup(i)
          numC=numC+1
          icluster(i,1)=0
          icluster(j,1)=0
          write (92,7001) igroup2(j)
          end if
                    end do
            end do

          if((size==.true.).and.(igroup(i).ge.1)) then
          write (99,1850) icluster(i,1:igroup(i))
          igroup2=igroup(i)
          numC=numC+1
          icluster(i,1)=0
          write (92,7001) igroup2(i)
          end if
          end do

          close (unit=92)
          close (unit=70)
          close (unit=99)

          open (unit=91, file='cluster.txt')
          open (unit=70, file='group.txt')
          open (unit=99, file='sinter.txt')
          open (unit=92, file='group2.txt')
          do i=1,numC
                    read (92,7001) igroup2(i)
          end do

          do i=1,numC
                    read (99,1850) (isinter(i,j),j=1,igroup2(i))
          end do
          close (unit=99)

          numD=0
          do i=1,numC
```

```
            do j=1,numC
              do k=1,igroup2(j)

           sinter3=any (isinter(i,1:igroup2(i)).eq.isinter(j,k))
           size3= all(isinter(i,1:igroup2(i)).gt.0)
           size4= all(isinter(j,1:igroup2(j)).gt.0)
 if((sinter3==.true.).and.(size3==.true.).and.(size4==.true.).and.(i.ne.j)) then
           write (91,1850) isinter(j,1:igroup2(j)),isinter(i,1:igroup2(i))
           igroup=igroup2(j)+igroup2(i)
           numD=numD+1
           isinter(i,1)=0
           isinter(j,1)=0
           write (70,7001) igroup(j)
           end if
                    end do
            end do

           if((size3==.true.).and.(igroup2(i).ge.1))then
           write (91,1850) isinter(i,1:igroup2(i))
           igroup=igroup2(i)
           numD=numD+1
           isinter(i,1)=0
           write (70,7001) igroup(i)
           end if
           end do

           close (unit=91)
           close (unit=92)
           close (unit=70)

C          remove duplicate number

           open (unit=99, file='sinter.txt')
           open (unit=92, file='group2.txt')
           open (unit=70, file='group.txt')
           do i=1,numD
                    read (70,7001) igroup(i)
                    write (92,7001) igroup(i)
           end do

           open (unit=91, file='cluster.txt')
           do i=1,numD
                    read (91,1850) (icluster(i,j),j=1,igroup(i))
           end do
           close (unit=91)
           close (unit=70)
```

```
      do i=1,numD
            do j=1,igroup(i)
                  do k=1,igroup(i)
 if (icluster(i,j).eq.icluster(i,k).and.(j.ne.k).and.(icluster(i,j).gt.0)) then
      icluster(i,k)=0
      end if
                  end do
            end do
      write (99, 1850) (icluster(i,j),j=1,igroup(i))
      end do

      close (unit=99)
      close (unit=92)

C     remove ZERO

      open (unit=91, file='cluster.txt')
      open (unit=92, file='group2.txt')
      do i=1,numD
      read (92,7001) igroup2(i)
      end do

      open (unit=99, file='sinter.txt')
      do i=1,numD
            read (99,1850) (isinter(i,j),j=1,igroup2(i))
      end do
      close (unit=99)
      close (unit=92)

      open (unit=70, file='group.txt')

      icheck=0
      igroup=0
      do i=1,numD
            do j=1,igroup2(i)
      if (isinter(i,j).ne.0) then
      igroup(i)=igroup(i)+1
      icluster(i,igroup(i))=isinter(i,j)
      end if
            end do

      write(91,1850) (icluster(i,j),j=1,igroup(i))
      write(70,7001) igroup(i)
      icheck=icheck+igroup(i)
      end do

      close (unit=91)
```

```
      close (unit=92)
      close (unit=70)

C     Check if reduction completed

      if (icheck.ne.npoin) then
      go to 999
      else if (icheck.eq.npoin) then
      Write(*,*) "completed! Yeah!"
      end if

C=============================================================
C     merge cluster with average orientation (generate input data for chapter 7)

      open (unit=170, file='coal output.txt')

      open(unit=15,file='output.txt')
      do ipoin=1,npoin
      read (15, 1101) phi(ipoin)
      end do
1101  format (69x, 1g15.5)
2101  format (I5, g15.5)
      open (unit=70, file='group.txt')
      do i=1, numD
      read (70, 7001) igroup(i)
      end do

      open (unit=91, file='cluster.txt')


      do i=1, numD
      sum=0.0
        read (91,1850) (icluster(i,j), j=1, igroup(i))
            do j= 1, igroup(i)
            sum= sum+phi(icluster(i,j))
        end do
        phi(i)= sum/igroup(i)

      end do


            do i=1, numD
                  do j=1, igroup(i)
                        if ipoin=icluster(i,j)
                        phi(ipoin)=phi(i)
                        write (170, 2101) icluster(i,j), phi(i)
                  end do
```

```
                end do

        close (unit=170)

        open (unit=151, file='output2.txt')
        open (unit=170, file='coal output.txt')
        do ipoin=1,npoin
        read (170, 2101) i, phi(i)
        end do

        do ipoin=1,npoin
                        if ipoin=i
                        theta(ipoin)=theta(i)
          write(151,1001) ipoin, x(ipoin),y(ipoin),z(ipoin),theta(ipoin),
*       phi(ipoin),numA(ipoin),numB(ipoin)
        end do
        close (unit=170)

        end
```

A4 Program to convert center points and random orientations into pixel matrix for phase field simulation

```
C============================================================
      implicit double precision (a-h,o-z)
     parameter (n=1100, m=1100, N1=256, N2=256, Nact=2)
      dimension x(n),y(n),z(n),theta(n),phi(n),s(n), pixel(n,m)
      double precision, dimension (1:N1,1:N2,1:Nact,1:2)::eta,orien
C============================================================
      SN1=9.5
      NN2=256
      npoin=997
      R=1.68

C     To convert into pixel matrix

      do i=1,NN2
      do j=1,NN2
            pixel(i,j)=0
            orien(i,j,1,1)=0
            eta(i,j,1,2)=0
      end do
      end do

     do i=1,1000
            x(i)=0.0d0; y(i)=0.0d0; z(i)=0.0d0;
      end do

      open (unit=10, file='output 14deg.txt')
       do ipoin=1,npoin
            read (10,1001) x(ipoin),y(ipoin), theta(ipoin)
       end do
      close (unit=10)
1001  format (5x,2(g15.5,1x), 32x, g15.5)

      do i=1,NN2
      do j=1,NN2
            do ipoin=1,npoin

     Radius=dsqrt((i-(x(ipoin)+5)*SN1)**2+(j-(y(ipoin)+5)*SN1)**2)
          if (Radius.lt.R*SN1) then
                        pixel(i,j)=theta(ipoin)
                        orien(i,j,1,1)=theta(ipoin)
                        eta(i,j,1,2)=1
                        end if
            end do
```

```
          end do
          end do

          open (unit=31, file='orien.txt')
          write (31, 2001) ((orien(i,j,1,1), j=1,NN2), i=1,NN2)
          close (unit=31)

          open (unit=32, file='rho.txt')
          write (32, 2001) ((eta(i,j,1,2), j=1,NN2), i=1,NN2)
          close (unit=32)
2001    format (256F10.4)

          end
```